Dissertations   Theses and Dissertations

Fall 2000

Nonlinear optical properties of nano structures

Mahesh U. Ajgaonkar
New Jersey Institute of Technology

Recommended Citation

ABSTRACT

NONLINEAR OPTICAL PROPERTIES OF NANOSTRUCTURES

Nonlinear optical properties of nanoscale semiconductors had been a topic of intense research in recent years in attempts to realize all-optical communication systems. These semiconductor nanoclusters, in the range of 1-100nm are hosted in a dielectric material and are considered as a particular example of Conditional Artificial Dielectric (CAD). It has been reported that the dielectric properties of such materials will be greatly changed by light intensity.

Two main paths to realize nano semiconductor clusters are reported in this dissertation. The Pulsed Laser Deposition (PLD) technique is first described. Here we were investigating the effect of surface modification of nano silicon clusters by incorporating various gases (H_2, Ar, He) during the deposition process. Linear and nonlinear optical properties of these passivated Si nanoclusters were obtained.

Ion Implantation is another successful method to obtain nano semiconductor clusters. In order to further enhance the nonlinear optical properties of these clusters, we incorporated them in optically confining structures, such as three-dimensional photonic crystals. The latter part of the dissertation is devoted to three-dimensional periodic structures made of silica spheres (opal) which were implanted with Si, Ge and Er. Linear and nonlinear optical properties of these novel materials have been measured and assessed.

NONLINEAR OPTICAL PROPERTIES OF NANOSTRUCTURES

by
Mahesh U. Ajgaonkar

A Dissertation
Submitted to the Faculty of
New Jersey Institute of Technology
in Partial Fulfillment of the Requirements for the Degree of
Doctor of Philosophy in Electrical Engineering

Department of Electrical and Computer Engineering

January 2001

APPROVAL PAGE

NONLINEAR OPTICAL PROPERTIES OF NANOSTRUCTURES

Mahesh U. Ajgaonkar

Dr. Haim Grebel, Dissertation Advisor   Date
Professor of Electrical and Computer Engineering, NJIT

Dr. Gerald Whitman, Committee Member   Date
Professor of Electrical and Computer Engineering, NJIT

Dr. Marek Sosnowski, Committee Member   Date
Associate Professor of Electrical and Computer Engineering, NJIT

Dr. John Federici, Committee Member   Date
Associate Professor of Physics Department, NJIT

Dr. Zafar Iqbal, Committee Member   Date
Senior Principal Scientist, Honeywell International, Morristown, NJ

BIOGRAPHICAL SKETCH

Author: Mahesh U. Ajgaonkar

Degree: Doctor of Philosophy

Date: January 2001

Undergraduate and Graduate Education:

- Doctor of Philosophy in Electrical Engineering,
  New Jersey Institute of Technology, Newark, NJ, 2000

- Master of Science in Electrical Engineering,
  Indian Institute of Technology, Madras, India, 1997

- Bachelor of Engineering in Electronics Engineering,
  Bombay University, Mumbai, India, 1994

Major: Electrical Engineering

Publications:

M. Ajgaonkar, Y. Zhang, H. Grebel, C.W. White,
"Nonlinear optical properties of a submicron SiO_2 spheres (opal) embedded with Si nanoparticles", Applied Physics Letters, **75**(11), pp 1532-1534, 1999.

M. Ajgaonkar, Y. Zhang, H. Grebel, M. Sosnowski, D.C. Jacobson,
"Linear and nonlinear optical properties of erbium-implanted coherent array of submicron silica spheres", Applied Physics Letters, **76**(26), pp 3876-3878, 2000.

M. Ajgaonkar, S.Vijayalakshmi, Y.Zhang, H.Grebel, C.W. White,
"Nonlinear Optical properties of Ion Implanted Si Nanoclusters in Silica Substrates (short note in " Physics, Chemistry and Application of Nanostructures Reviews and Short Notes to Nanomeeting'99, World Scientific, edited by V.E. Borisenko et al).

Dedicated to Bai Aaji and my parents

ACKNOWLEDGEMENT

TABLE OF CONTENTS

TABLE OF CONTENTS
(Continued)

TABLE OF CONTENTS
(Continued)

LIST OF FIGURES

CHAPTER 1

INTRODUCTION

1.1 Background

In the last three decades the telecommunications industry has been revolutionized by the advent and deployment of long haul terrestrial and undersea fiber optic communication links. In the last five years or so, the telecommunication industry has witnessed an explosive growth of data and internet traffic which is doubling every three months. It is expected to have 4.5 billion Internet accounts by the year-end of 2003. The major telecommunication technology able to support this demand appears to be optical communication [1], [2] which is based on low loss and low dispersion fiber media coupled with novel devices.

To support this growth in the optical communication field, the semiconductor world also has been driven towards the quantum limit of operating devices. To elaborate in brief, the semiconductor lasers which started with a threshold current density of few 1000's of A/cm^2 [3] in 1970's are now achieving a value of few μA/cm^2 in VCSEL (Vertical Cavity Surface Emitting Lasers) [4]. Correspondingly, the size of the semiconducting devices is halving every 2 years [5] eventually reaching the nano limit.

With these ever-increasing applications of the optical devices, the need for the novel optically functional and transparent materials increases. At the same time, the new optical materials should be adaptable enough to be utilized with prevailing IC manufacturing technology. It is the aim of this thesis to investigate novel optical materials which will enable all-optical communication systems.

So far direct bandgap semiconductors have been used in optoelectronics or all-optical systems. The involvement of phonons in the indirect transitions make their corresponding optical elements slow and inefficient for the GB/s system applications. Recent studies, though, show that indirect bandgap materials could be used in high speed applications [6], [7], [8]. These applications mainly utilize relatively slow devices in switching. One of our aims in this thesis is to explore the use of indirect bandgap materials in applications that require much higher speeds.

It is well known that the nonlinear optical properties of a given semiconductor material are amplified when dimensions are reduced to nanometer scale size. This is due to effects of quantum confinement in direct bandgap materials and the increased overlap integral between photon and electron in indirect bandgap materials. For example, the nonlinear time constant in bulk silicon is on the order of microseconds whereas it is on the order of sub-nanosecond in nano size silicon clusters [9]. Our goal in this dissertation is therefore to explore the nonlinear optical properties of nanoclusters.

Our example materials were Si, Ge and Er, which cover a broad applications potential for the optical communications. Silicon and germanium are most widely used semiconductors in electronic circuits but rarely in optoelectronic circuits. We wish to pursue if their nonlinear properties could make them good candidates for optoelectronic integration of nonlinear functional elements such as, all optical switching and limiters, wavelength manipulators etc. The use of erbium doped fiber amplifier in optical communication systems has revolutionized optical communication systems in the last decade. With this in mind we also investigated erbium implanted photonic crystals.

In the following section, we give a semi classical [10] treatment of the nonlinear optics. In the subsequent section we complete the picture by considering basic electromagnetic theory [11] of nonlinear optics [12]. At the end of the current chapter, an outline of the thesis is included.

1.2   Theoretical Background

The classical picture begins with consideration of an electron attached to an infinitely massive positive charge (i.e. a nucleus) under the influence of a sinusoidally varying electric field $\vec{E}$ as shown in Fig 1.1.

E(t)

$k = m\omega_0^2$

Electron   Nucleus

$E_{dipole} \approx \eta$
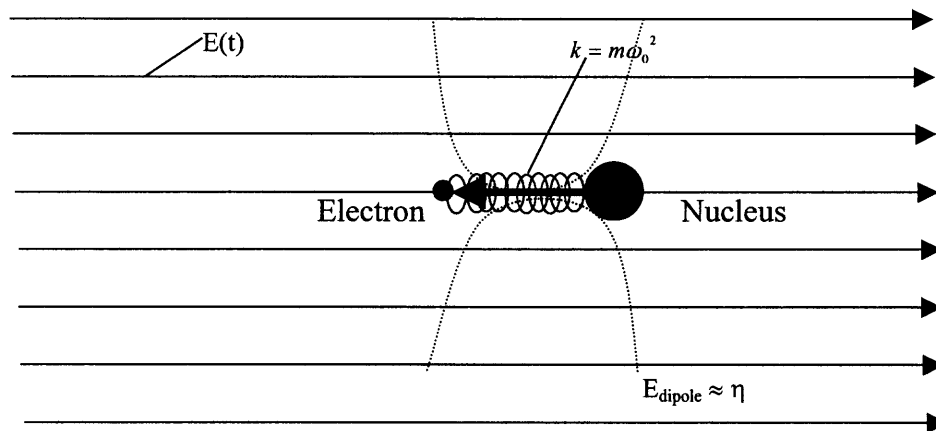
Figure 1.1   Electron attached to nucleus

In above Fig. 1.1, an electron (i.e. negative charge) of mass m is bound to the positive charge of infinite mass through internal field E_{int}. For linear field, this internal field is represented by a spring with spring constant $k = m\omega_o^2$. The displacement of the

electron from equilibrium is given by $x(t)$. The damping η is represented as a reradiated dipole field shown by the dotted lines as E_{dipole}. Considering only one dimension, Newton's equation of motion for the system in Figure 1.1 is

$$m\frac{d^2x}{dt^2} + \eta\frac{dx}{dt} + m\omega_0^2 x = -eE(t)$$
(1.2.1)

where x is the distance the electron has moved from its equilibrium position, m is the mass of the electron, η is a damping term, and, ω_0 is the resonant frequency of the electron. The oscillating macroscopic polarizability is given by the solution $x(t)$ of Eq. (1.2.1) above as

$$P(t) = Nd(t) = -Nex(t)$$
(1.2.2)

where N is the number of oscillators per unit volume and d is the dipole moment. For $E = 0.5E_0(e^{j\omega t} + e^{-j\omega t}) = E_0\cos(\omega t)$ where ω is the optical frequency, the solution to the x in the linear Eq. (1.2.2) can be found by substituting $x = 0.5x_0(e^{j\omega t} + e^{-j\omega t})$ $= x_0\cos(\omega t)$ in Eq. (1.2.1) to get

$$x_0 = -e\frac{E_o}{m}(\omega_0^2 - \omega^2 + i\Gamma\omega)^{-1}$$
(1.2.3)

where $\Gamma = \eta/m$ gives rise to complex polarizability of

$$P(t) = -\frac{Ne^2E(t)}{m}(\omega_0^2 - \omega^2 + i\Gamma\omega)^{-1}$$
(1.2.4)

The index of refraction and absorption coefficient can be approximated from the above Eq.(1.2.4) if it is assumed that only one resonance is near the optical frequency and that the local field that the electron sees is close to the incident field. The polarizability is

linear in the electric field and can be written as $P = \chi E$ where χ is the complex linear susceptibility tensor. The linear relationship between P and E results in an index of refraction and absorption coefficient that is independent of the electric field. That is, for weak absorption, small local field correction, and only one dominant nearby resonance ω_0, the index of refraction and the absorption coefficient are independent of optical electric field as observed at low optical intensities, and given by

$$n^2 \approx 1 + \frac{\text{Re}(\chi)}{\varepsilon_0} \qquad (1.2.5)$$

$$\alpha \approx \frac{\omega \, \text{Im}(\chi)}{nc\varepsilon_0} \qquad (1.2.6)$$

This simple oscillating spring model seems to predict field-independent indices and absorption coefficients, but it is note very clear as to why it should be so successful. To probe further we look at the simple spring model in detail.

The spring model uses a linear (Hooke's Law) restoring force $F = kx$, where k is the spring constant or $k = m\omega_0^{\,2}$. In general, the charges responding to the oscillating electric field have been moved from equilibrium point and return to that point when the field is removed. This is called the stable equilibrium and can be thought of a potential well that has a minimum point. The potential V can be expanded about the minimum point located at $x = 0$

$$V(x) = V\Big|_{x=0} + \frac{dV}{dx}\Big|_{x=0} x + \frac{d^2V}{dx^2}\Big|_{x=0} \frac{x^2}{2} + \ldots \ldots \qquad (1.2.7)$$

The first two terms of the above equation are zero at $x = 0$ and , the potential becomes

$$V(x) = \frac{d^2V}{dx^2}\bigg|_{x=0}\frac{x^2}{2} + \frac{d^3V}{dx^3}\bigg|_{x=0}\frac{x^3}{3!} + \ldots \ldots \quad (1.2.8)$$

which results in a force of $dV = F \bullet dx$, or

$$F = \frac{d^2V}{dx^2}\bigg|_{x=0} x + \frac{d^3V}{dx^3}\bigg|_{x=0}\frac{x^2}{2} + \ldots \ldots \quad (1.2.9)$$

The first term in the Eq.(1.2.9) is the linear term of Hooke's law and is the dominant term for small deviation of the electron from it's equilibrium position. With larger perturbations, usually associated with large optical fields, the restoring force must include higher-order terms and would result in more complicated nonlinear behavior.

For a general restoring force derived from a non-parabolic stable equilibrium potential well, the force equation about minimum potential is

$$m\frac{d^2x}{dt^2} + \eta\frac{dx}{dt} + m\omega_0^2 x + \sum_{i=1}^{N} D_i x^{i+1} = -eE(t) \quad (1.2.10)$$

where D_i are the coefficients characterizing the nonlinearity of the response. The solution for small anharmonic contributions is of the form

$$x(t) = \sum_{j=1}^{N} \frac{x_j \exp(ij\omega t) + c.c.}{2} \quad (1.2.11)$$

where c.c. mean the complex conjugate. By equating the coefficients of $e^{i\omega t}$, the second-order term x_2 can be found and so on for other higher order terms.

The anharmonic terms result in a nonlinear polarizability which, in general, for three dimensions is

$$P_i(x_p) = \chi_{ij}^{(1)}E_j + \chi_{ijk}^{(2)}E_jE_k + \chi_{ijkl}^{(3)}E_jE_kE_l + \ldots \ldots \quad (1.2.12)$$

where E is the total electric field present. The equation above clearly shows the nonlinear relation between the polarization developed in a material due to the applied electric field. The first term is the result of a linear restoring force and describes the linear, low intensity, optical interactions with the material. The second term includes the second order susceptibility $\chi_{ijk}{}^{(2)}$ and two electric fields E_j and E_k. This term results from anharmonic potential well and is only found in crystals without inversion symmetry. In fact, all the even numbered, higher order susceptibilities are eliminated in materials that have center of inversion. On the other hand, the third order term, and all higher order odd terms, are found in all materials assuming that the materials will not suffer a laser induced damage.

1.3   Electromagnetic Theory Behind Optical Nonlinearity

In this section, we review a few of the concepts of the electromagnetic wave propagation which lead us to the development of optical nonlinearity [12]. Let us start with the wave equation for the propagation of light (i.e. electromagnetic field) through a nonlinear optical medium. We begin with the Maxwell's equations in Gaussian units in the following form:

$$\vec{\nabla} \bullet \vec{D} = 4\pi\vec{\rho} \tag{1.3.1}$$

$$\vec{\nabla} \bullet \vec{B} = 0 \tag{1.3.2}$$

$$\vec{\nabla} \times \vec{E} = -\frac{1}{c}\frac{\partial \vec{B}}{\partial t} \tag{1.3.3}$$

$$\vec{\nabla} \times \vec{H} = \frac{1}{c} \frac{\partial \vec{D}}{\partial t} + \frac{4\pi}{c} \vec{J} \qquad (1.3.4)$$

where,

$\vec{E}$ is the electric field vector, $\vec{D}$ is the electric displacement vector, $\vec{B}$ is the magnetic flux density, and $\vec{H}$ is the magnetic field, and $\vec{J}$ is the current density, and all the field quantities are time dependent. For a nonmagnetic, nonlinear medium, $\vec{B} = \vec{H}$ i.e. $\mu_0 = 1$, and

$$\vec{D} = \vec{E} + 4\pi \vec{P} \qquad (1.3.5)$$

where $\vec{P}$ is the polarization vector and depends nonlinearly on the local field strength $\vec{E}$. We now proceed to derive the optical wave equation using standard techniques namely, by taking the curl of Eq. (1.3.3) and using vector identities. The curl of Eq.(1.3.3) with substitution for $\vec{\nabla} \times \vec{H}$ from Eq. (1.3.4), and assuming source free conditions we get

$$\vec{\nabla} \times \vec{\nabla} \times \vec{E} + \frac{1}{c^2} \frac{\partial^2 \vec{D}}{\partial t^2} \qquad (1.3.6)$$

Substitution of Eq. (1.3.5) leads to

$$\vec{\nabla} \times \vec{\nabla} \times \vec{E} + \frac{1}{c^2} \frac{\partial^2 \vec{E}}{\partial t^2} = \frac{-4\pi}{c^2} \frac{\partial^2 \vec{P}}{\partial t^2} \qquad (1.3.7)$$

This is the general form of the wave equation for the electric field in source free medium. To separate the linear and nonlinear parts of the above equation, one can write the displacement vector as follows:

$$\vec{D} = \vec{D}^{(L)} + \vec{D}^{(NL)} \qquad (1.3.8)$$

where

$$\vec{D}^{(L)} = \vec{E} + 4\pi \vec{P}^{(L)} \qquad (1.3.9)$$

and

$$\vec{D}^{(\mathrm{NL})} = 4\pi\vec{P}^{(\mathrm{NL})}$$ (1.3.10)

using these equations, the wave Eq. (1.3.7) becomes

$$\vec{\nabla}\times\vec{\nabla}\times\vec{E} + \frac{1}{c^2}\frac{\partial^2\vec{D}^{(L)}}{\partial t^2} = -\frac{4\pi}{c^2}\frac{\partial^2\vec{P}^{(NL)}}{\partial t^2}$$ (1.3.11)

If each field component can be written as Fourier series i.e.

$$\vec{E}(\vec{r},t) = \sum_{\mathrm{n}}\vec{E}_{\mathrm{n}}(\vec{r},t) = \sum_{\mathrm{n}}\left[\vec{E}_n(\vec{r})e^{-i\omega_n t} + \vec{E}^*{}_n(\vec{r})e^{i\omega_n t}\right] = \sum_n E_{cn}(\vec{r},t) + E^*{}_{cn}(\vec{r},t)$$ (1.3.12)

with similar expressions for $\vec{D}$ and $\vec{P}$ and substituting these expressions from Eq.(1.3.12) in Eq. (1.3.11) gives:

$$\vec{\nabla}\times\vec{\nabla}\times\vec{E}_{cn} + \frac{\varepsilon^{(1)}(\omega_n)}{c^2}\bullet\frac{\partial^2\vec{E}_{cn}}{\partial t^2} = -\frac{4\pi}{c^2}\frac{\partial^2\vec{P}_{cn}^{(NL)}}{\partial t^2}$$ (1.3.13)

For the general case of non dissipative dispersive medium, the relationship between $\vec{E}$ and $\vec{D}$ can be written as follows in terms of a real frequency dependent dielectric tensor:

$$\vec{D}_{cn}^{(L)}(\vec{r},t) = \varepsilon^{(1)}(\omega_n)\bullet\vec{E}_{cn}(\vec{r},t)$$ (1.3.14)

where the subscript n denotes the frequency component under consideration. Substituting these expressions from Eq.(1.3.12) in Eq. (1.3.13), and keeping in mind that the time derivative gives ω_2 terms, we get for the wave equation

$$\vec{\nabla}\times\vec{\nabla}\times\vec{E}_{\mathrm{n}}(\vec{r}) - \frac{\omega_{\mathrm{n}}^2}{c^2}\varepsilon^{(1)}(\omega_{\mathrm{n}})\bullet\vec{E}_{\mathrm{n}}(\vec{r}) = \frac{4\pi\omega_{\mathrm{n}}^2}{c^2}\vec{P}^{(\mathrm{NL})}(\vec{r})$$ (1.3.15)

The above equation can be simplified to yield solution for the individual cases. So far we have discussed the dielectric tensor and its role in relating the electric field and the electric displacement vector. For a given frequency, substitution of equation 1.3.12 in 1.3.9 yields the following relation between the polarization and the electric field:

$$\vec{P}_n = (\chi^{(1)}\vec{E}_n + \chi^{(2)}{}_{ijk} \otimes \vec{E}_n \bullet \vec{E}_n + \chi^{(3)}{}_{ijkl} \otimes \vec{E}_n \bullet \vec{E}_n \bullet \vec{E}_n + ...) \qquad (1.3.16)$$

where $\chi^{(2)}_{ijk}$ is the second order susceptibility tensor of rank three and $\chi^{(3)}_{ijkl}$ is the third order susceptibility tensor of rank four etc. The $\otimes$ sign in Eq. (1.3.16) denotes the tensor nature of the product. As can be seen from the Eq. (1.3.16), the polarization of the medium depends on the electric field strength in a nonlinear fashion. Very high intensity photon source is necessary to observe such nonlinear effects. The modern Q-switched or mode locked pulsed lasers with pulse widths ranging from few nano-seconds to femto-seconds with optical peak intensities in the range of few Gigawatts per cm^2 are ideal means of studying such nonlinear processes.

1.4   Outline of the Dissertation

In Chapter 1: Introduction, we discuss the need for the novel optical materials and dwelled on basics of nonlinear optics.

In Chapter 2, we discuss the Laser Ablation technique as a possible means to manufacture semiconductor nanoclusters. Different experimental techniques to characterize the third order nonlinearity are discussed here. We introduce the technique called Z-Scan in detail and present results on the passivated laser ablated Si nanocluster film on glass substrate.

In Chapter 3, we introduce the concept of a photonic crystal in the visible spectrum of electromagnetic waves. After reviewing a few earlier works in the field we report a method used to manufacture a three dimensional photonic crystal made up of silica spheres namely silica opal. We then introduce the concept of ion implanting of

silica opal films with silicon, and then give a brief description of the experimental technique used to characterize the same in both linear and nonlinear regime. We discuss the 1-dimensional Bragg reflector model for the photonic crystal.

In Chapter 4, we describe the erbium doped red opal structure and explain the linear and nonlinear optical properties of the structure including the photoluminescence spectra of the same.

In Chapter 5, we introduce a germanium doped red opal structure and describe its various linear and nonlinear optical properties.

In sixth Chapter, we present different applications of these novel optical materials which themselves manifest as future research directions in the novel materials tested during the course of the thesis.

In Chapter 7, we conclude the current dissertation by drawing few broad conclusions based on the study of different materials studied.

CHAPTER 2

LASER ABLATED SILICON NANOCLUSTERS

2.1   Introduction

The main aim of this chapter is to introduce the laser ablation [13], more commonly known as Pulsed Laser Deposition (PLD) [14] as a method for preparation of semiconductor nanocluster. We give a brief description of the laser ablation set-up used to prepare the silicon nanocluster thin films. We further discuss the experimental technique for the characterization of third order nonlinearity in thin films namely Z-Scan. We have devoted Appendix A for describing the theoretical background required for the Z-Scan methodology. We present the results of the experimentation on various gas passivated Si nanocluster films.

2.2   Laser Ablation

Laser ablation is a simple and versatile method for the deposition of thin films of a wide variety of materials. The stoichometric removal of the constituent species from the target during the ablation, as well as small number of control parameters, are two major advantages of PLD over some of the other deposition techniques like Chemical Vapor Deposition (CVD), Molecular Beam Epitaxy (MBE), Metal Organic Chemical Vapor Deposition (MOCVD) etc.

A typical laser ablation setup usually consists of an excimer laser [15] with collimating and focusing optics and a vacuum chamber where the actual film deposition

takes place. The choice of different gases in the excimer laser gives rise to variety of wavelength outputs of the laser for example ArF- 193 nm, KrCl- 222 nm, KrF- 248 nm etc.

2.3   Sample Preparation

The samples containing Si clusters were prepared using the ablation setup shown in Fig 2.1. A KrF excimer laser beam with specifications λ =248 nm, average power, <I>=3W, pulse duration = 8 nS and repetition rate =50 Hz, was focussed to a 100 μm spot size on a silicon wafer target (<100>, n-type, 10^{16} cm^{-3}). The silicon target was cleaned by methanol and HF to remove any native oxide. The glass substrate was cleaned by acetone and methanol. The glass substrate was positioned 3 cm away from Si target We prepared the silicon ablated films under the passivating environment of different gases such as H_2, He, and Ar at 10^{-5} torr. The glass substrate was maintained at room temperature and a typical deposition time was 15 minutes.

2.4   Z-Scan

Z-Scan characterization technique was used to determine the sign and magnitude of refractive index as well as absorption coefficient. This section is further divided into the explanation of Z-Scan [16] technique followed by the experimental configuration used.
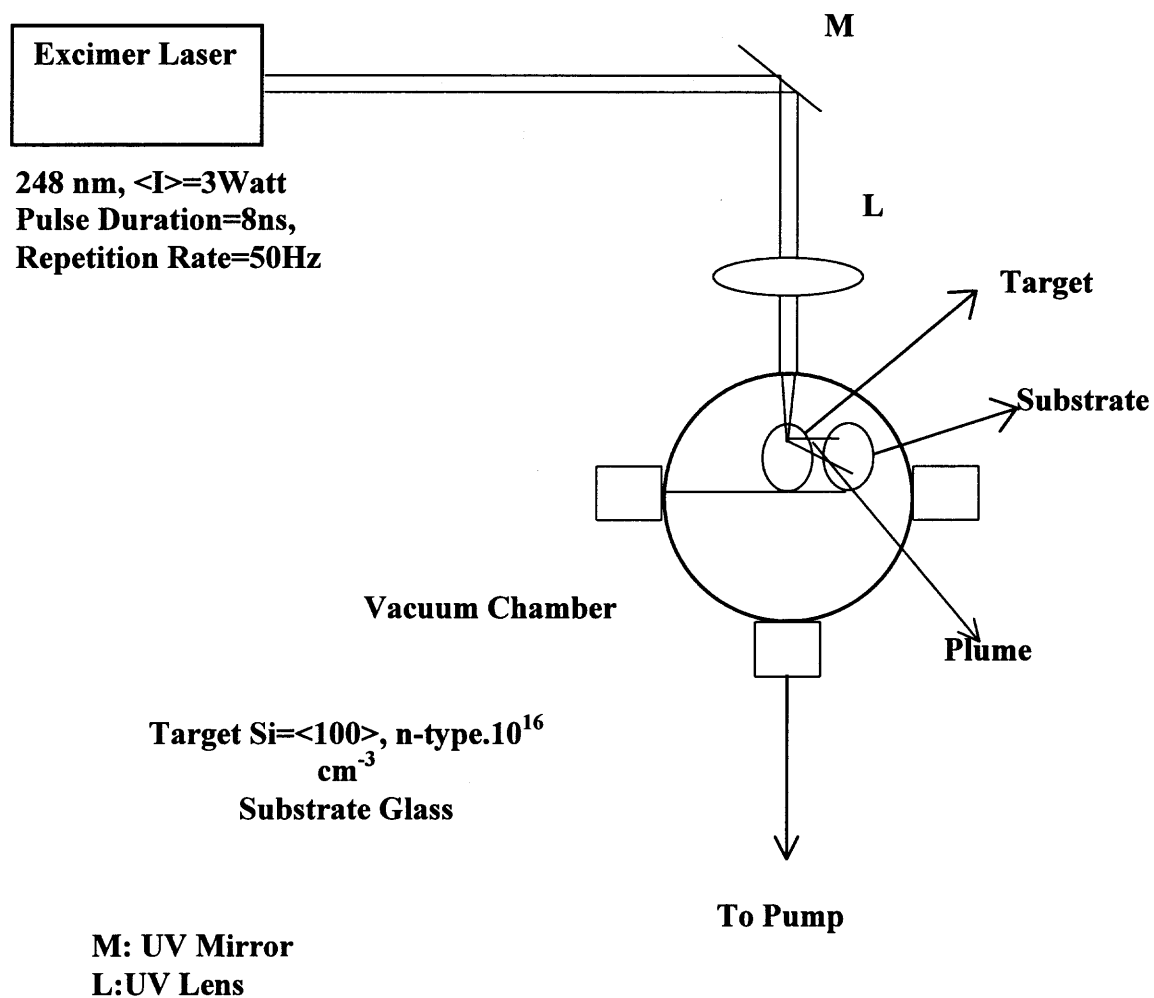
Fig. 2.1   Laser Ablation setup used to produce silicon nanoclusters

2.4.1   Z-Scan Technique

Z-Scan technique can be described as measuring the transmittance of a nonlinear medium with a finite aperture in the far field, as a function of the sample position ' z ' measured with respect to focal plane. In the following paragraphs we explain in detail how such a trace is related to nonlinear refraction of the sample.

To understand the Z-Scan [10], let's assume that the nonlinear index of the thin film under test is positive, and the sample is in prefocal position as shown in Fig. 2.2. The Kerr type nonlinear thin film may be viewed as a lens if we assume that the response of the film follows the transverse light profile. In the far field the beam opens up more owing to combined diffraction from the nonlinear lens and the focussing lens. It remains collimated over shorter distance in the near field; and diverges at larger beam angle in the far field correspondingly reducing irradiance at the detector. When the same sample passes through the focal point to postfocal point position, the positive lensing of the nonlinear thin film tends to reduce beam divergence, which in turn results in increased irradiance at the detector in the far field. Hence one would observe a characteristic valley and peak in transmission spectra when a positive index nonlinear material is scanned from prefocal to postfocal region. The situation is reversed if negatively nonlinear index thin film is under Z-Scan test. The characteristics of the scan are peak and valley as the sample is scanned. In open aperture Z-Scan, we collect the entire light output from the sample. This yields the information on its nonlinear absorption properties. While in the close aperture experiment, we limit the detector reading to light propagating along the ' z ' axis. This yields the information about the nonlinear refraction of the sample.

Sample

Z=0

(b) Prefocal

Detector

$\cdots\cdots\ n_2 > 0$

$--\ n_2 < 0$

Sample

Z=0

(b) Postfocal

Detector
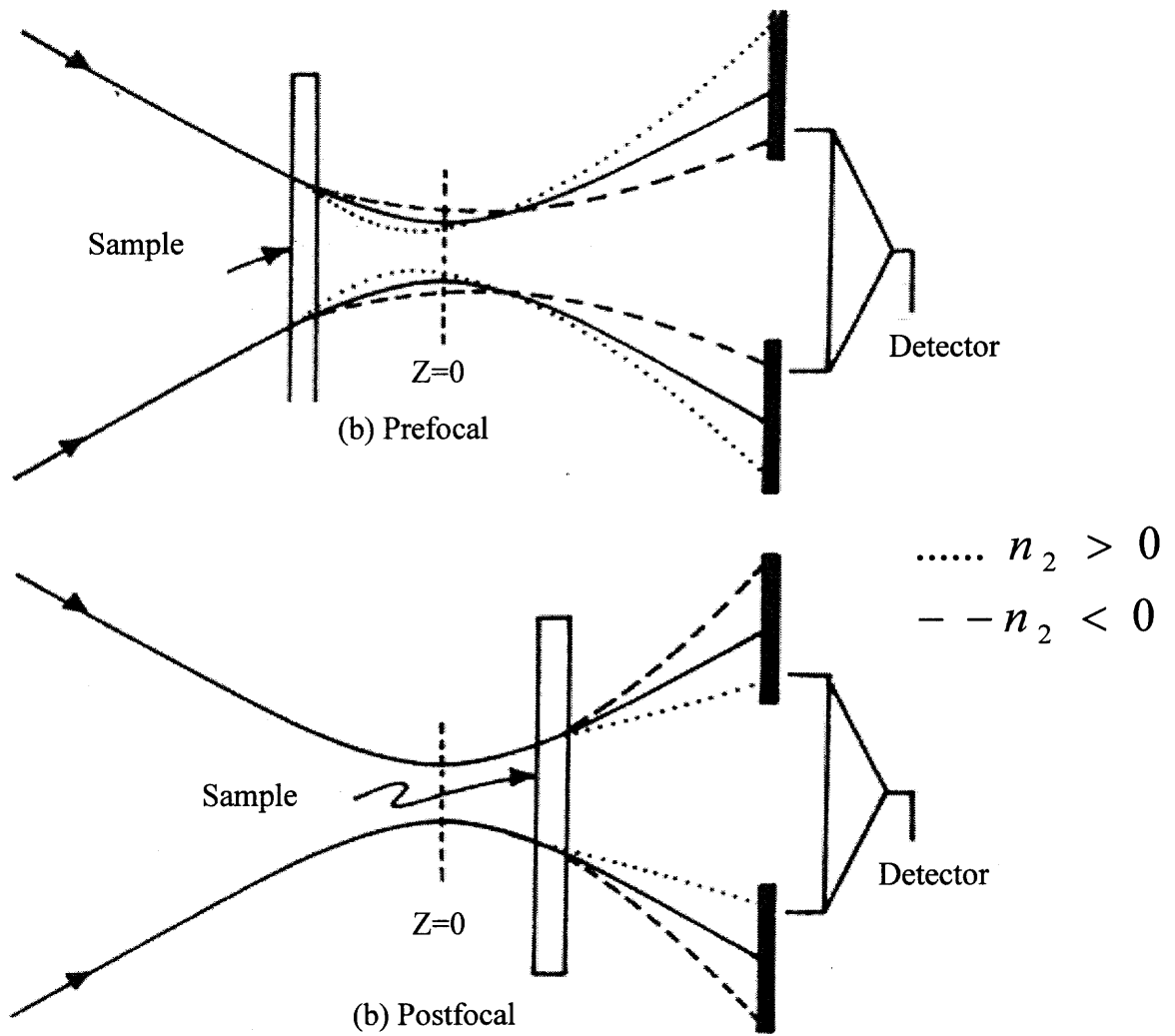
Fig. 2.2   Nonlinear refraction measurement through Z-Scan method (dark lines denote beam propagation without nonlinear sample in the path)

2.4.2   Z-Scan Experimental Setup

The experimental set-up used during Z-Scan is shown in Fig. 2.4, which is completely automated using LabView™ and being. The main laser source used in the experimentation is Q switched Nd:YAG laser which is frequency doubled to give 10 pulses every second each of duration 10 nS at $\lambda = 532$ nm. To perform experiments at other wavelengths, the green ($\lambda = 532$ nm) output from the Nd:YAG pumps a dye laser which generates other output wavelengths. For example solution of Rhodamine B dye prepared in Methanol results in 590 nm, Cresyl Violet dye when prepared in Methanol gives 645 nm and Nile Blue dye when prepared in Methanol results in 710 nm; all of which are pumped with 532 nm from Nd:YAG laser [17].

Both the open aperture and close aperture Z-Scan signatures are collected. During the data collection, care was taken to see that the laser power fluctuations are less than 5% of the peak value. This was done through monitoring the reference signal collected by the beamsplitter in the beam path and writing a small signal processing subroutine in LabView™.

2.5   Experimental Results

In present section we present few of the results at different wavelengths on the silicon ablated films grown on the glass substrate under the different gaseous passivating medium. The curve fitting procedure adopted for the data is by writing a subroutine in KaleidaGraph™, a curve fitting software package. We start the curve fitting procedure by
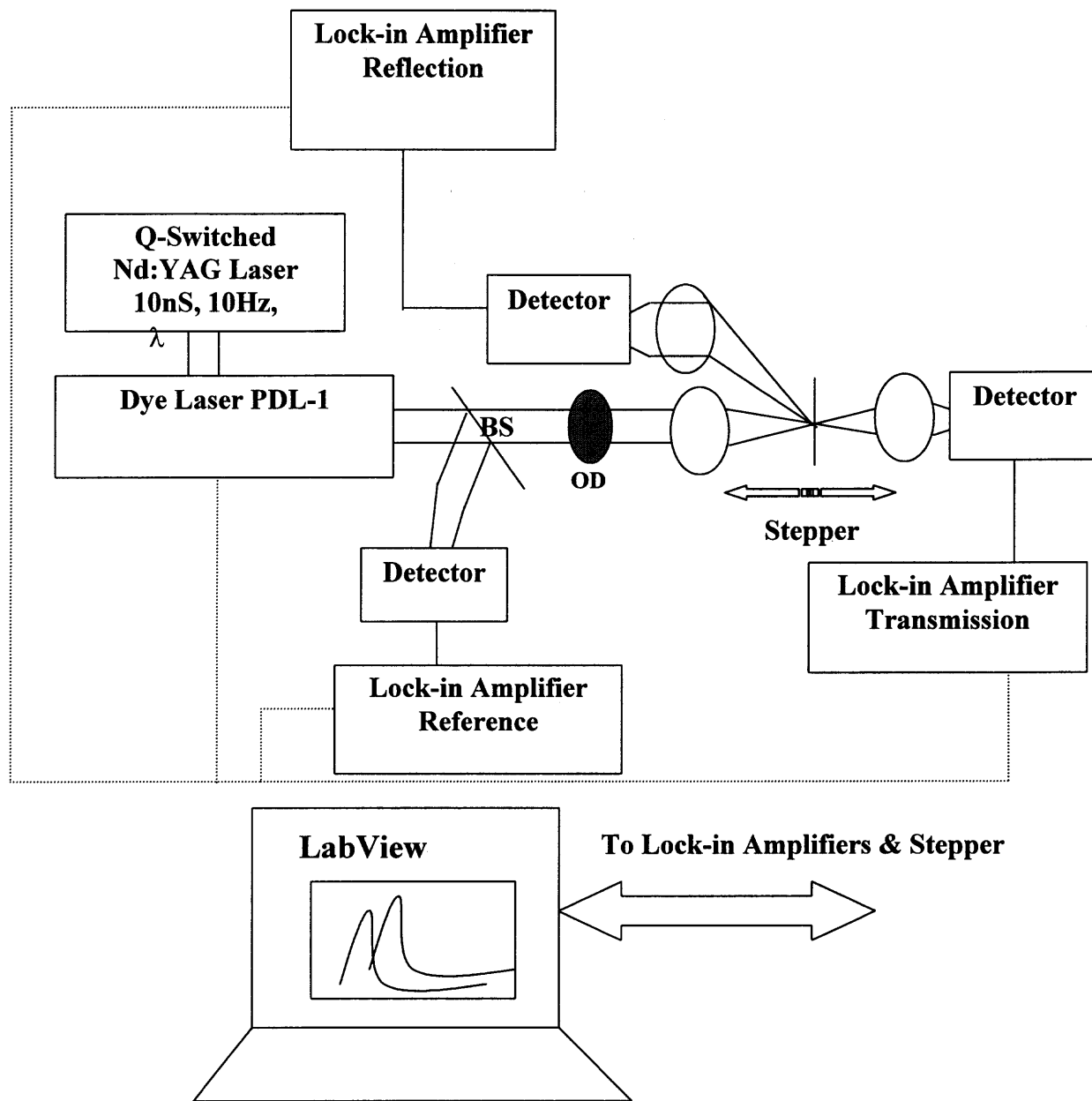
BS: Beam Splitter
OD: Neutral Density Filter

Fig 2.3   Z-Scan experimental setup

giving the initial guess value for the w_0 i.e. the beam waist for the open aperture data according to Eq. (A.27) and the best fit value of the same parameter returned by the program is later used for the close aperture curve fitting according to Eq. (A.14). The error in fitting the curve is observed to be less than 5%.

In figure 2.4, we show a representative Z-Scan normalized transmission data as a function of 'z' coordinate for close aperture, open aperture experiments. Negative values of 'z' represent sample being closer to the lens and positive values of 'z' represents sample closer to the detector placed in the far field. One can clearly observe the close fit between the theory and experimental values obtained through our Z-Scan experiments. We repeated the same curve fitting procedure for all the three passivated samples tested at different wavelengths.

In following graph, presented in figure 2.5, we present the maximum change in nonlinear refractive index Δn as a function of λ, the wavelength at which the Z-Scan experiment is performed (the intensity values are in the decade 1-10MW/cm^2) [18]. One can observe the variation in the Δn values at different wavelengths for the samples passivated in different gases.

2.6   Discussion

The variation in Δn for different silicon ablated samples with respect to different wavelengths at approximately similar incident peak powers were presented in figure 2.5. The graphs clearly show the variation of Δn for different passivating gases. For example
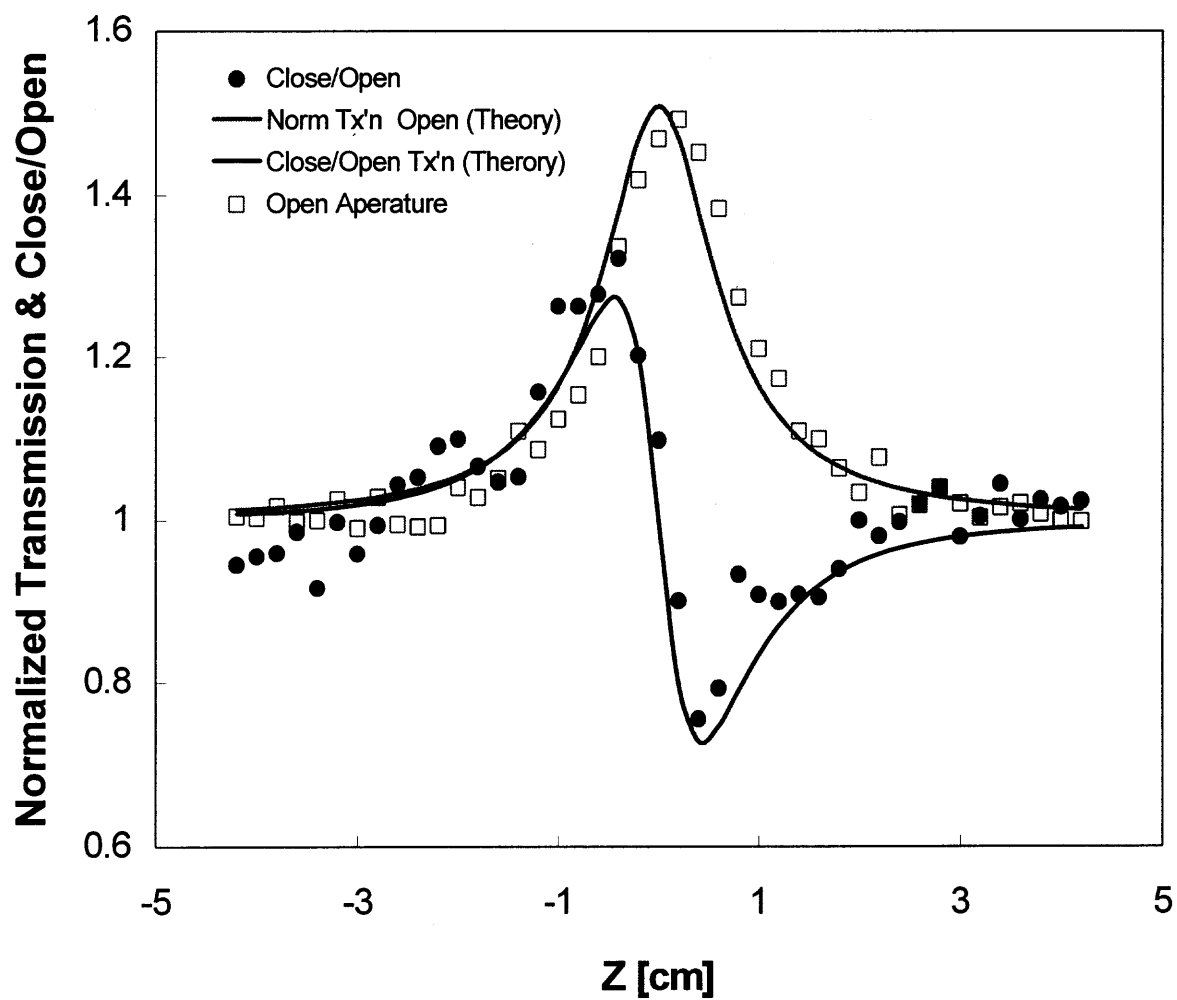
Fig. 2.4   Typical Z-Scan data for the passivated Si nanocluster samples
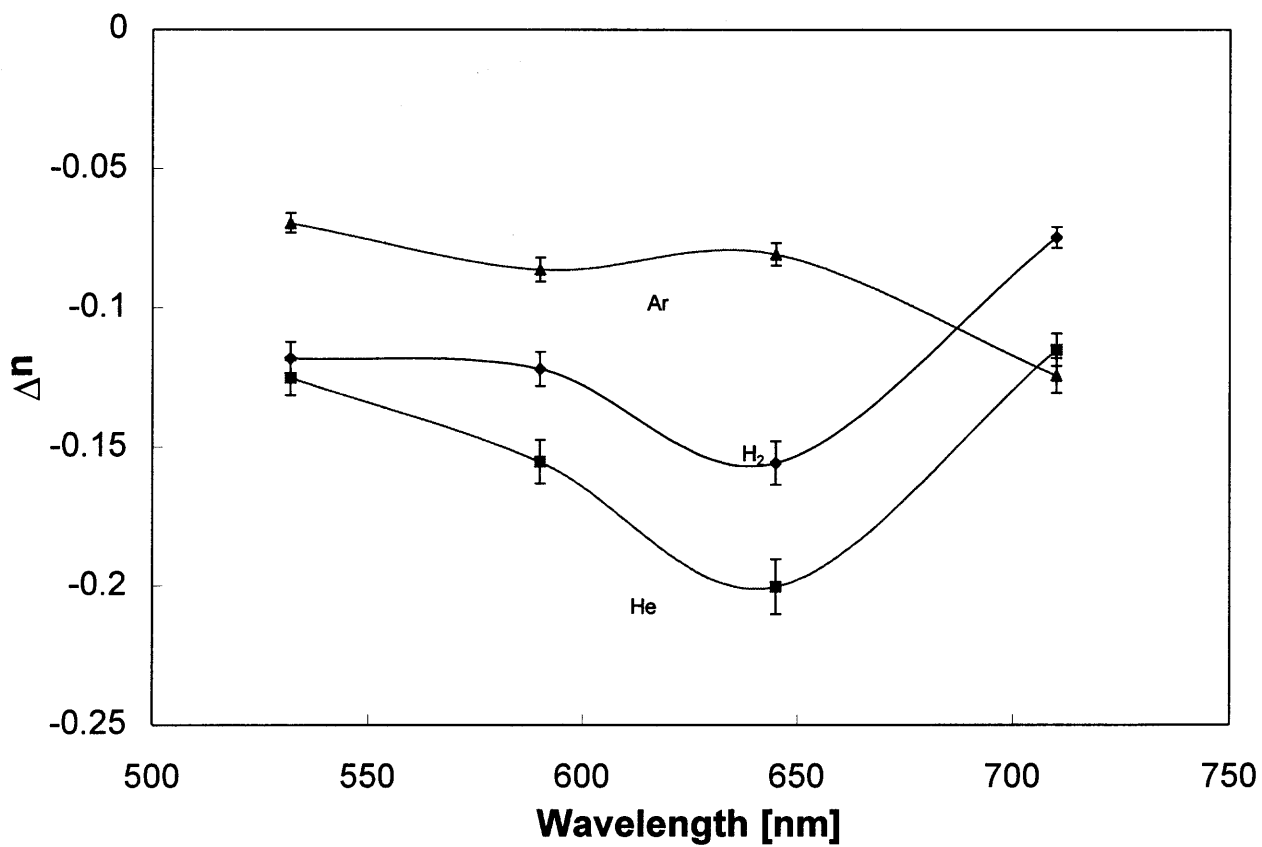
Fig 2.5 Δn values for samples with silicon nanoclusters passivated in different gases

the films passivated in He show the maximally negative Δn as compared to those passivated under H_2 and Ar in that order. The present Δn results are about $1/10^{th}$ to $1/2$ of the non passivated films at $\lambda = 532$ nm [19]. Our Δn results when compared to the porous silicon are larger by an order of magnitude.

Our results elucidate the role of surface states in the nonlinear process. Linear absorption measurements indicate an absorption peak around $\lambda = 650$ nm. Samples grown in He or H_2 did exhibit an enhanced nonlinear refraction in that spectral range whereas samples grown in Ar environment exhibited that tendency at longer wavelength. This characteristic of samples grown in Ar is similar to the characteristics of films grown in high vacuum, with the exception of a much lower linear values in the present case. Since all films show a reduced nonlinearity when compared to films grown in vacuum, one may lead to believe that the crystallographic nature of these films is different. Films grown in high pressure tend to possess cubic symmetry, whereas films grown in vacuum of 10^{-6} torr tend to show more of hexagonal symmetry [20,21]. This point is still under investigation. Though all films are grown under the same gas pressure, no obvious dependence on the gas mass density is observed. It is widely believed that scatterings between the ablated species and the ambient gas is critical to the nucleation process. Let us examine the gas equation of states $PV = NRT$, where P is pressure, V is volume R is gas constant, T is temperature and N is number of gas moles in the volume. Since all parameters are kept constant the ablation process should not discriminate between various gases unless a chemical reaction takes place. This may be true for hydrogen but

not for other gases. Thus, one may conclude that unlike a simple evaporation, laser ablation is sensitive to atomic mass of the gas in the growth chamber.

CHAPTER 3

SILICON IMPLANTED SILICA OPAL

3.1   Introduction

The three-dimensional periodic structures made at different pitch size, so called "Photonic Crystal [22]" along the electromagnetic wave spectra have been a topic of high interest research for the last decade. Photonic crystals have the similar effect on photons as semiconductor crystals have on electrons.

In this chapter, after a brief review of the earlier work done on the topic of photonic crystal, we give the procedure of growing such a photonic crystal namely the Silica Opal. After reviewing few basic linear optical properties of this opal we also present the one-dimensional simulation for this structure. We further wish to present the nonlinear experimentation performed on the silicon implanted opal structure.

3.2   Literature Review

The concept of electronic band structure is well known from solid state physics and electronics: due to the periodic potential variations in a crystal, electron motion is restricted and electrons of certain energy are not allowed to travel through the crystal at all. This phenomenon leads to " forbidden bands" and forms the basis of the most microelectronic devices known to date. In analogy to electronic band gaps in a semiconductor crystal with a lattice constant on the order of fractions of nano-meter range, a periodic refractive index modulation created by a lattice composed of dielectric building blocks could yield a band gap for photons energies or equivalently frequencies.

This was the basic idea behind the original proposals of a photonic crystal as conceived by Eli Yablonovitch [23] and Sajeev John [24] in 1987. While Yablonivitch's approach was more concentrated on inhibiting the spontaneous emission from semiconductors, Sajeev John was concerned about the localization of the photon. After few experiments in the microwave region of the electromagnetic spectrum [25], [26] it was the explosive growth of optical communication in last decade which made scientist to explore novel materials operative at visible and near IR region which are of great interest to communication society.

The processing of photonic crystal can be divided in two different paths. In one, selective patterning and etching of the semiconductor wafers would lead to a three dimensional photonic crystal [27]. The other approach uses a slow sedimentation of colloidal particles of silica [28] or TiO_2 [29] yielding the three-dimensional photonic structure.

3.3   Preparation of Silica Opal - A Photonic Crystal

Precious opals are composed of amorphous silica spheres and their colors are due to the light diffraction from regular packing of these uniform silica spheres. These silica opals are available in nature [30]. The silica spheres, 150-400 nm in diameter, are of colloidal size, and are prepared by a well-known methodology called TEOS [31], [32]. The face centered cubic (FCC) structure of synthetic opal which consist of sub-micron size silica spheres can be grown on glass or quartz substrates by self-assembly.

The nano meter size silica spheres in alcohol are prepared by the hydrolysis of tetraethoxysilane (TEOS) in a mixture of ammonium hydroxide, water and ethanol.

Spherical silica particles are obtained when sufficient ammonia is present in the initial reaction mixture at room temperature. The final opal size depends mainly on the initial water and ammonia concentration. Silica powder is then obtained by evaporating the excess ethanol and ammonia and heated at 600^0C for three hours. Then, the particles are dispersed in ethanol again to form a suspension. The opal films are then self-assembled by laying the suspension on fused silica or quartz.

Owing to the Bragg's law, opal samples with silica diameter of 200, 245 and 300 nm scattered blue, green and red colors respectively in reflection when viewed at normal angles. The brightness of the reflection also gives an estimate of the periodicity and uniformity of the grown opal films. A schematic of the Bragg reflection occurring in the opal structure is shown in figure 3.1.

3.4   Ion Implantation of Si

The red (i.e. silica ball diameter = 300 nm) opal films were ion implanted [33] at room temperature by Si$^+$ ions at 400-KeV and current of approximately 30μA to a dose of 6×10^{17} cm^{-2} resulting in a peak excess Si concentration of 2×10^{22} cm^{-3}. The red opal substrate was air cooled during Si implantation eliminating heat damages to the periodic opaline structure. These ion implanted opal samples were further annealed at 1100 ^{0}C for 1 hour in flowing 4%H$_2$ in Ar to form surface passivated Si nanocrystals inside the silica spheres. The projected range of the implanted ions was 600 nm with an average full width at half height of 300 nm.
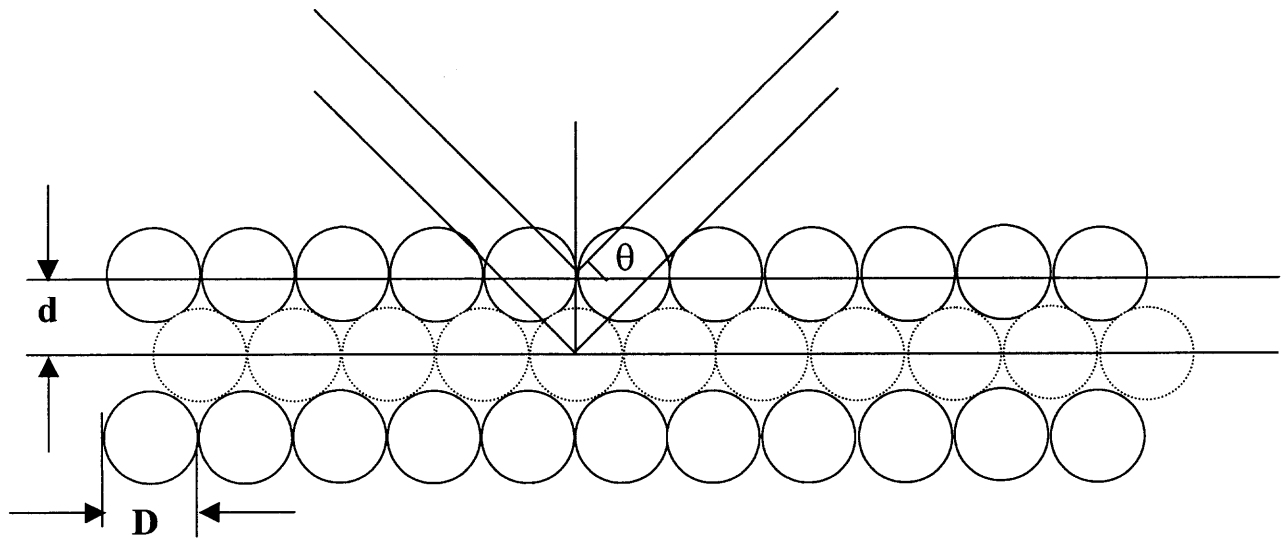
$$2\ n\ d\ \sin\theta=\lambda$$

$$d=0.8165\ D$$

$$D_{red}=300\ nm \qquad \lambda_{red}=660\ nm$$

$$D_{green}=245\ nm \qquad \lambda_{green}=542\ nm$$

Fig 3.1   Schematic of the Bragg reflection in opal

3.5   Experimentation on Si Implanted Opal Structure

This section is subdivided into two parts mainly linear and nonlinear characterizations. We start by analyzing a few of the linear optical properties including the white light reflection and transmission of the sample and 'virgin' opal. We discuss in detail the one-dimensional modeling of the silica opal structure. We then proceed to describe the nonlinear experimentation performed on these sample.

3.5.1   Scanning Electron Micrograph Pictures

We took the SEM [34] pictures of the nonimplanted and implanted red opal samples with the SEM model ESEM2020, EDX Super Dry.

One can appreciate the regularity of opal sphere in the silica opal in the Scanning Electron Microscope picture shown in Fig 3.2. of the red opal implanted by silicon. The other SEM picture in Fig. 3.3 shows the cross sectional view of the silicon implanted red opal sample. One can easily see the swollen opal film after annealing although the underlying opal film is intact. The swelling has taken place only in the first four layers of the opaline structure as viewed from the SEM picture. This result is consistent with average aimed projected range of the implantation.

In fig. 3.4, we show the SEM picture of the silicon implanted red opal matrix with average cluster size 3-4 nm and one can see the non-swollen opal matrix.
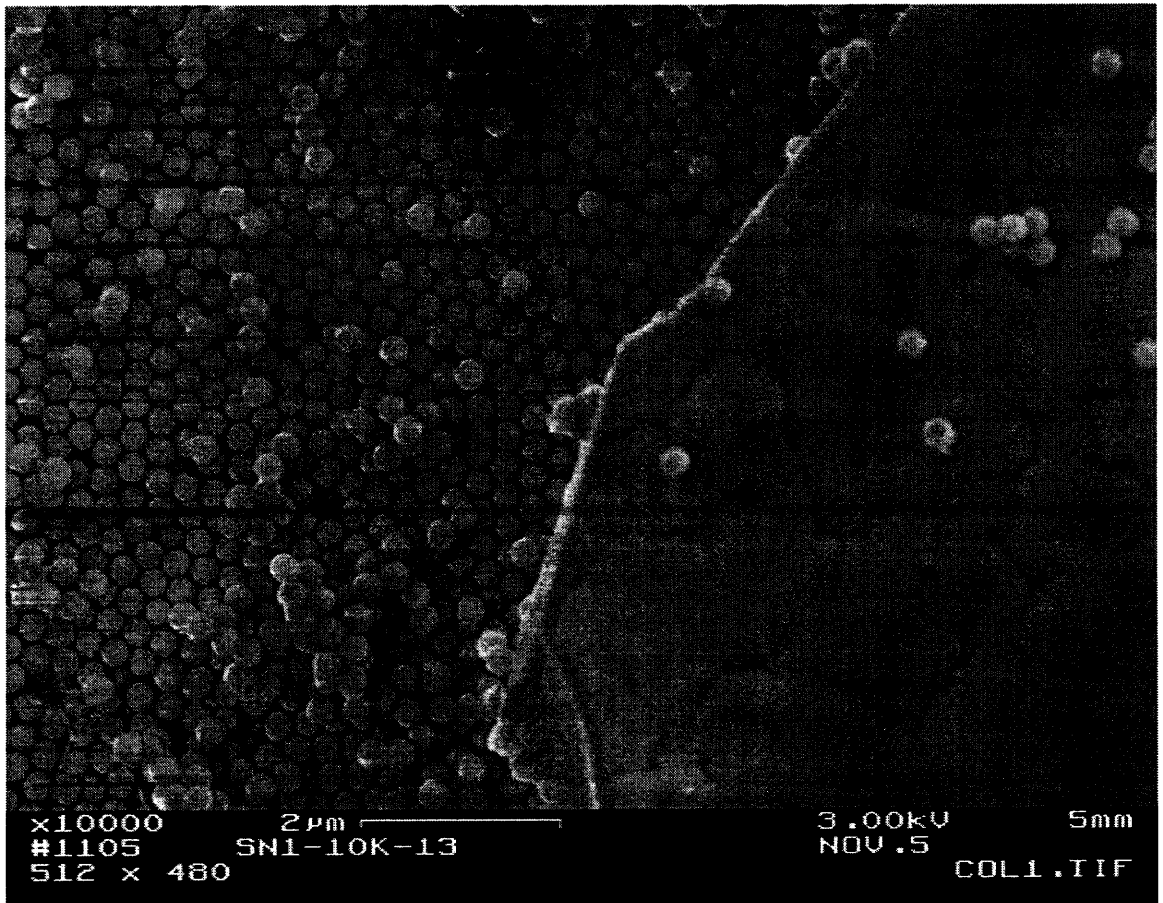
Fig. 3.2   A scanning electron microscope (SEM) picture of a silicon ion implanted 'red' opal. The featureless region is the swollen top layer.
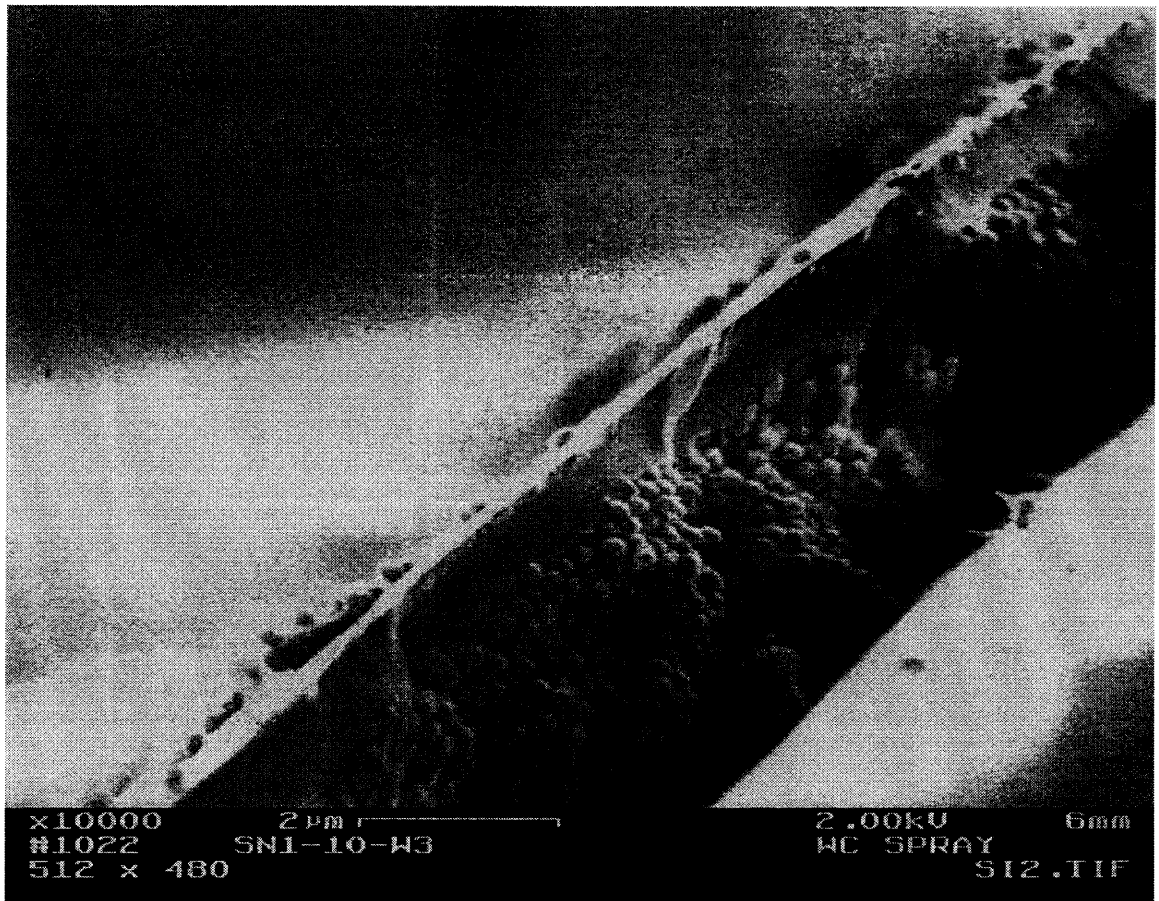
Fig. 3.3   A scanning electron microscope (SEM) picture of a cross section of a silicon ion implanted 'red' opal. The smooth featureless region indicates the swollen region.
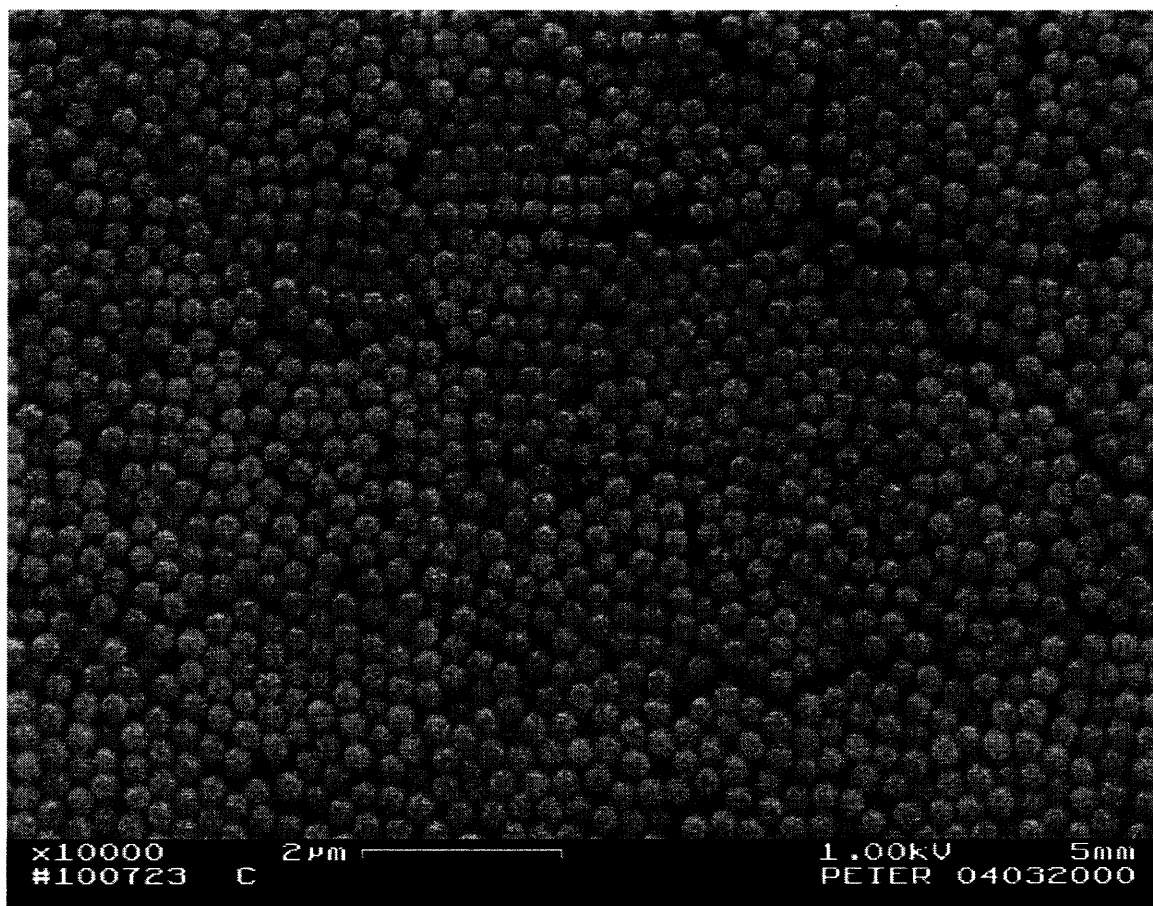
Fig. 3.4   Silicon implanted opal with cluster size 3-4 nm and non-swollen opal matrix

3.5.2   Linear Experimentation

Linear white light reflection and transmission experiments [35] on non-implanted and implanted opaline samples were made to verify the presence of a periodic structure and to determine the effective refractive index of the samples.

The linear white light reflection and transmission experiment is done with the help of SPEX white light (Tungsten filament) source and monochromator (CD2B). The experimental configuration is shown in figure 3.5.

The experiments are performed on nonimplanted opal and repeated for implanted samples. The reflection data were normalized to the input intensity. Data for nonimplanted and ion implanted red opal samples as a function of wavelength are presented in figures 3.6 and 3.7 respectively. One can easily appreciate the presence of periodic nano size silica opal structure by the typical Bragg resonance seen in figure 3.4 for the non implanted sample. From Fig. 3.7 one can infer the survival of the periodic opal layers beneath the first few silicon implanted layers. This has already been confirmed through the cross-sectional SEM picture in figure 3.3.

3.5.2.1   One Dimensional Modeling of the Photonic Crystal

Here we model the 3-dimensional photonic crystal in our case namely silica opal as a periodic layered media. Periodic layered media are a special class of layered media in which layers of dielectric material are stacked in a periodic fashion. Wave propagation in these media is directly correlated to the remarkable colors of some of the beetles and butterflies and silvery skin and scales of some of the fish.
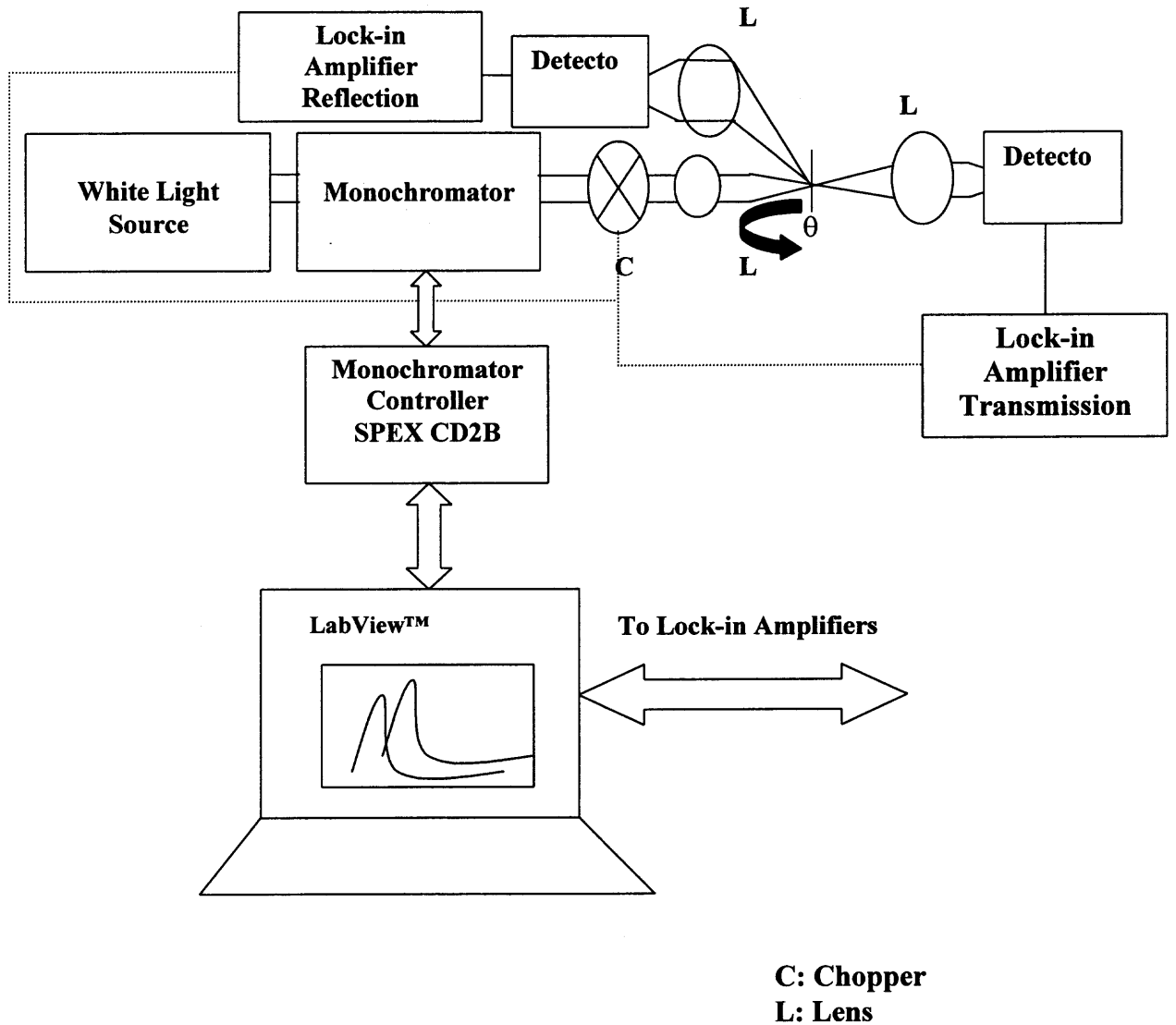
Fig. 3.5   Experimental setup for the linear characterization of ion implanted opal
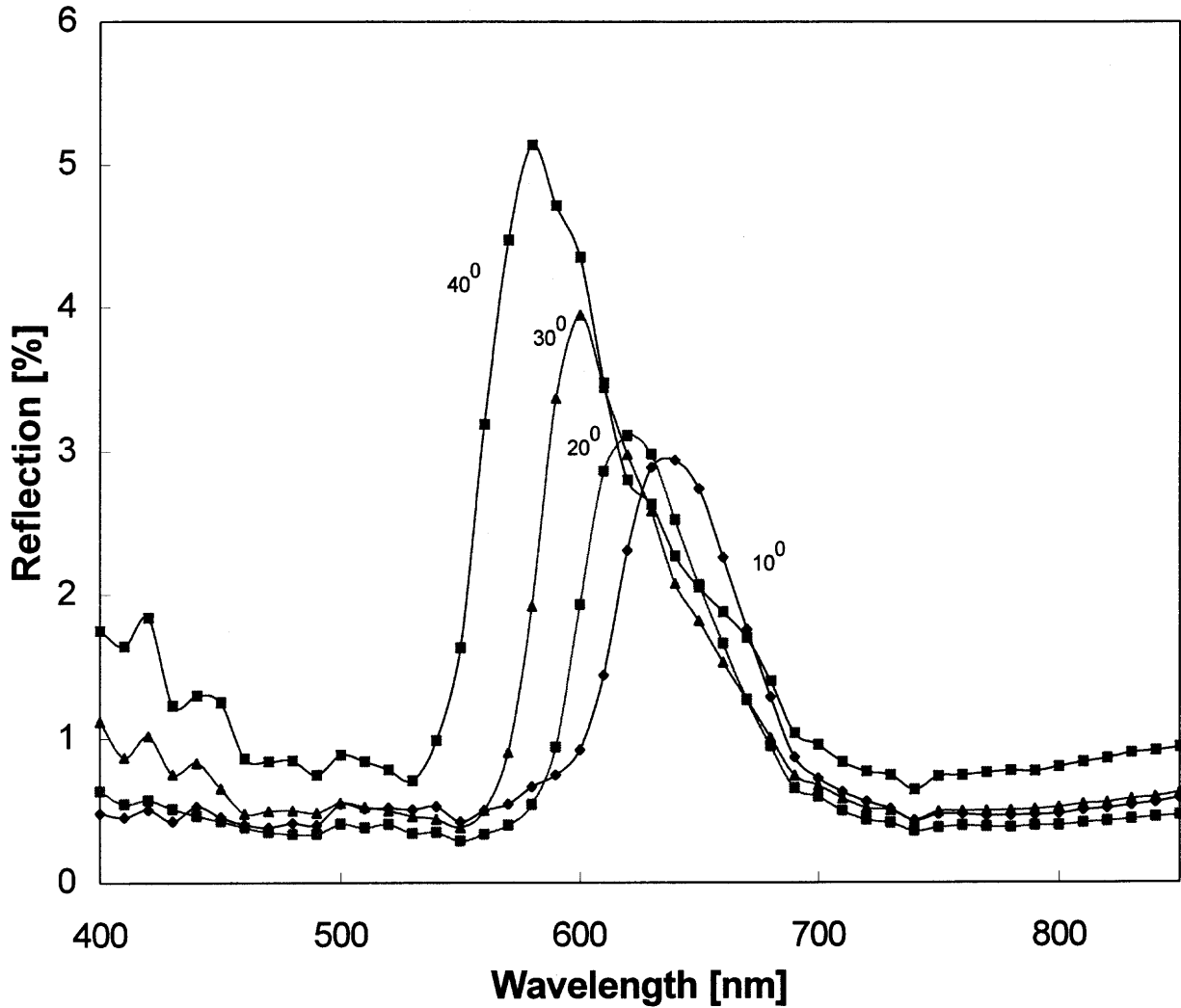
Fig. 3.6   White light reflection from the nonimplanted opal as a function of angle of incidence and wavelength.
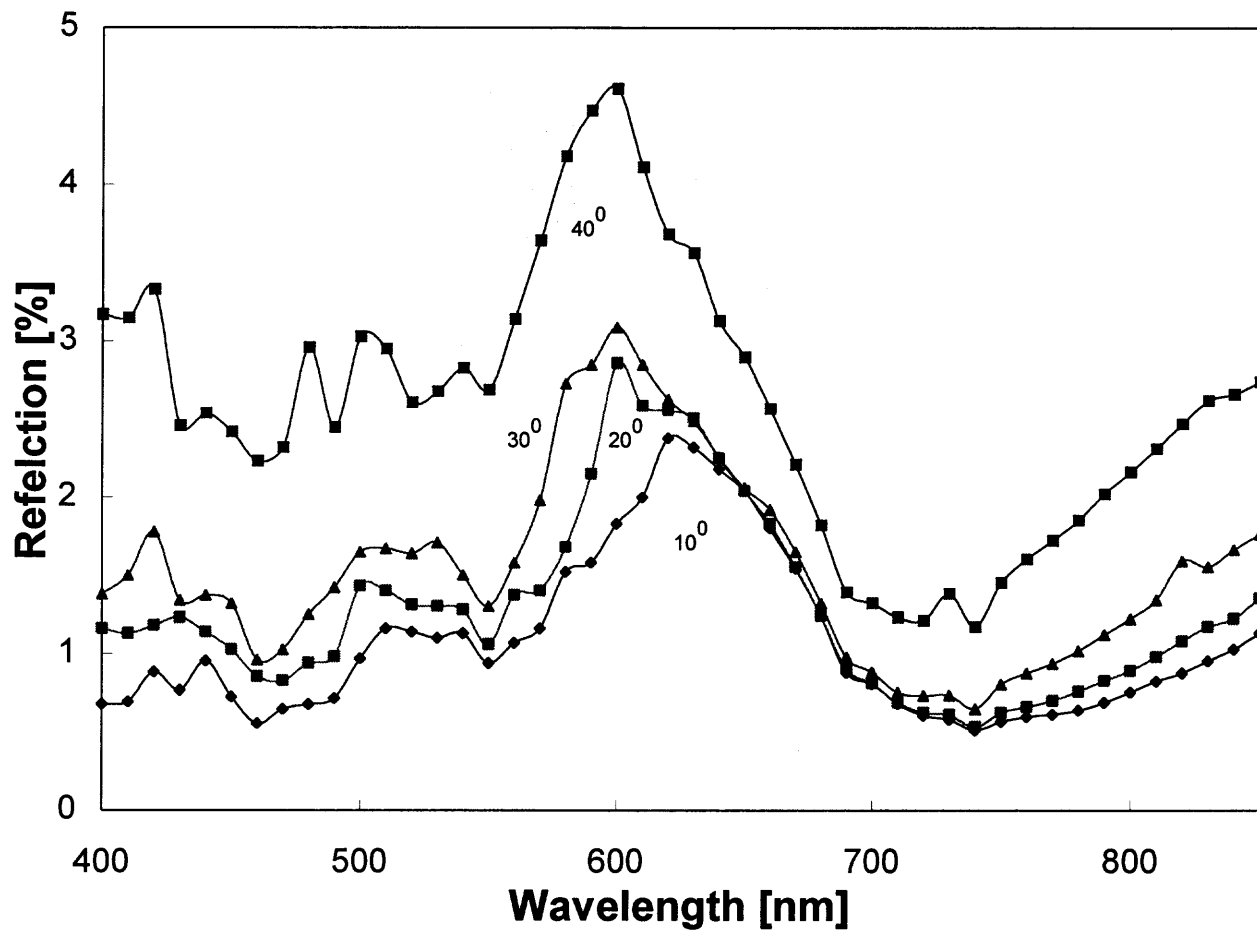
Fig. 3.7   White light reflection from the Si implanted red opal as a function
of angle of incidence and wavelength

Reflection Coefficient of a Periodic Layered Media [36], [37]

Consider a plane wave incident on a stratified isotropic medium with boundaries at

$$z = -d_0, -d_1, -d_2, ..., -d_n$$

The $(n+1)$ th region is semi-infinite. The permittivity and permeability in the region is

denoted by $\varepsilon_1, \varepsilon_2$ and μ_1, μ_2 respectively. Such a structure is represented in Fig. 3.8. The

plane wave is incident from region 0 and has the plane of incidence parallel to

$x - z$ plane. This implies that all field vectors are dependent only on x and z only and

independent of y. Since $\partial / \partial y = 0$, the Maxwell equations in any region 1 can be

separated into TE and TM components governed by E_{ly} and H_{ly}. We obtain,

$$H_{ix} = -\frac{1}{i\omega\mu_l} \frac{\partial}{\partial z} E_{ly} \qquad (3.5.2.1.1)$$

$$H_{iz} = -\frac{1}{i\omega\mu_l} \frac{\partial}{\partial x} E_{ly} \qquad (3.5.2.1.2)$$

$$\left(\frac{\partial^2}{\partial x^2} + \frac{\partial^2}{\partial z^2} + \omega^2 \mu_l \varepsilon_l \right) E_{ly} = 0 \qquad (3.5.2.1.3)$$

$$E_{ix} = \frac{1}{i\omega\varepsilon_l} \frac{\partial}{\partial z} H_{ly} \qquad (3.5.2.1.4)$$

$$E_{iz} = -\frac{1}{i\omega\varepsilon_l} \frac{\partial}{\partial x} H_{ly} \qquad (3.5.2.1.5)$$

$$\left(\frac{\partial^2}{\partial x^2} + \frac{\partial^2}{\partial z^2} + \omega^2 \mu_l \varepsilon_l \right) H_{ly} = 0 \qquad (3.5.2.1.6)$$

The TE waves are completely determined by the first three equations while the later three

equations are for the TM waves. One can also easily observe the duality in the TE and

TM equations.
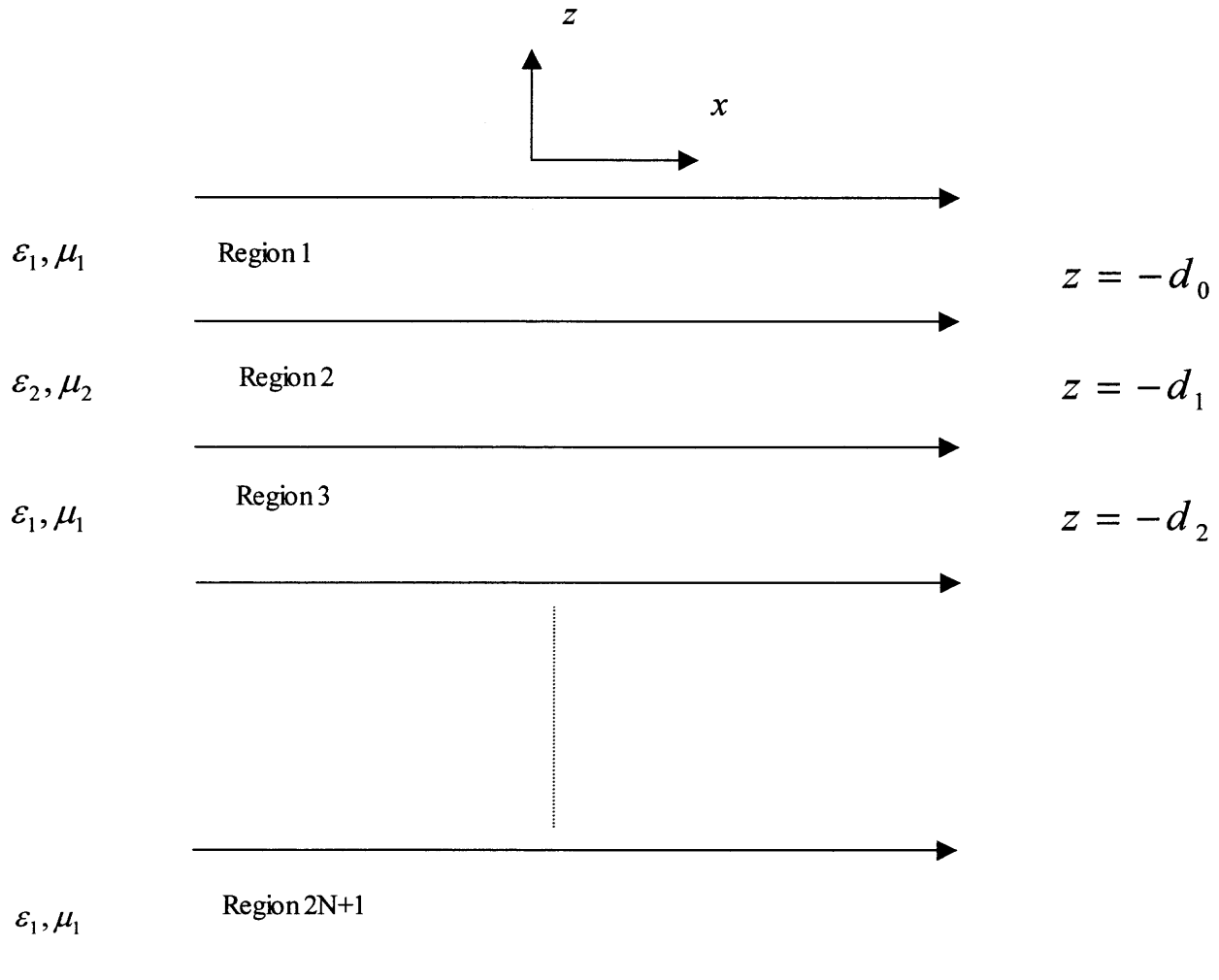
Fig. 3.8 A stratified medium with alternate layers of permittivities ε_1 and ε_2

For a TE plane wave, $E_y = E_0 e^{-ik_z z + ik_x x}$, incident on the layered medium, the total field in region l can be written as

$$E_{ly} = \left(A_l e^{ik_{lz} z} + B_l e^{-ik_{lz} z}\right) e^{ik_x x} \qquad (3.5.2.1.7)$$

$$H_{lx} = -\frac{k_{lz}}{\omega \mu_l}\left(A_l e^{ik_{lz} z} - B_l e^{-ik_{lz} z}\right) e^{ik_x x} \qquad (3.5.2.1.8)$$

$$H_{lz} = \frac{k_{lx}}{\omega \mu_l}\left(A_l e^{ik_{lz} z} + B_l e^{-ik_{lz} z}\right) e^{ik_x x} \qquad (3.5.2.1.9)$$

One can easily see that the solution of (3.5.2.1.7) satisfies the Helmholtz equation in (3.5.2.1.3). We obtain the dispersion relation by substituting equation (3.5.2.1.7) into equation (3.5.2.1.3) to get

$$k_{lz}^2 + k_x^2 = \omega^2 \mu_l \varepsilon_l \qquad (3.5.2.1.10)$$

We have not written subscript l for the x component of $\bar{k}$ as a consequence of phase matching conditions. Truly, there are multiple reflections and transmissions in each layer l. The amplitude thus represents all wave components that have a wave velocity component along positive $\bar{z}$ direction, and B_l represents those with velocity component along negative $\bar{z}$ direction.

We may also note that in region 0 where $l = 0$,

$$A_0 = RE_0 \qquad (3.5.2.1.11)$$

$$B_0 = E_0 \qquad (3.5.2.1.12)$$

In region t where $l = n + 1 = t$, we have

$$A_t = 0 \qquad (3.5.2.1.13)$$

$$B_t = TE_0 \qquad (3.5.2.1.14)$$

because region t is semi-infinite and there is no wave propagating with a velocity component in the positive $\vec{z}$ direction. We denote the transmitted amplitude by T.

The wave amplitudes A_l and B_l are related to wave amplitudes in the neighboring regions by the boundary conditions. At $z = -d_l$, boundary conditions require that E_y and H_x be continuous. We obtain

$$A_l e^{-ik_{lz}d_l} + B_l e^{ik_{lz}d_l} = A_{l+1} e^{-ik_{(l+1)z}d_l} + B_{l+1} e^{ik_{(l+1)z}d_l} \qquad (3.5.2.1.15)$$

$$\frac{k_{lz}}{\mu_l}\left[A_l e^{-ik_{lz}d_l} - B_l e^{ik_{lz}d_l}\right] = \frac{k_{(l+1)z}}{\mu_{l+1}}\left(A_{l+1} e^{-ik_{(l+1)z}d_l} - B_{l+1} e^{ik_{(l+1)z}d_l}\right) \qquad (3.5.2.1.16)$$

There are $n+1$ boundaries which gives rise to $(2n+2)$ equations. In region 0, we have an unknown reflection coefficient R and in region t, we have an unknown transmission coefficient T. There are two unknowns namely, A_l and B_l in each of the regions $l = 1,2,3,....,n$. Thus we have a total of $(2n+2)$ unknowns from $(2n+2)$ linear equations. This systems of equation can be solved by in the matrix form with the unknowns forming a $(2n+2)$ column matrix and the coefficients forming a $(2n+2) \times (2n+2)$ square matrix. And the solution is obtained by inverting the square matrix. With this procedure being tedious although straightforward; we describe a simpler method to solve the problem.

a. Reflection Coefficients:

Since we are interested in finding the reflection coefficient for the layered medium, we derive below the closed-form formula for R. This is obtained by solving (3.5.2.1.15) and (3.5.2.1.16) for A_l and B_l to obtain,

$$A_l e^{-ik_{lz}d_l} = \frac{1}{2}\left(1 + p_{l(l+1)}\right)\left(A_{l+1} e^{-ik_{(l+1)z}d_l} + R_{l(l+1)} B_{l+1} e^{ik_{(l+1)z}d_l}\right) \qquad (3.5.2.1.17)$$

$$A_l e^{ik_{lz}d_l} = \frac{1}{2}\left(1 + p_{l(l+1)}\right)\left(R_{l(l+1)}A_{l+1}e^{-ik_{(l+1)z}d_l} + B_{l+1}e^{ik_{(l+1)z}d_l}\right) \qquad (3.5.2.1.18)$$

where

$$p_{l(l+1)} = \frac{\mu_l k_{(l+1)z}}{\mu_{l+1} k_{lz}} \qquad (3.5.2.1.19)$$

for TE waves and $\qquad R_{l(l+1)} = \dfrac{1 - p_{l(l+1)}}{1 + p_{l(l+1)}} \qquad (3.5.2.1.20)$

is the reflection coefficient for waves in region l, caused by the boundary separating regions l and $l+1$. We note from equation (3.5.2.1.19) that,

$$p_{(l+1)l} = \frac{1}{p_{l(l+1)}} \qquad (3.5.2.1.21)$$

implying

$$R_{(l+1)l} = -R_{l(l+1)} \qquad (3.5.2.1.22)$$

Hence the reflection coefficient in region $l+1$, $R_{(l+1)l}$, caused by the boundary separating regions $l+1$ and l, is equal to the negative of $R_{(l+1)l}$.

Calculating the ratio of A_l and B_l i.e of equations (3.5.2.1.17) and (3.5.2.1.18) we get,

$$\frac{A_l}{B_l} = \frac{e^{i2k_{lz}d_l}}{R_{l(l+1)}} + \frac{\left[1 - \left(1/R^2_{l(l+1)}\right)\right]e^{i2(k_{(l+1)z} + k_{lz})d_l}}{\left[1/R_{l(l+1)}\right]e^{i2k_{(l+1)z}d_l} + \left(A_{l+1}/B_{l+1}\right)}$$

$$= \frac{e^{i2k_{lz}d_l}}{R_{l(l+1)}} + \frac{\left[1 - \left(1/R^2_{l(l+1)}\right)\right]e^{i2(k_{(l+1)z} + k_{lz})d_l}}{\left[1/R_{l(l+1)}\right]e^{i2k_{(l+1)z}d_l}} + \frac{A_{l+1}}{B_{l+1}} \qquad (3.5.2.1.23)$$

Through equation (3.5.2.1.23) we have introduced notation for the continued

fraction i.e. expressing $\left(A_l \big/ B_l \right)$ in terms of $A_{l+1} \big/ B_{l+1}$ and so on, till the last region

namely t, where, $A_t \big/ B_t = 0$, is reached.

The reflection coefficient due to the layered medium is $R = A_0 \big/ B_0$. We get,

$$R = \frac{e^{i2k_z d_0}}{R_{01}} + \frac{\left[1 - \left(1 \big/ R_{01}^2 \right)\right] e^{i2(k_{1z} + k_z)d_0}}{\left(1 \big/ R_{01} \right) e^{i2k_{1z}d_0}} + \frac{e^{i2k_{1z}d_1}}{R_{12}} + \frac{\left[1 - \left(1 \big/ R_{12}^2 \right)\right] e^{i2(k_{2z} + k_{1z})d_1}}{\left(1 \big/ R_{12} \right) e^{i2k_{2z}d_1}} + \ldots\ldots +$$

$$\frac{e^{i2k_{(n-1)z}d_{n-1}}}{R_{(n-1)n}} + \frac{\left[1 - \left(1 \big/ R_{(n-1)n}^2 \right)\right] e^{i2(k_{nz} + k_{(n-1)z})d_{n-1}}}{\left(1 \big/ R_{(n-1)n} \right) e^{i2k_{nz}d_{n-1}}} + R_{nt} e^{i2k_{nz}d_n} \qquad (3.5.2.1.24)$$

This closed-form solution is programmed using MATLAB and MathCad to obtain the

1-dimensional equivalence of the three dimensional photonic crystal in our case

namely silica opal.

A typical reflection data, as a function of wavelength and normalized to input

intensity, is shown in figure 3.9, for a red opal nonimplanted sample at an angle of

incidence of $\theta = 20^0$ with respect to normal to the sample. The fit obtained by the

model is justified because the beam spot size was large thus emulating a plane wave.

The state of polarization was perpendicular to the plane of incidence i.e. E-

polarization. The one-dimensional curve fit of the same is shown on the same figure

by dark lines. The one-dimensional model is based on a periodic structure made of

succession of layers with alternating refractive indices, which correspond to mixed air
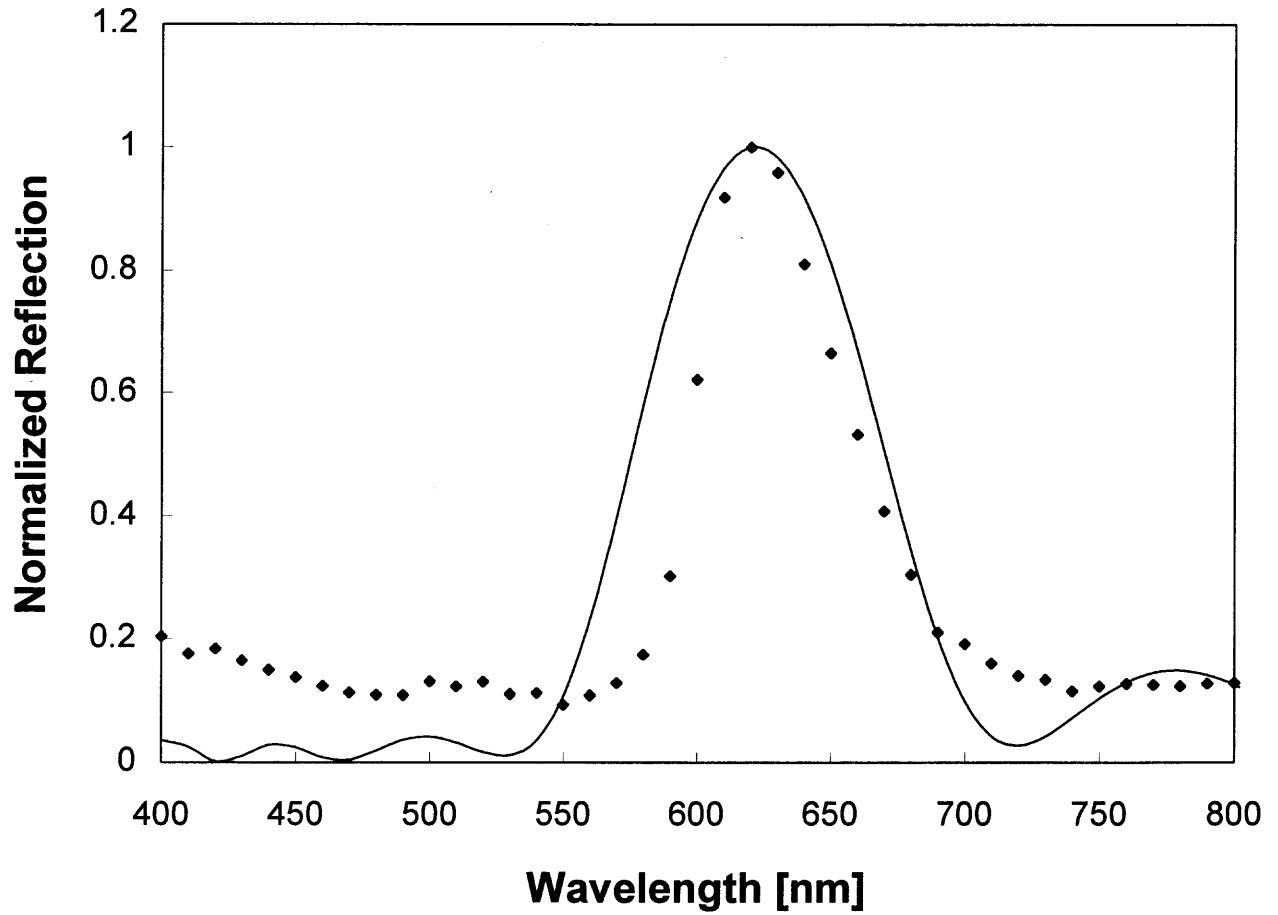
Fig. 3.9   One dimensional model fit to the experimental data for the

red opal substrate (The peak reflection is set to unity)

and glass layer (layer 1) and pure core silica layer (layer 2). Thus in our case, a 300 nm diameter size opal structure is broken into two consecutive layers of thickness, $d_1 = 0.225 \mu m$ i.e. two thirds of the silica sphere diameter and $d_2 = 0.075 \mu m$ i.e. one third of the silica sphere diameter for the glass/air layer and solid glass respectively. We had corrected for the interplannar spacing along <111> direction that is 0.8165 times the silica sphere's diameter. The refractive indices of these layers is calculated with the help of the loading equation [38]

$$(n_{eff})^2 = F(n_{01})^2 + (1-F)(n_{02})^2 \qquad (3.5.2.1.25)$$

where n_{01}, n_{02} are the refractive indices of the corresponding glass $n_{01} = 1.45$, and air $n_{02} = 1.0$, respectively. The filling factor F, for only the first layer of glass/air i.e. layer 1 is taken as, $F = 0.45$, based on the geometry of the close packing structure and width of the same layer is assumed to be half of the air/glass layer i.e. $d1 = 0.225/2 = 0.1125 \mu m$. For the rest of the structure, the filling factors for air/glass sub-layer (i.e. layer 1) and the glass layer (i.e. layer 2) are taken to be $F = 0.55$ and $F = 0.91$, respectively. These calculations of F is based on the amount of glass or silica present in each sub layer. A pure opal structure has $F = 0.74$, i.e. it contains 26% air voids.

After Si implantation and subsequent annealing, we observe the broadened reflection peak and slightly blue shifted as can be clearly seen in figure 3.9. Apart from this, we observe formation of two side bands around $\lambda = 500$ and 430 nm, and a shoulder at 650 nm. A one-dimensional model for this implanted structure is also simulated and is shown in figure 3.9. In this model, we assumed that the implantation of Si into opal has changed the refractive index of the opal structure. The index

sequence is 1.3, 1.42, 1.3, 1.42, 1.7, 1.95, 1.4, 1.42, 1.3, 1.42, 1.25, 1.42, 1.25, 1.42, ..., keeping the layer widths same as discussed before. We have assumed an asymmetric implantation profile due to the varying local slope of each silica sphere with respect to ion beam direction.

3.5.3   Nonlinear Experimentation

The nonlinear experimentation [39] on the ion implanted silica opal samples are conducted with the help of the Q-switched frequency doubled Nd:yttrium-aluminium-garnet (Nd:YAG) laser system. The laser emits 10 pulses every second with pulse duration of 10 nS at λ=532 nm. The experimental setup is shown in figure 3.11.

The Si implanted red opal sample is kept at the focal point of a lens with $f = 15cm$. The reflection and transmission for the nonimplanted and implanted sample was obtained as a function of latitude angle between surface normal and laser beam. The experiment is done at different i/p intensities by varying the neutral density filters in the path of the laser beam.

In figure 3.12, we show the transmission through the Si implanted sample as a function of latitude angle, θ, at two input light intensities falling on the sample for H-polarized light. The curves are normalized to the data obtained for nonimplanted opal samples. The actual transmission values were 20 to 40%. In figure 3.13, we represent the reflection data at two intensities. The reflection data includes all diffraction orders and is normalized as in the case of transmission to the reflection from the nonimplanted opal. The normalized reflection data oscillates as a function of the latitude angle θ,
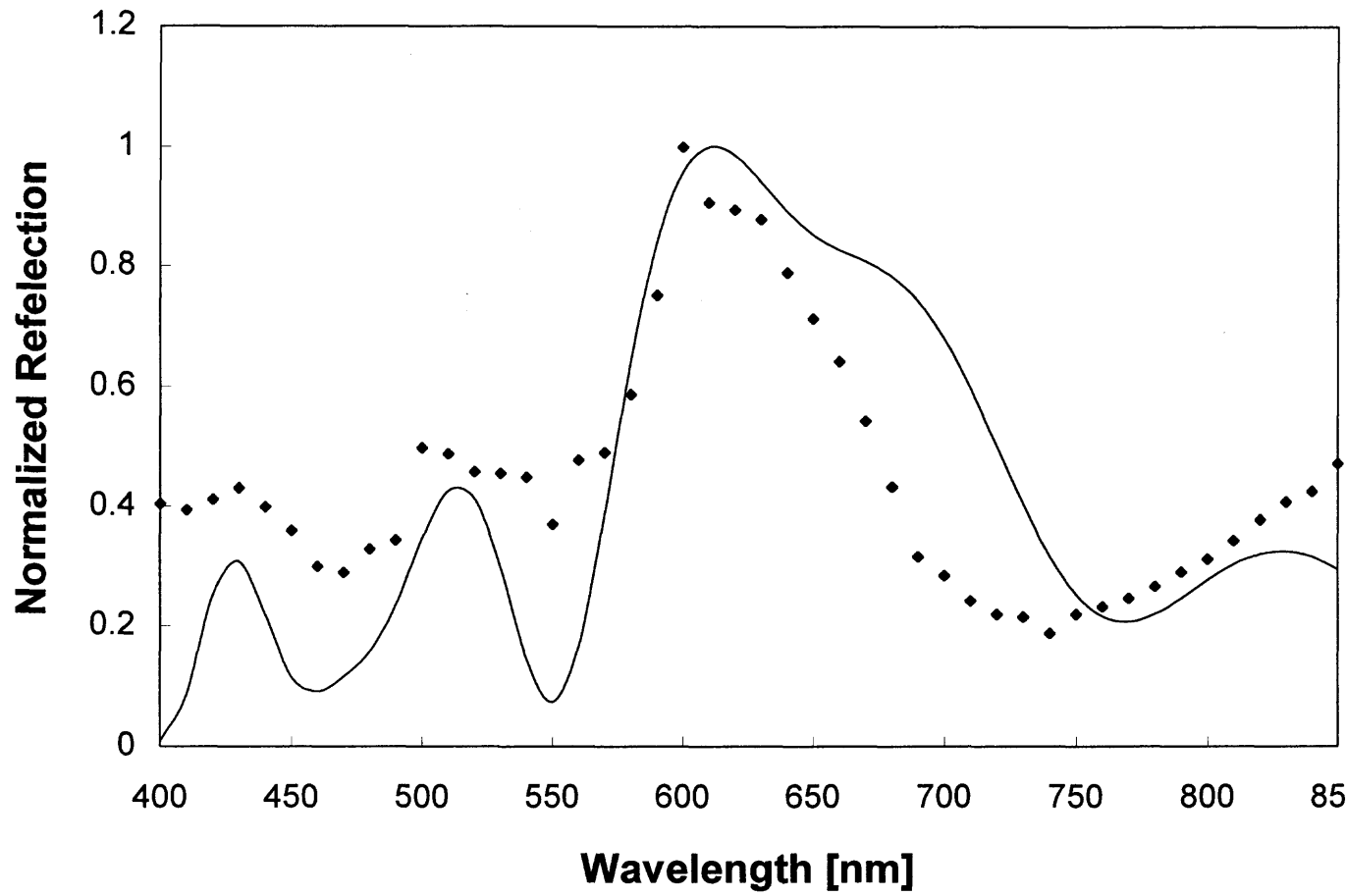
Fig. 3.10   One dimensional simulation of the reflection data of the silicon implanted red opal sample (The peak reflection is set to unity)
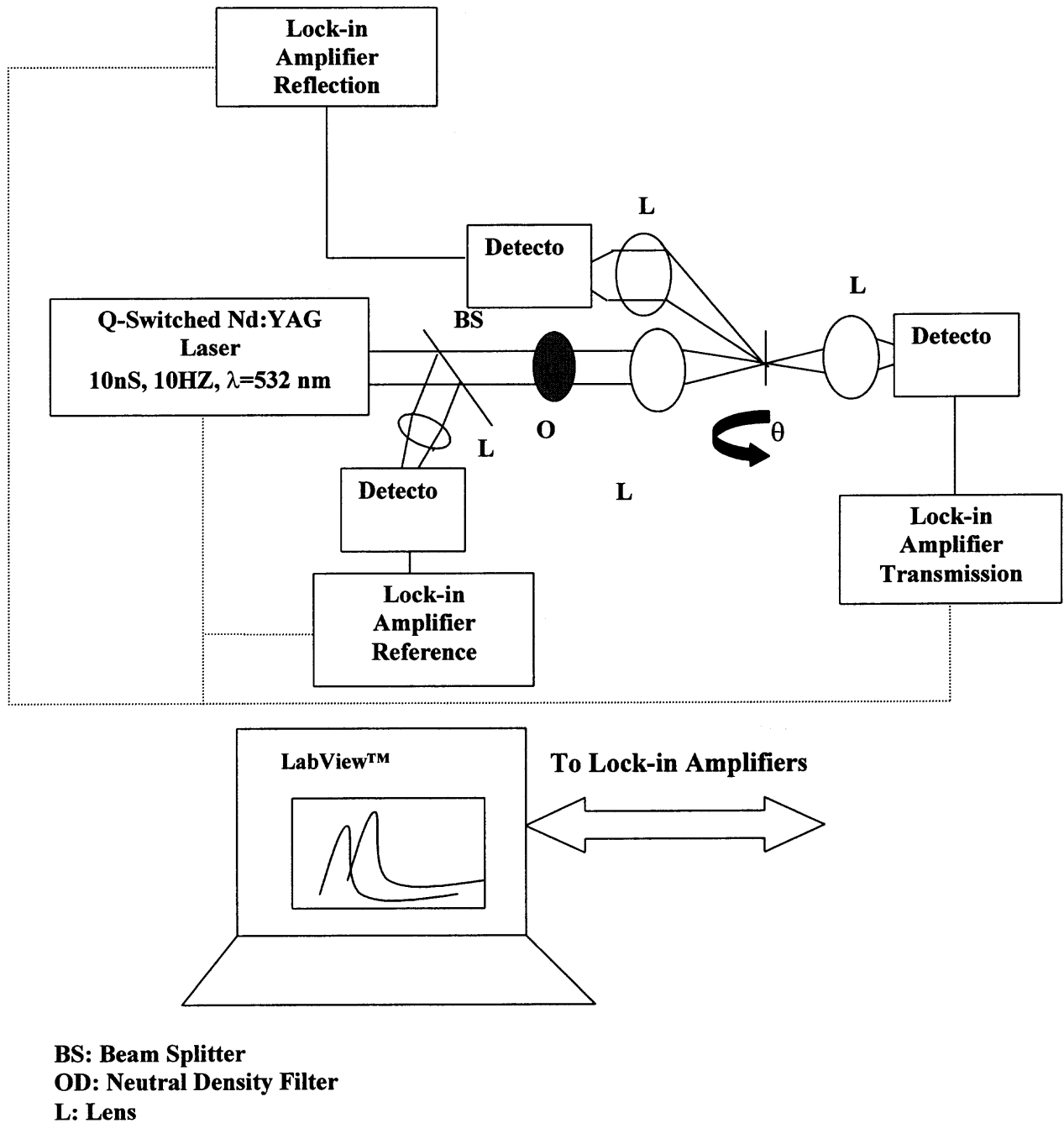
Fig. 3.11   Experimental setup for the nonlinear characterization of silicon implanted opal

indicating the effect of the difference between Bragg reflections from the implanted and nonimplanted opal layers in <111> crystallographic direction.

In figure 3.14, we present the normalized transmission of the Si implanted red opal sample as a function of light intensity at $\theta = 20^0$. One can clearly see the large change in the transmission as the i/p intensity is varied by only one order of magnitude. The intensity values on the order of 10^4W/cm^2 are of particular consideration as compared to 10^7W/cm^2 for the Si implanted in plane silica [40]. We checked the nonimplanted opal samples for this behavior, but they show a flat transmission response in the intensity range of 10^3-10^7W/cm^2.

A simplified model can be constructed to fit the normalized transmission data of the Si implanted red opal structure. The transmission through the sample T, in the <111> crystallographic direction and away from longitudinal resonance condition, is composed of the transmission through the implanted film, T_{Si-nc}, and the transmission through the nonimplanted portion of the opal, T_{opal}. Hence total transmission through the ion implanted sample may be written as

$$T_{sample} = T_{Si-nc} T_{opal} \qquad (3.5.3.1)$$

Hence normalized transmission of only the implanted film may be written as

$$T = T_{sample} / T_{opal} \qquad (3.5.3.2)$$

The implanted film is very thin (few monolayers of 300-nm size opal) and hence can be treated as a nonlinear phase grating. Therefore, overall normalized transmission in the far field can be written as
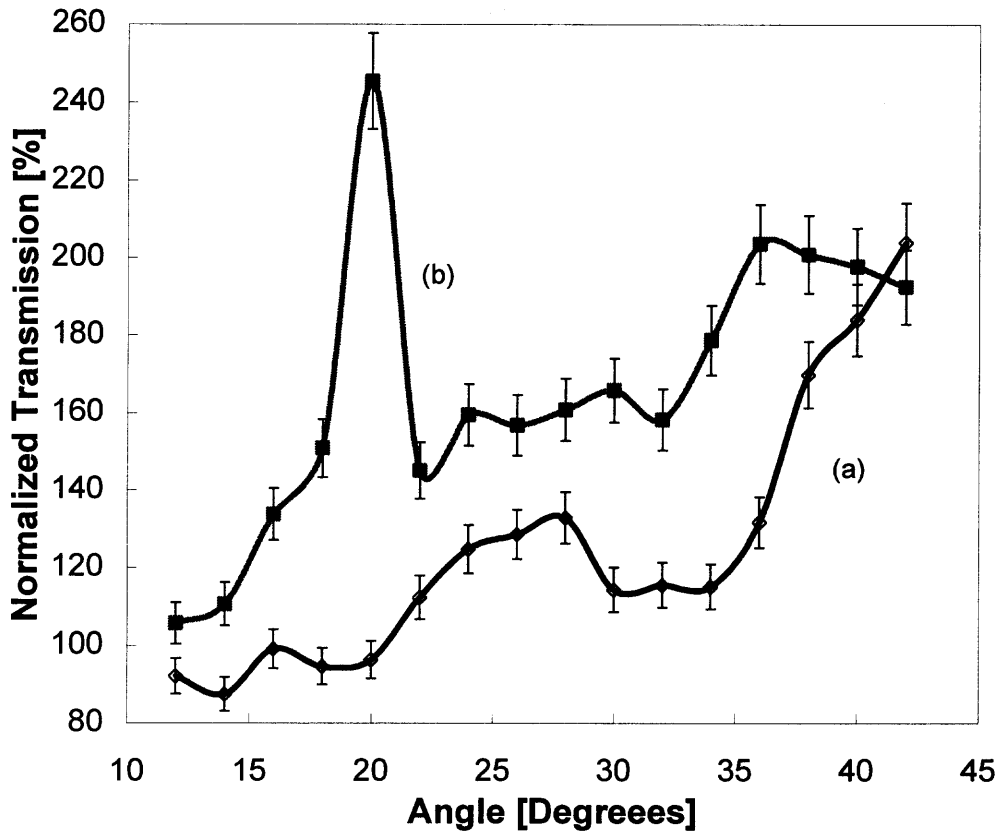
Fig. 3.12   Normalized transmission through a Si implanted opal sample as a function of latitude angle, θ at two intensities (a) $I = 1.49 X 10^3$ and (b) $I = 25 X 10^3 W / cm^2$ (Normalization is done with respect to non-implanted sample)
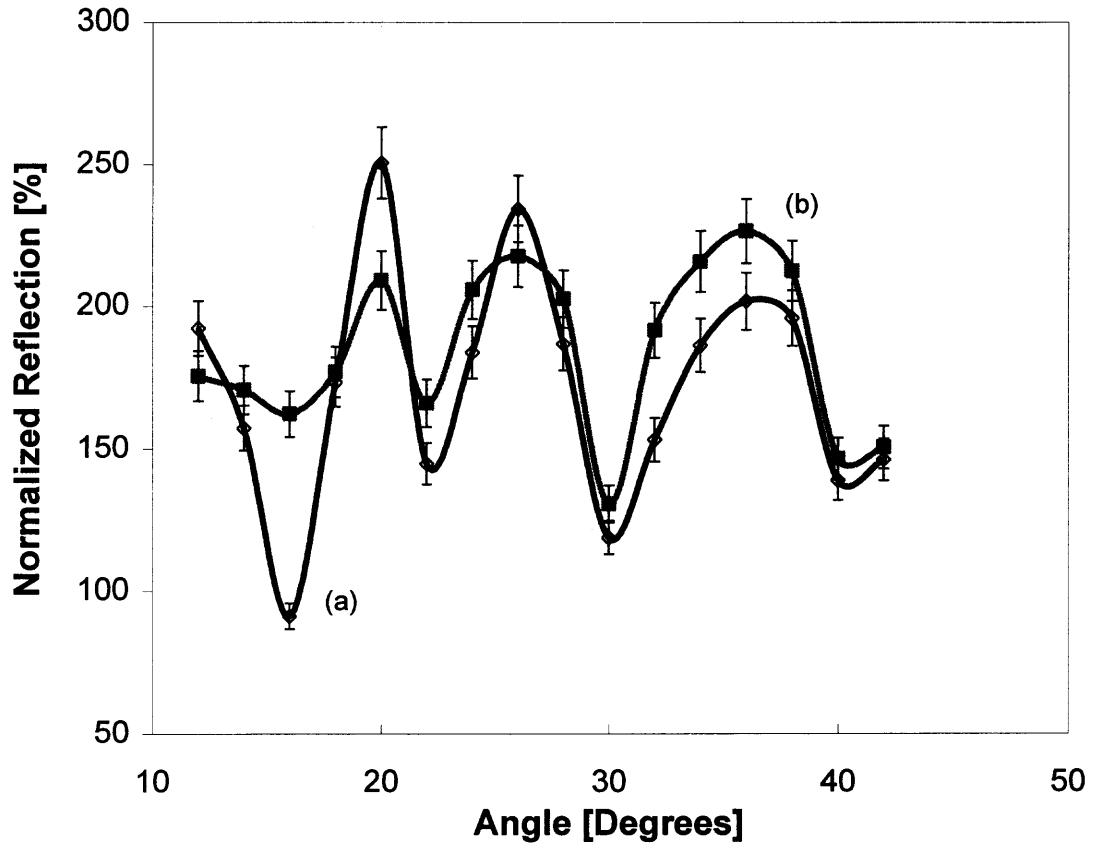
Fig. 3.13 Normalized reflection from a Si implanted opal sample as a function of the latitude angle, θ at two intensities (a) $I = 1.49 X 10^3$ and (b) $I = 25 X 10^3$ W/cm^2 (Normalization is done with respect to non-implanted sample)
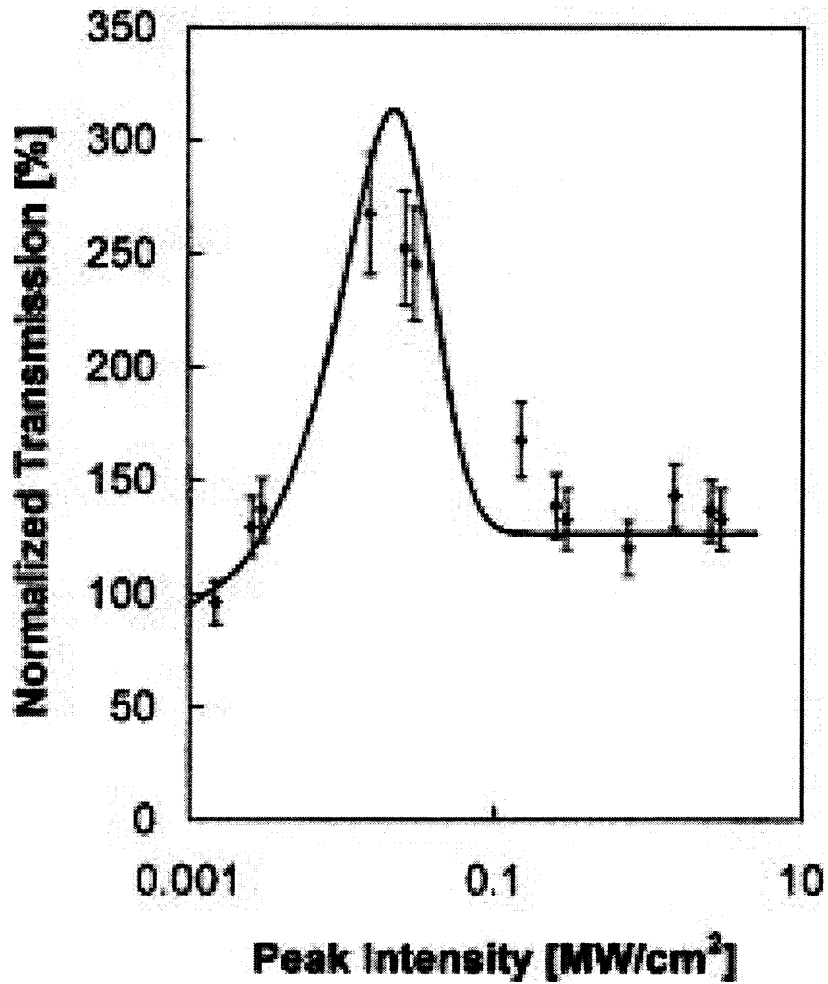
Fig. 3.14   Normalized transmission as a function of light intensity. The curve is normalized to the transmission obtained for a nonimplanted opal. The solid curve is a fit to the data based on equations 3.5.3 and 3.5.7

$$T \approx [AJ_0(m/2)]^2 \qquad (3.5.3.3)$$

Here, A, is the relative amplitude, J_0 is the Bessel function of the first kind and zeroth order, and m is the modulation index. In general, the modulation index m may be written as

$$m = k_0 n(I) L_{eff} \qquad (3.5.3.4)$$

where, k_0, is the propagation wave number in the vacuum, $n(I)$, is the intensity dependent effective refractive index of the grating at a given peak i/p intensity I, L_{eff} is the effective thickness of the implanted film which is given by

$$L_{eff} = L \cos \theta'' \qquad (3.5.3.5)$$

where θ'' is the angle of the optical beam inside the implanted film with respect to the normal to the sample surface. The modulation index of the implanted film is the unknown and is used as a fitting parameter in the form

$$m = 2n(I)\pi \qquad (3.5.3.6)$$

The calculation of the nonlinear refractive index change is based on the results for the Si implanted flat silica samples [37]. We assume that the electronic properties of the Si nanoclusters in opal do not substantially differ from those incorporated in flat samples. We approximate the saturation of the refractive index of the implanted samples as

$$n(I) = n_{eff} + n_{20} \tanh[-\gamma(I - I_t)] \qquad (3.5.3.7)$$

where n_{20} is the saturation coefficient. The nonlinear coefficient γ is fitted to the data and I_t also. Finally at a given angle, we plot equation (3.5.3) and (3.5.7) as a function of peak intensity I. The result of such a modeling procedure is shown in figure 3.11 with solid curve.

This fit to the experimental data is consistent with the modulation index that is described by equations 3.5.4 and 3.5.6. The assumptions made during the modeling procedure are: $n_{eff} = 1.91$, $n_{20} = 0.53$, with the resulting fit parameters: $\gamma = 3X10^{-5} cm^2 / W$ and $I_t = 5000W / cm^2$. A similar curve fit when employed for the Si ion implanted flat silica samples had resulted $\gamma = 8.4X10^{-9} cm^2 / W$ and $I_t = 6.5MW / cm^2$. Thus, we interpret the efficiency in the transmission results arising from the nonlinear effective phase grating with a large modulation index; $m(I) \approx 2.4\pi$; when the zeroth order maximizes and the first order of diffraction minimizes.

3.6 Discussion

After the Si implantation and subsequent annealing at 1100^0C, the opal film showed swelling, although the opaline structure beneath is intact as seen in the SEM picture (Fig 3.2) This film swelling is consistent with the average projected range of the Si implanted layers. One expects that above a certain implantation thresholdthe silica spheres will be damaged. From Fig. 3.3, we observe that the damage was pronounced for the first layer even though the peak concentration of the implanted Si lies approximately 600 nm below surface. Therefore, we expect the swollen region to occupy a width of $1.2 \mu m$ which is in good agreement with Fig. 3.3 .As shown through white light experiments, the refractive index of the swollen film is inhomogeneous and retained it's periodicity. Optical inspection of the top implanted layers before and after annealing revealed no visible change which implies that the matrix damage and the swelling is a result of only implantation process and is related to the implantation energy and dosage. The possibility of opal matrix melting during the implantation is small as the substrate

was air-cooled during implantation and the elevated temperature due to poor glass conductivity is estimated to be no more than 200^0C which is far less than melting temperature of glass. Recently the deformation of opal matrix by the 4MeV Xe ion beam implantation dose of 10^{14} cm^{-2} is reported [41]. We will discuss in later chapters, whereby the opaline matrix implanted by 2.7 MeV Er$^+$ [42] ion beam dose of 10^{14} cm^{-2} leaves the opaline structure intact.

The qualitative agreement between our one-domensional model and experimental data suggests that the refractive index distribution in the swollen layers of the implanted film retained some degree of periodicity. Despite its simplicity compared to some of the other models [43], the model accounted for the sideband formation. Nonlinear experiments also support the idea of periodic dispersion of silicon nano clusters followed the periodic structure of opaline template even after the collapse of top layers of opal matrix. The one-dimensional theoretical model for the opal matrix indicates that the distribution of ion-implanted region around the peak concentration is asymmetric. This is due to the fact that local surface normal of the opal sphere was not parallel to the ion beam direction and varies form point to point. The implantation range varies roughly as the cosine of the angle between the ion beam direction and the surface normal, which results in a shorter and asymmetric range profile. The reflection Bragg peak does not change when H-polarized incident light is used which re-emphasizes the fact that major contributions to the reflection data are from longitudinal Bragg planes. Transmission data on the other hand depends on the input polarization state and on the opal symmetry because of accumulated lateral scattering from various crystallographic planes.

For the nonlinear experiments, the normalization procedure [39] may be complicated by the fact that the in-plane symmetry is that of a hexagonal structure as seen in Fig. 3.2. Thus, one may argue against the validity of the normalization procedure on the basis that the azimuthal (rotations within plane) angle is unknown. We checked this point by measuring the transmission dependence of the nonimplanted sample and implanted sample as a function of latitude angle, θ, at various azimuthal angles, ϕ. Nonimplanted opal did not show any major change in normalized transmission profile, where as silicon implanted sample showed random oscillations within error margins.

The assessment of the angular dependence of the beam propagation within the opal matrix is based on the Figs. 3.4 and 3.5. If the process originated from a longitudinal Bragg condition along <111> crystallographic plane, then, $2n(I)d_1 \cos\theta'' = s\lambda$, with $s = 1,2,3,....$ and d_1, the interplanar spacing and θ'', the angle of transmission inside the implanted film. In this case, $\tan\theta'' \Delta\theta'' \approx \Delta\lambda/\lambda$. On the other hand, if there is a transverse confinement component, the Bragg condition reduces to $2n(I)d_2 \sin\theta'' = s\lambda$ and thus, $ctg\theta'' \Delta\theta'' \approx \Delta\lambda/\lambda$. Based on the white light reflection experiments, $\Delta\lambda/\lambda \approx 1/6$. Taking $\theta = 20^0$, we find from the Snell's law and by using $n_{eff}^{(0)} = 1.99$ and that $\theta'' \approx 10^0$. Based on the later equation we estimate $\Delta\theta \approx 2^0$ which is in excellent agreement with the data presented in Fig. 3.5. We hence conclude that the experimental values imply a transverse confinement process.

Thermal effects associated with the silicon nanoparticles usually posses negative γ values; while here we calculate positive values. Also, thermal effects which are related to mechanical displacements or refractive index changes in the opal structure, would

result in curve's oscillation when plotted as a function as a function of the light intensity. This is due to the fact that they involve only the implanted film and not the nonimplanted layers. If we were to assume that the Si implanted region is made of a homogeneous implanted material, then we may treat it as a dielectric slab. Based on the white light experiments, we concluded that we operate away from any longitudinal Bragg reflection. Therefore we are able to calculate the nonlinear index change. We calculate $\Delta n = 0.55$ per decade of intensity change around $I \approx 10^4 W / cm^2$, compare to $\Delta n = 0.53$ at $I \approx 15 MW / cm^2$ for Si implanted in smooth silica matrix.[40]. Since the thickness of the silicon implanted flat and opaline films are comparable, we arrive at the conclusion that the opal provided additional confining environment, which enabled the nonlinear properties of silicon nanoclusters. For the same reasons outlined above, we propose that the enhanced nonlinear effects are the result of a transverse beam confinement in the opaline matrix.

CHAPTER 4

Ge IMPLANTED OPAL MATRIX

4.1   Introduction

In the current chapter we probe into the germanium implanted opal structure for its various linear and nonlinear optical properties. Quite interestingly, both the Si and Ge group IV semiconducting elements from the periodic table although widely used in semiconductor industry, are not being used extensively in the optoelectronic industry owing to their indirect bandgap [44].

This chapter is organized into the sections on sample preparation, scanning electron micrograph pictures portraying the morphological details of the physical structure of the sample followed by few linear and nonlinear optical experimentation and finally winding with discussions.

4.2   Preparation of Photonic Crystal

We follow the TEOS procedure outlined in chapter 3, section 3.3.1 whereby the sub-micron sized photonic crystal is prepared by the hydrolysis of TEOS (tetraethoxysilane) in a mixture of ammonium hydroxide, for the preparation of a photonic crystal with the periodicity in the visible wavelength. FCC structure of the silica spheres is grown on the glass. As discussed earlier, owing to Bragg's law, opaline matrix scatters red, green and blue colors in reflection for the feature size of 300, 245 and 200 nm respectively.

4.3   Ion Implantation of Ge In Opaline Matrix

The opaline matrices prepared above are ion implanted by Ge ions. The ion implantation was done at 150 KeV with fluence levels ranging between 2 x 10^{14} to 2 x 10^{15} cm^{-2}. The corresponding germanium peak concentration was estimated to be 3 x 10^{20} to 3 x 10^{21} cm^{-3} respectively. At the above said energy, the range of implantation is 925^0A with a straggle of 266^0A i.e. occupying only the first monolayer of the silica spheres.

The above Ge ion implanted opal samples are further annealed at temperature of 1100^0C in flowing Ar. Subsequently the Ge precipitates into nano-size crystallites within the nano-size opal matrix, to create the nano within nano structure.

4.4   Morphology of The Ge Implanted Opal

As in the case of Er implanted opal structure, we found that the implantation dosage of Ge at an energy of 150 KeV has left the opal matrix undamaged which is further concluded with the linear white light experiments. We present the SEM picture of the Ge implanted red opal matrix after annealing in Fig. 4.1.

4.5   Linear Experiments

Linear white light experiments [45] were performed on the Ge implanted red opal matrix with the help of the experimental arrangement discussed in chapter 3, section 3.4.2. As concluded by the SEM photographs in previous subsection, we indeed observed clear Bragg peaks in reflection for the Ge implanted red opal structure. The normalized reflection with respect to input intensity from the Ge implanted red opal matrix is shown in Fig. 4.2. This again confirms conclusively that the opal matrix was not damaged by
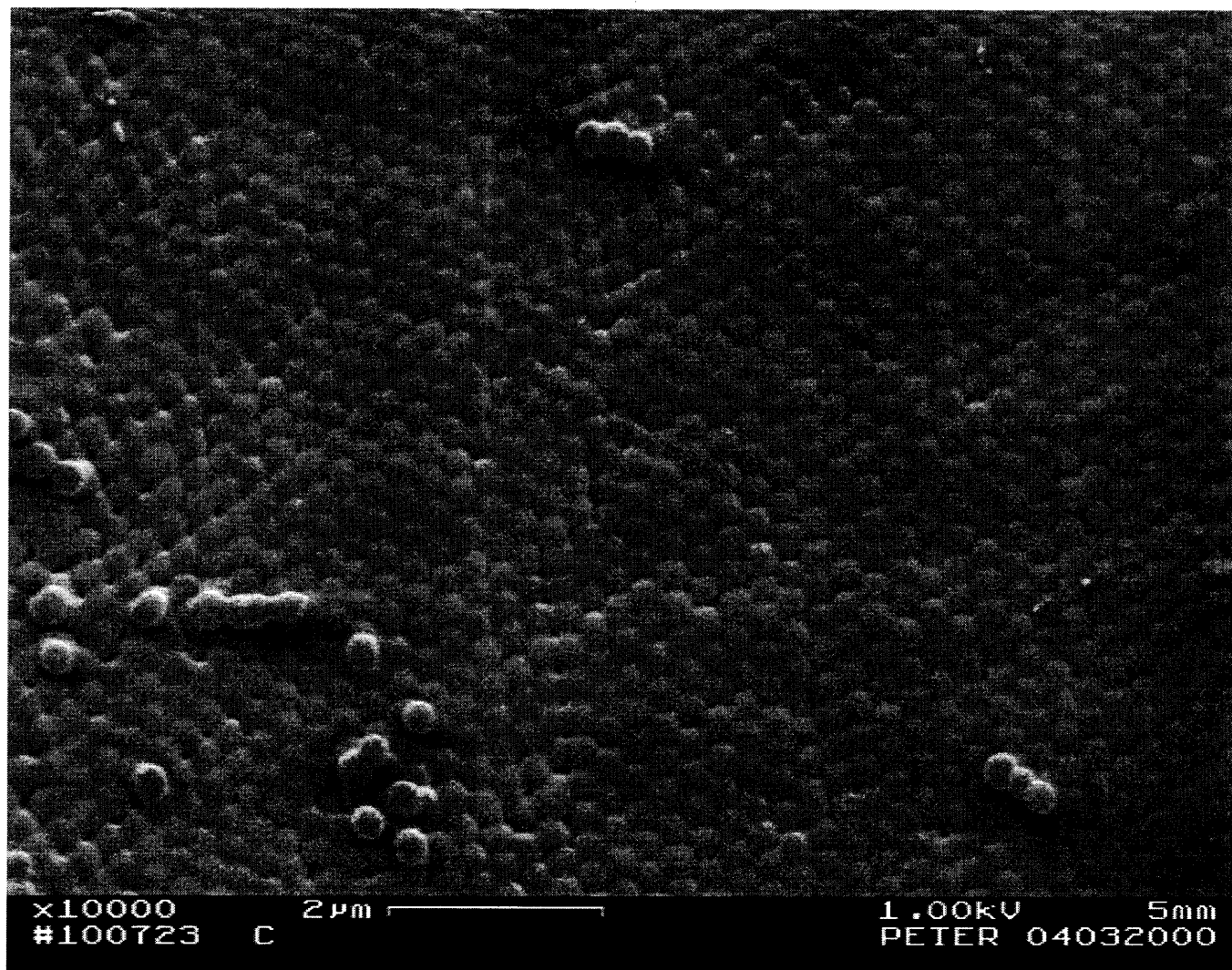
Fig. 4.1   SEM picture of high concentration, Ge-implanted, ordered array of
300-nm silica spheres after annealing at 1100 °C.
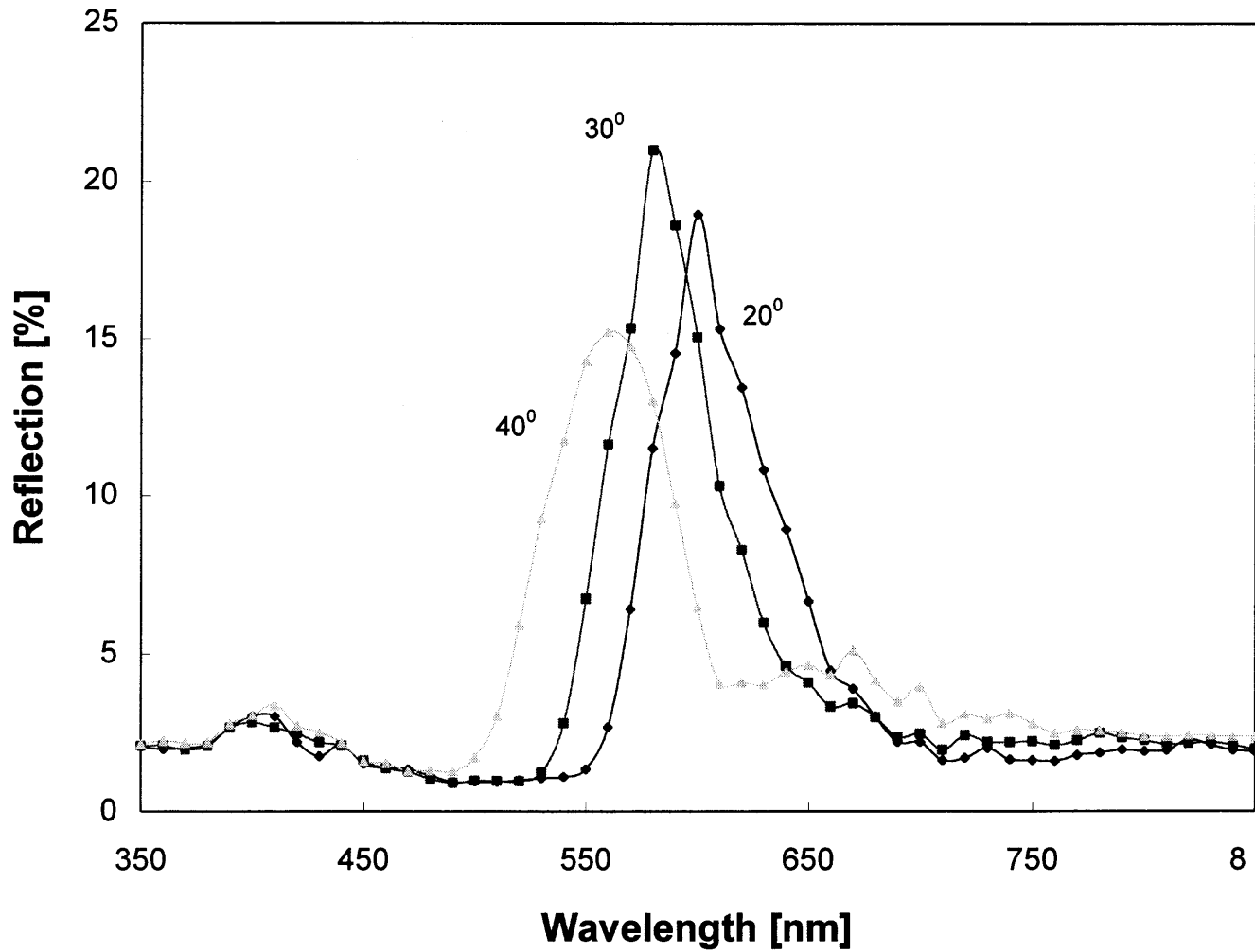
Fig. 4.2   Reflection from the Ge implanted opal as a function of incident wavelength and angle of incidence (Normalization is done with respect to input intensity)

the Ge implantation into it at the dose level described in section 4.2.2.

In Fig. 4.3 we present the transmission (normalized to input intensity) through the 300 nm size opal spheres in FCC lattice implanted by Ge ions. As seen the transmission exhibited two main features: one transmission dip centered at $\lambda = 550$ nm and other dip around $\lambda = 400$ nm. The first dip at 550 nm is attributed to complement of the enhanced reflection of <111> (across the opal sample) crystallographic plane of opal matrix. The other dip towards $\lambda = 400$ nm, is attributed to mid-Brillouin zone, direct transition within Ge nanoclusters. This transition is found to be independent of the fluence used during ion implantation process. Since the final Ge concentration and hence the final nanocluster size for a given annealing temperature depends on the ion fluence, one may conclude that this transition is cluster size independent. Fitting this transmission data for both the samples near the direct transition with the equation

$$-\ln T \propto (E - E_g)^{1/2} \tag{4.1}$$

where, T is the transmission through the sample, E is the photon energy and E_g is the bandgap energy of the nanocluster, we found $E_g = 2.26$ eV ($\lambda = 549$ nm) which is in good agreement with the size dependent, direct transition found for germanium colloids [46]. The curve fitting is done using KaleidaGraph software and by writing a subroutine for the equation 4.1.
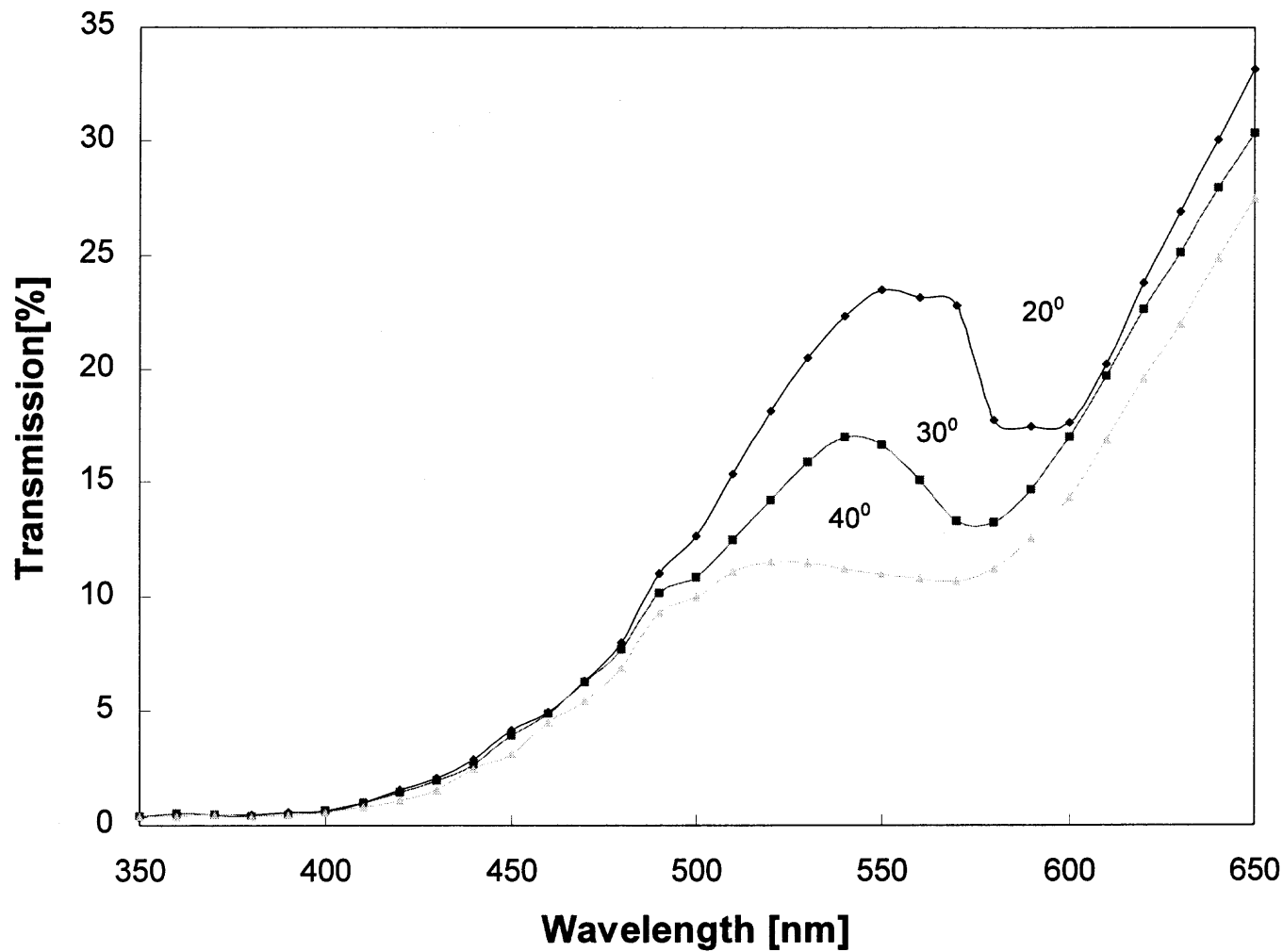
Fig. 4.3 Transmission through a high-concentration, Ge-implanted 300 nm opaline sample as a function of incident wavelength and various incident angles (Normalization is done with respect to input intensity)

4.6 Nonlinear Experiments

The nonlinear transmission experiments [45] were performed on the germanium implanted red opal matrix using the Q-switched Nd:YAG frequency doubled laser emitting 10 Hz pulses each of duration 10 nS at $\lambda = 532$ nm. The experimental setup used for nonlinear characterization of the sample is described in detail in chapter 3 under the section 3.5.

As in the case of earlier samples of silicon and erbium doped opal structures, we found the nonlinear transmission through the implanted samples peaking at angles of 22^0 and 38^0 for the high and low dose Ge samples. The transmission normalized tio input intensity through the high dose, Ge implanted opal sample as a function of different angle of incidence at three different intensities is shown in fig.4.4, while the transmission at angle of incidence of $\theta = 22^0$ for various input intensities is plotted in fig. 4.5.

4.7 Discussion

In this chapter, we describe the germanium implanted photonic crystal with feature size in the visible wavelength range, namely silica opal. The samples were fabricated by ion implanting the opal at different implantation dose at 150 KeV energy.

From the SEM pictures taken of the Ge implanted opal structure, we observed that none of the opal layers were destroyed by the germanium implantation dose unlike silicon implanted opal matrix discussed in chapter 3.
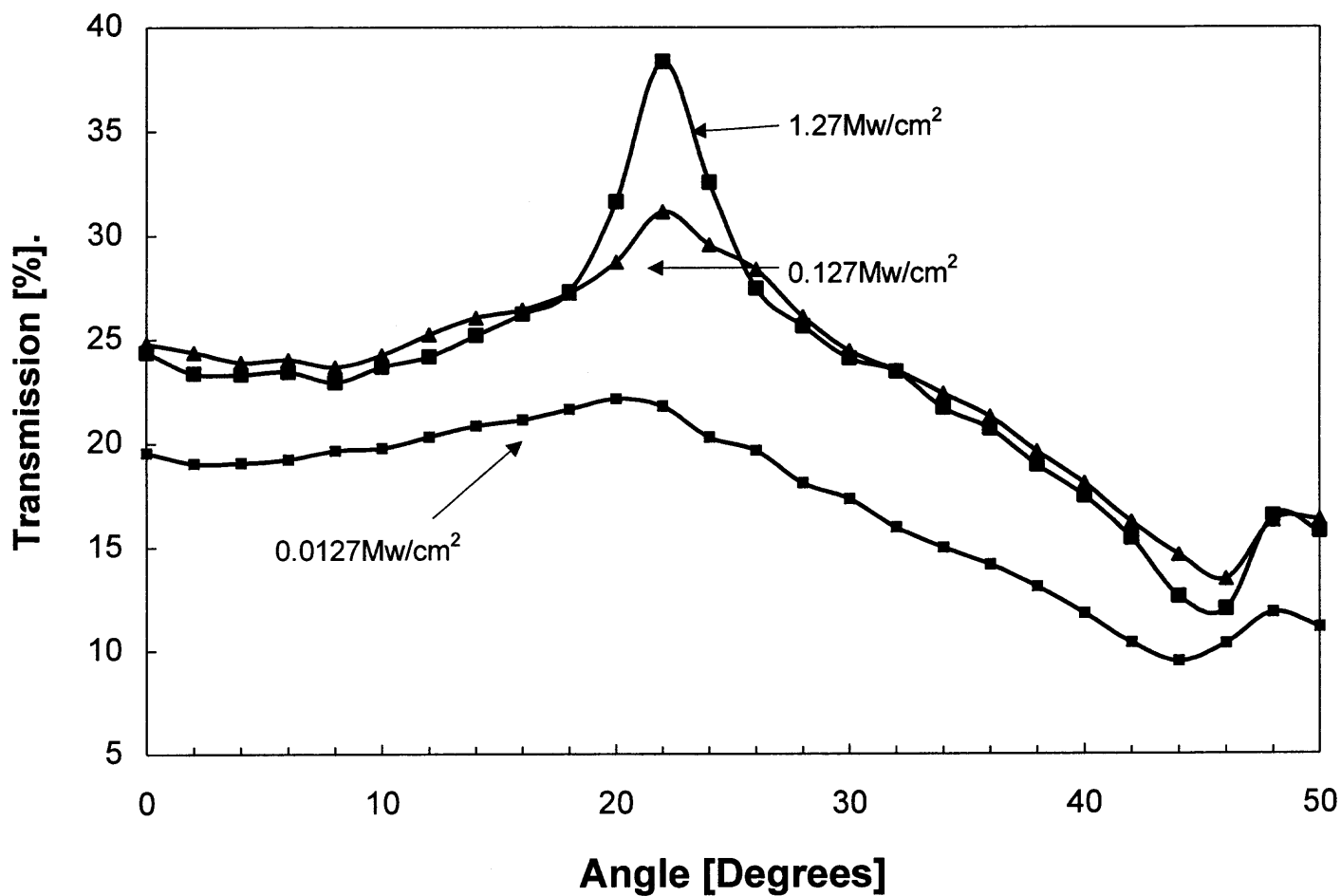
Fig. 4.4   Normalized transmission as a function of incident angle for high concentration sample of Ge implanted opal (Normalization is done with respect to input intensity)
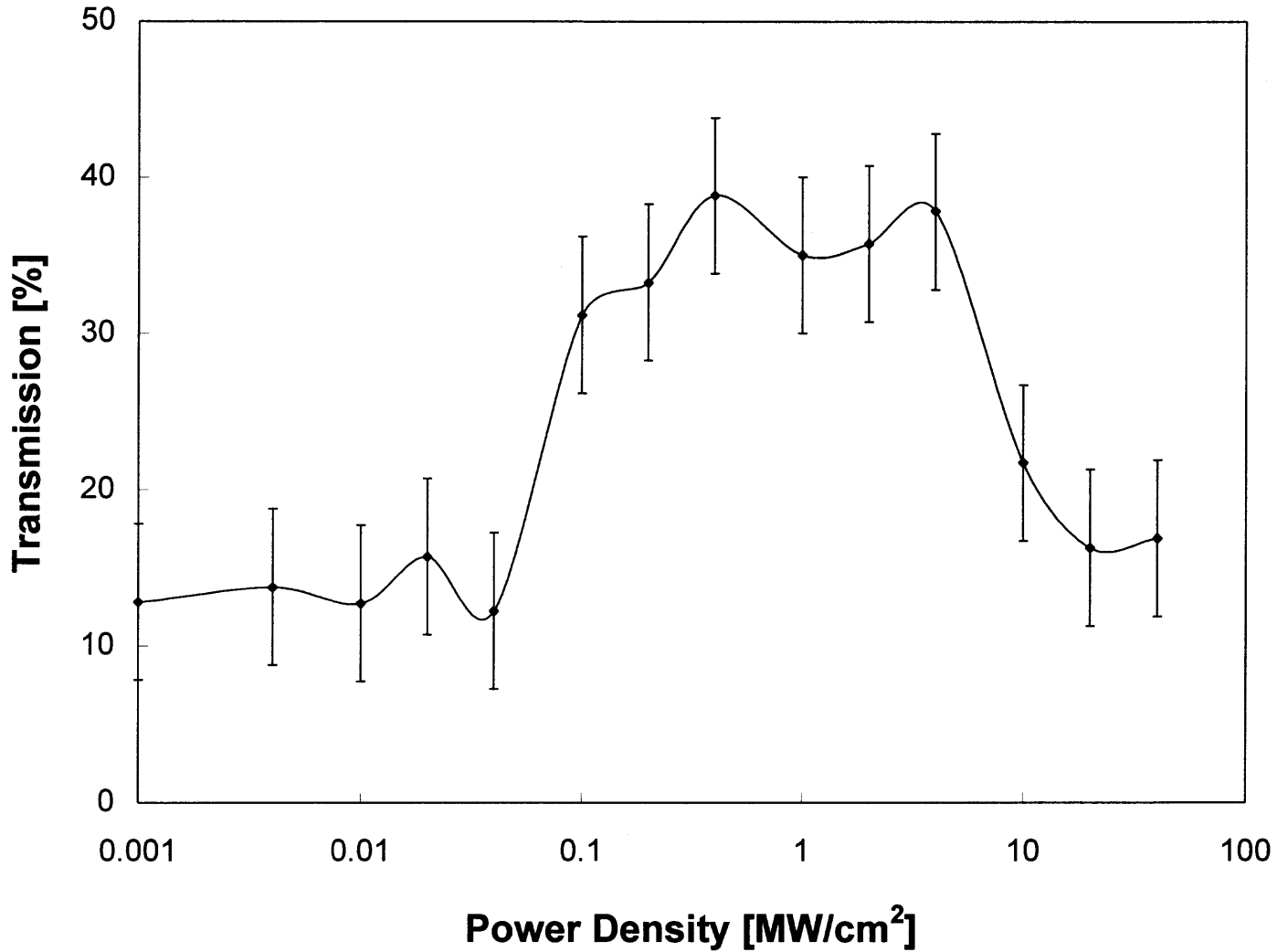
Fig. 4.5 Transmission as a function of light intensity at the angle of incidence θ=22° for the high concentration Ge sample (Normalization is done with respect to input intensity)
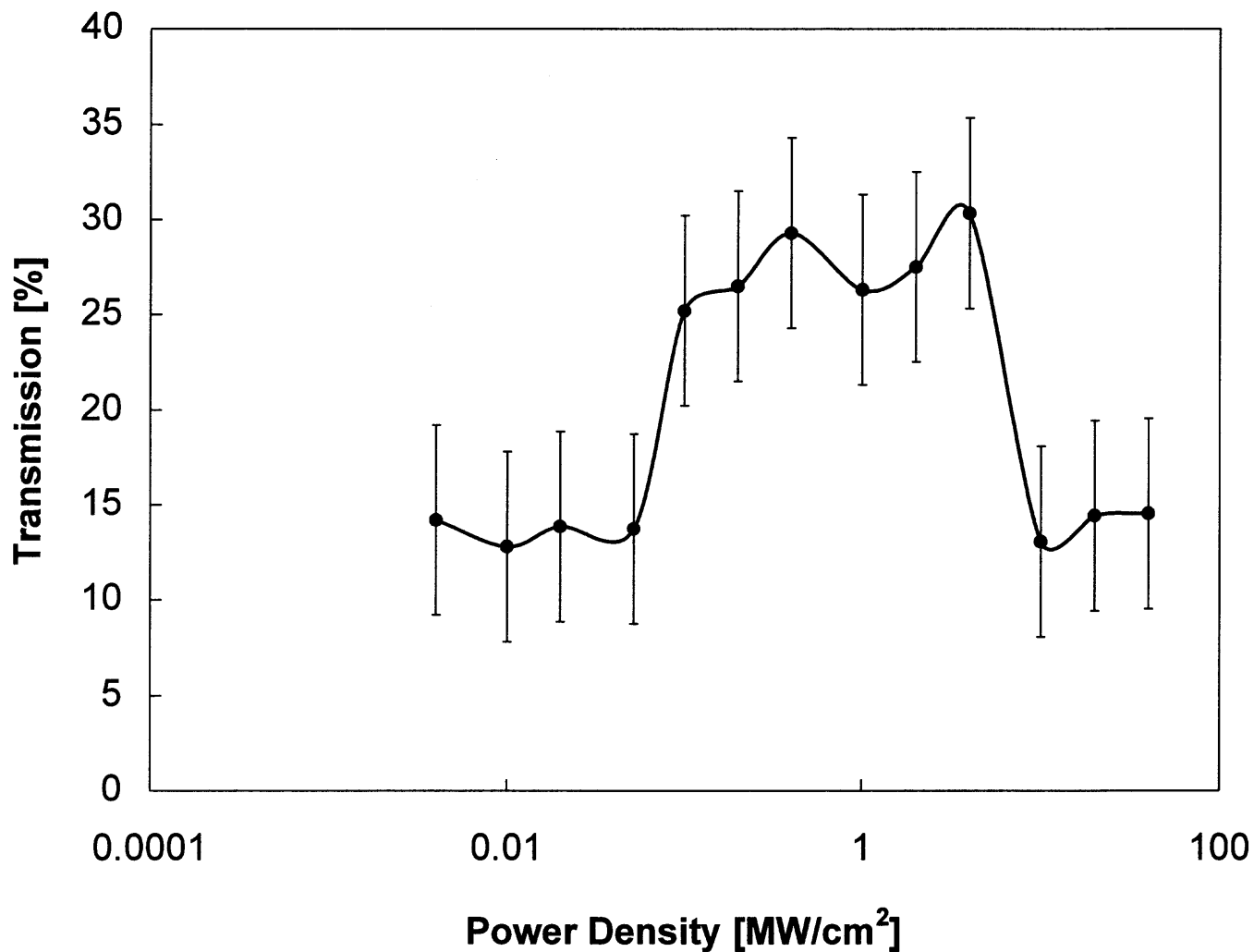
Fig. 4.6   Transmission as a function of light intensity at the angle of incidence

θ=38° for the low concentration Ge sample (Normalization is done with

respect to input intensity)

Linear white light experiments performed on the germanium implanted opal structure which displayed the Bragg peaks in reflection and corresponding decrease in the transmission through the sample. This is one of the typical characteristics of the photonic crystals. These experiments also support the conclusion of survival of the three dimensional periodic opal matrix after the germanium implantation. From the white light transmission results, we also verified the size-independent direct transition for the Ge colloids occurring at $\lambda = 549\,nm$.

Photoluminescence experiments were performed on the germanium implanted opal samples, but they failed to show any signal in the range of 600-850 nm.

The nonlinear experiments were done on the samples at $\lambda = 532\,nm$. As in the earlier samples of silicon implanted opal and erbium implanted opal, we found the nonlinear transmission of the germanium implanted opal samples peaks at different angles of incidence namely $\theta = 22^0$ and $\theta = 38^0$ for high and low implantation dose samples.

CHAPTER 5

ERBIUM IMPLANTED SILICA OPAL

5.1   Introduction

Over the past decade the fiber optic communications has been revolutionized by the advent of erbium doped fiber amplifier, which boosts the maximum length and the transmission capacity of the optical communication link. [47].

In this chapter, we will briefly review the procedure to grow such a Er implanted silica opal. We present different linear properties obtained from the white light experiments along with photoluminescence results on the Er implanted opal structure. We conclude the chapter after presenting different nonlinear results.

5.2   Preparation of Silica Opal-A Photonic Crystal

The TEOS [31], [32] method outlined in the third chapter in 3.3.1 is followed to fabricate opaline matrix with different periodicities in visible wavelengths. Opal samples with silica sphere diameter 200, 245, 275, 300 nm scattered blue, green, orange, red colors in reflection.

5.3   Ion Implantation of Er

The opaline matrix was ion implanted [33] by erbium ions to a dose of $10^{14} \, cm^{-2}$, aimed to reach the fifth layer of the FCC structure. For example, aiming at an implantation depth of 750 nm with a straggle of 90 nm for the 300 nm size opal matrix.

The implantation was done with an energy of 2.7 MeV. The peak Er concentration was estimated to be 1.8 x 10^{19} cm^{-3}. The ion implantor used for the sample preparation is of National Electrostatics Corporation's (5SDH-4) employing tandem Linear Accelerator. The ion source is Middleton type employing cesium sputtering source.

The implantation process was followed by one hour of annealing in flowing Ar at a temperature of 850 ^{0}C [48]. A color change made the implanted region visible after annealing, for example the implanted region of the red opal was seen as green, the orange sample turned bluish green, the green sample turned red, and the blue sample turned yellow. As observed in nonimplanted opal, complementary colors are seen in transmission for erbium implanted opal structures.

5.4   Morphological Details of Er Implanted Sample

We took the SEM pictures [34] of the implanted orange opal samples shown in Fig 5.1. As clearly seen in the SEM picture none of the opal layer was damaged or destroyed by the implantation process, unlike Si [39]or Xe [41] implanted samples. One can also see the uniformity of the opal size across the sample.

5.5   Linear White Light Experiments

Linear white light reflection and transmission experiments on the erbium implanted and nonimplanted opal samples were performed. The experimental configuration used for the linear characterization of the erbium implanted opal is the same as used for Si implanted opaline structure and drawn in Fig. 3.4 in section 3.4.2.
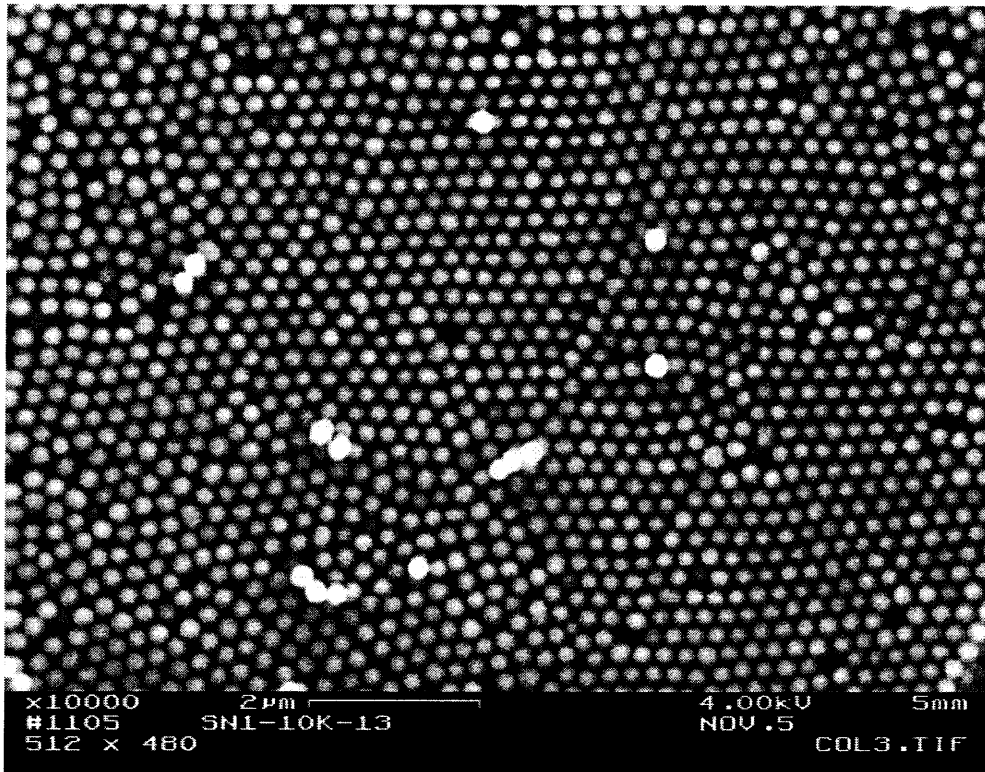
Fig. 5.1 Scanning electron micrograph picture of the Er implanted orange opal (i.e. silica sphere size = 275 nm).

In Fig 5.2 we show the linear reflection characteristics of the erbium implanted regions of a red sample [42] for two latitude angles of incidence (reflection is normalized to input intensity). The characteristic Bragg reflection pattern observed in these curves reconfirms the conclusion of non damaged opaline structure drawn from the SEM picture of the Er implanted opal structure. It also confirms the presence of a periodic opaline structure in crystallographic <111> direction perpendicular to the sample surface. The blue shift of the Er implanted opal structure with respect to the nonimplanted structure signifies the relative refractive index change in two regions. Although this change takes place only in the buried and implanted monolayer, it can be equivalently represented by a grating with effective refractive index $n_{eff} = 1.22$, (as compared to $n_{eff} = 1.35$ for nonimplanted opaline matrix) which is responsible for such a spectral shift.

5.6   Nonlinear Experiments

Nonlinear optical experiments [42] were conducted on the Er doped opal samples. The experimental configuration is drawn in Fig 3.5. The sample is placed at the focal point of a lens with $f = 15cm$. A $100\,\mu m$ focussed beam from a Q-switched Nd:YAG laser (Repetition rate = 10 Hz, Pulse duration =10 nS, $\lambda = 532nm$) was impinging on the sample. The transmission and reflection from the Er implanted and nonimplanted regions of the sample were measured as a function of latitude angle between the sample normal and laser beam.   The output from the photodetectors is collected using the lock-in amplifiers (Stanford Research SR510). We have used the averaging algorithm in the
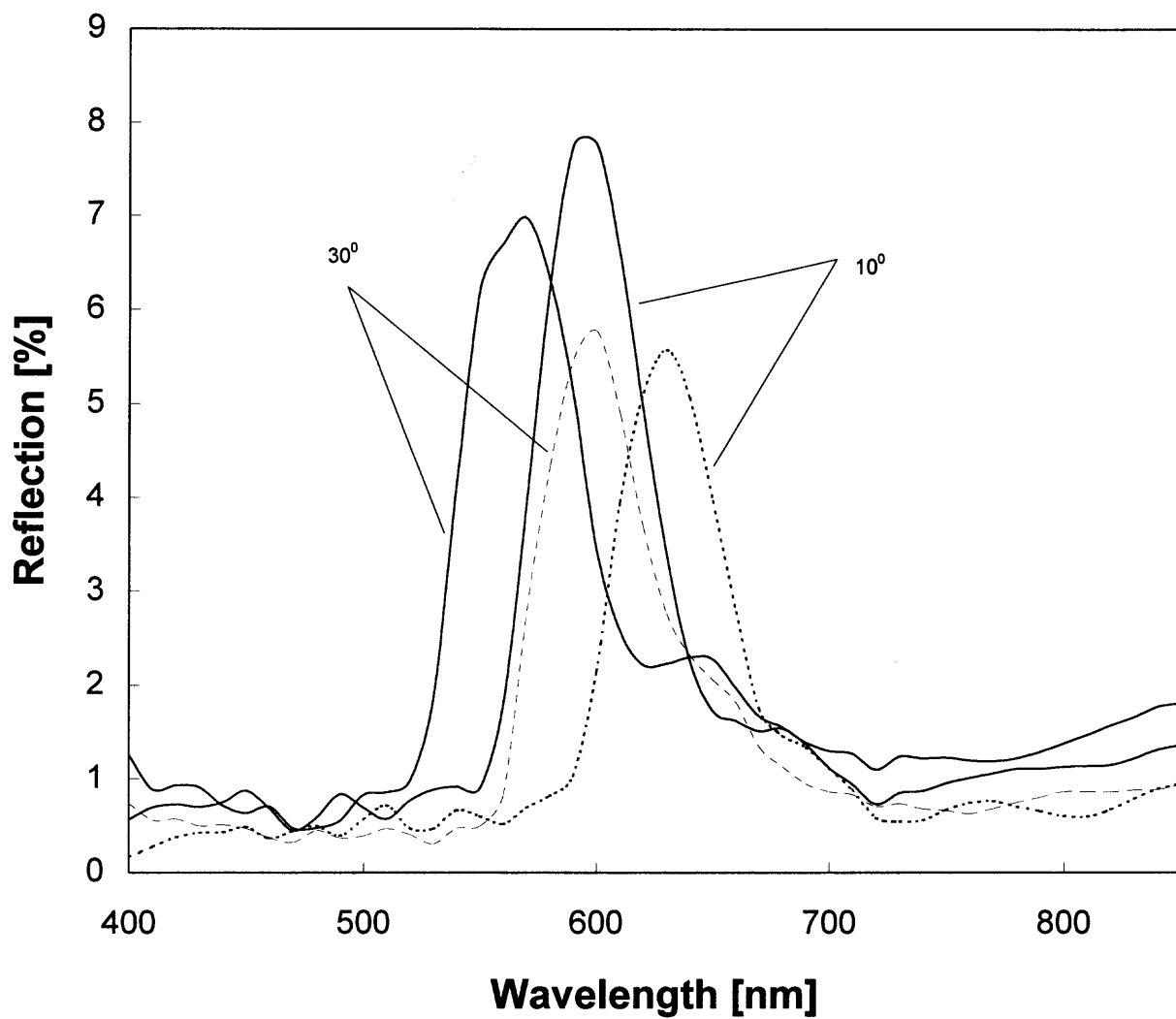
Fig. 5.2   Reflection from a 'red' (300 nm size spheres) Er implanted (solid curve) and non-implanted (dash curve) opal with E-polarized light (Normalization is done with reference to input intensity)

LabView™ to take the readings with laser power fluctuations less than 5-10% of it's nominal value.

The normalized transmission of the Er implanted opal with respect to the nonimplanted opal substrate is plotted for both the i/p polarizations in Fig 5.6 and 5.7. The polarization of the incident beam is varied by inserting the polarizer in the beam path. Figures 5.8 and 5.9 show the normalized transmission as a function of peak i/p intensity at a latitude angle $\theta = 50^{0}$. Based on the discussion in the earlier chapter on Si implanted opal structure and the Fig. 5.2, we note that such a normalization procedure helps to eliminate the effects of scattering from the opaline matrix in crystallographic <111> direction normal to opal surface.

5.7   Discussion

In this chapter, we probed the erbium implanted opal structures with respect to different linear and nonlinear optical properties.

From the SEM pictures, we clearly observe that none of the opaline layers were destroyed by the implantation dosage of Er, contrasting with the opal ion implanted with silicon as discussed in previous chapter.

The white light reflection experiments on the Er implanted and nonimplanted opal samples show distinct Bragg peaks, which themselves confirm the presence of periodic opal layers seen in SEM pictures. The blue shift of the reflection for the implanted layers shows the effect of the Er implantation on the refractive index profile of the combined i.e. opal and erbium implanted monolayer, structure.
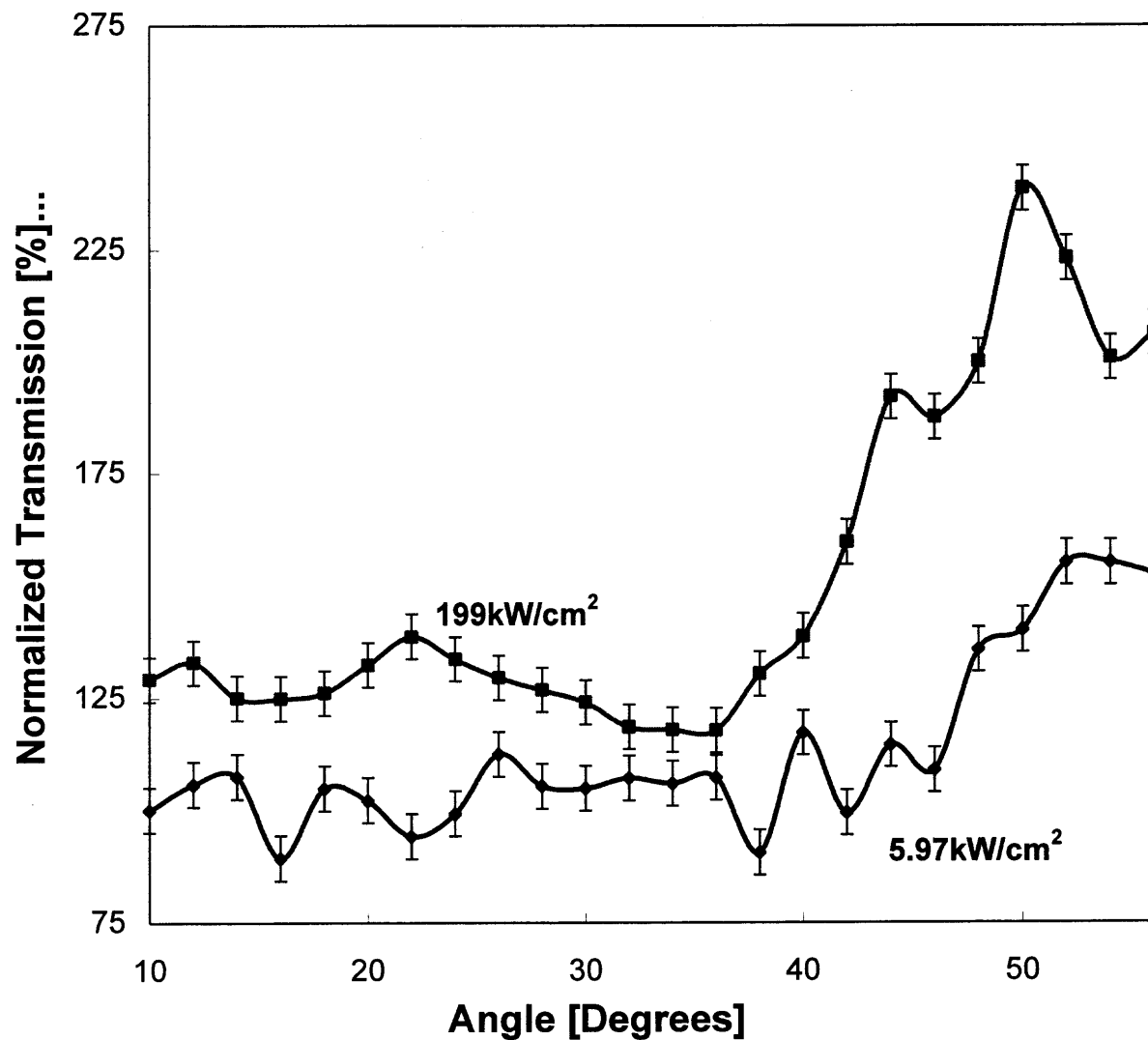
Fig. 5.3   Normalized transmission through the Er implanted red opal as a function of latitude angle for the perpandicular (E) polarization.(Normalization is done with reference to non implanted sample)
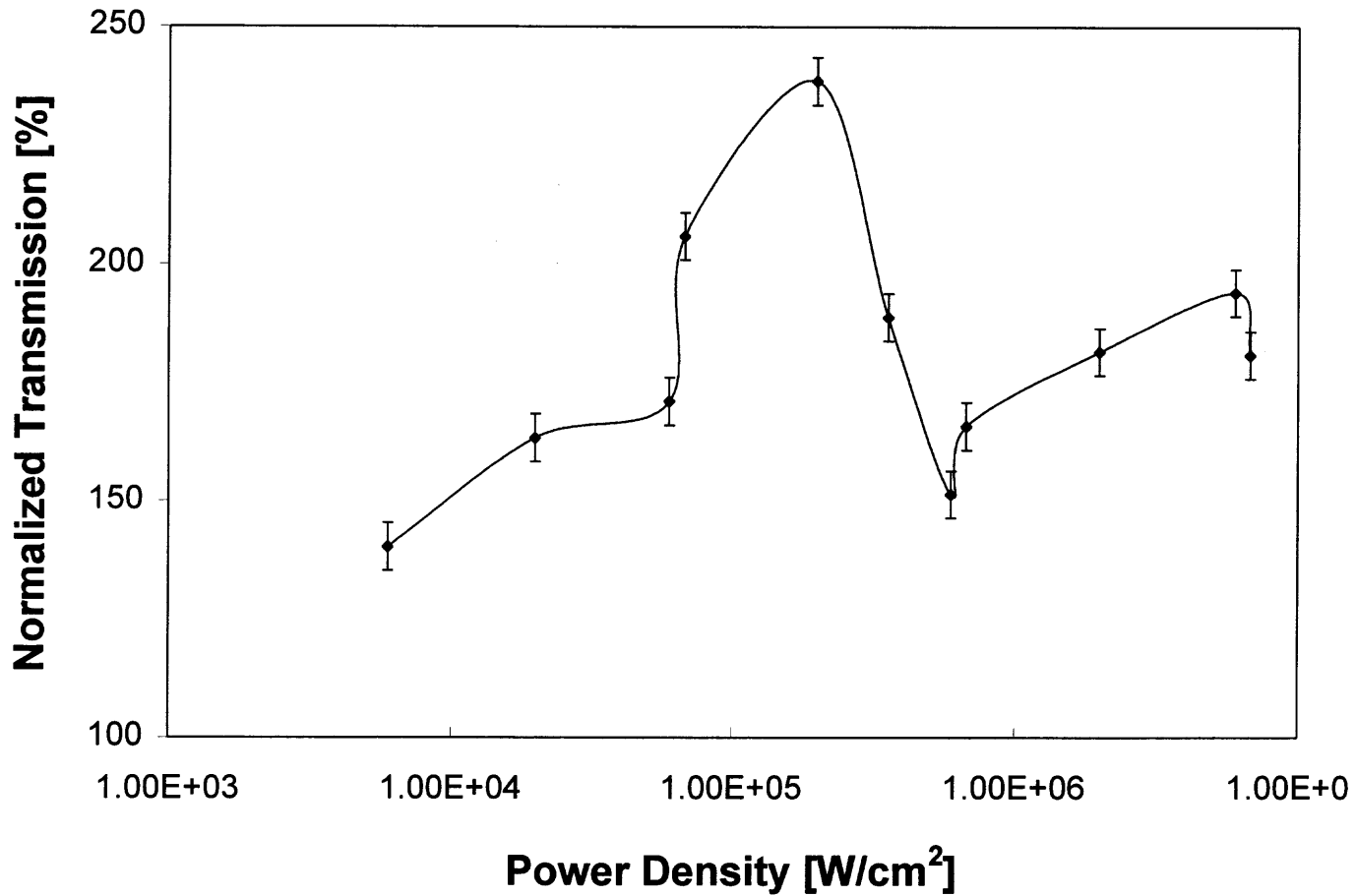
Fig. 5.4 Normalized transmission of the Er implanted red opal as a function of input light (E-polarization) intensity at latitude angle of $\theta = 50^0$ (Normalization is done with reference to non implanted sample)
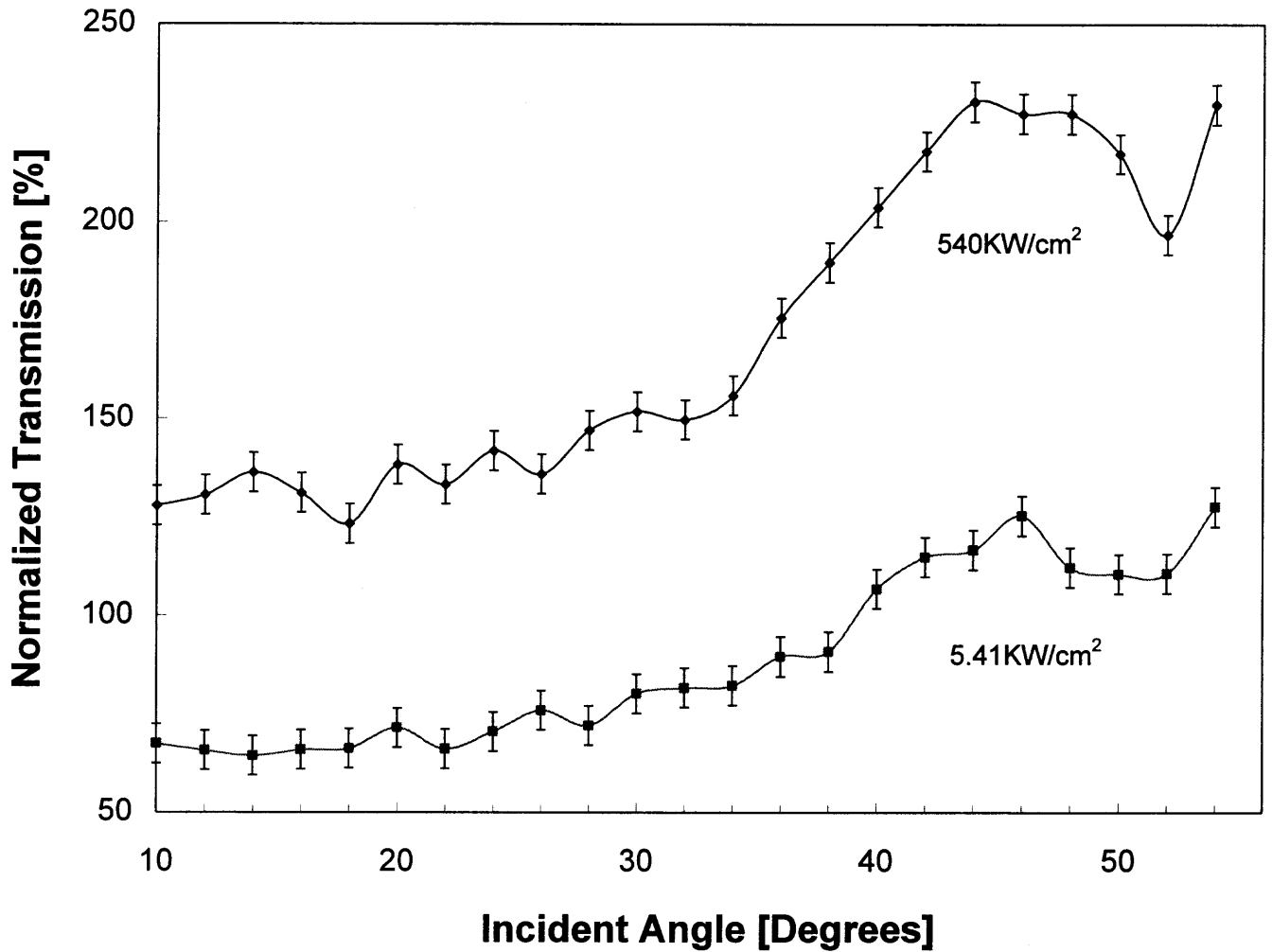
Fig. 5.5   Normalized transmission through the Er implanted red opal as a function of latitude angle for the parallel (H) polarization. (Normalization is done with reference to non implanted sample)
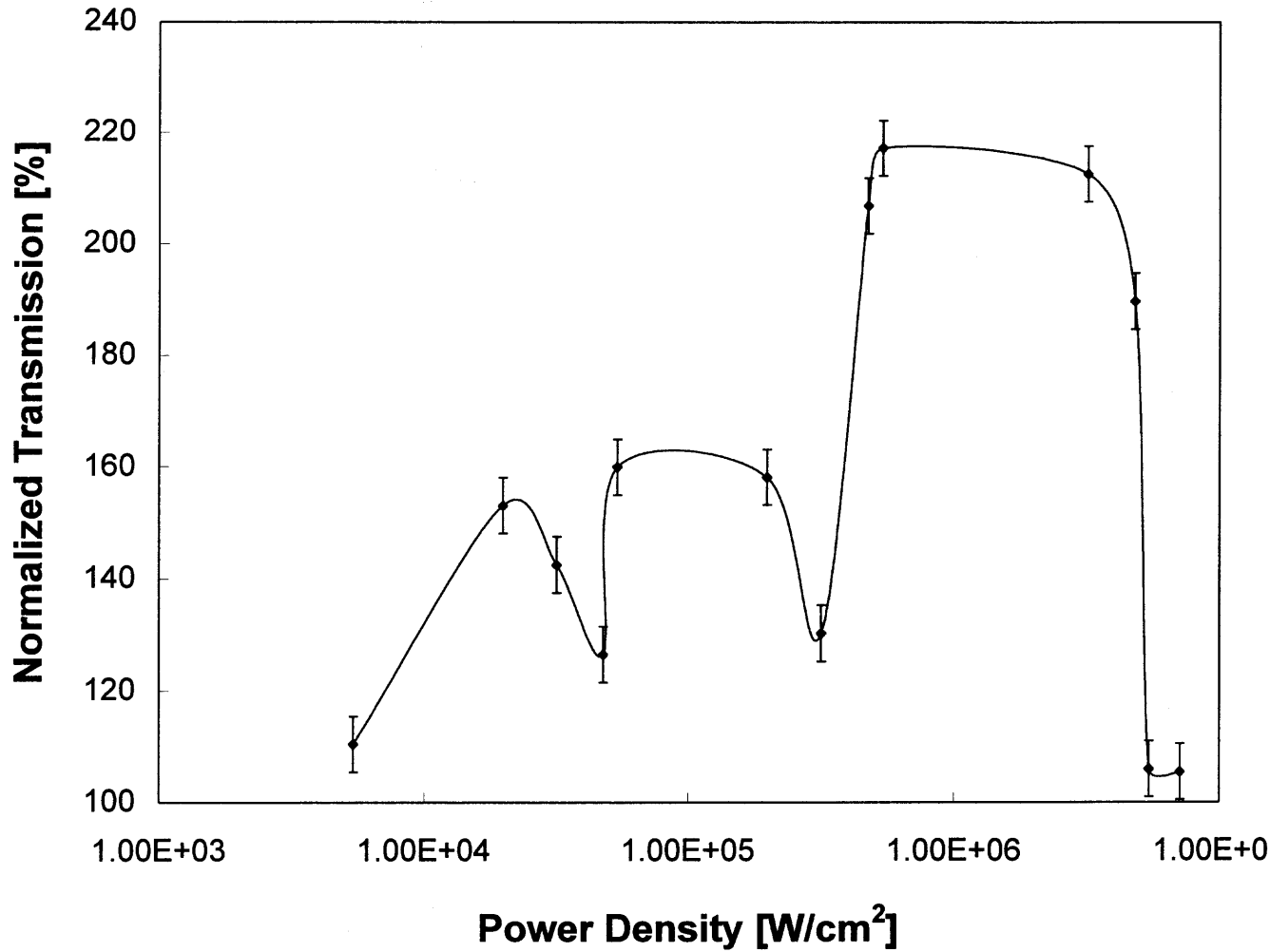
Fig. 5.6   Normalized transmission of the Er implanted red opal as a of function input light (H-polarization) intensity at latitude angle of $\theta = 50^0$. (Normalization is done with reference to non implanted sample)

The results of the nonlinear optical experiments may be explained as follows. The opaline matrix is composed of three dimensional periodic grating structure. The grating with a wave number K, affect the dispersion of the propagating optical beam with a wave number, k_n, inside the opal matrix. A resonance occurs when the following dispersion relation is met [49]

$$|k_n - K| \approx k_n \qquad (5.7.1)$$

Thus a resonance occurs at specific incident angles. If we treat cross section of opaline matrix as composed of two perpendicular gratings. The longitudinal periodicity along <111> direction being $m_z \ 0.816D = \frac{2\pi}{K_z}$, due to the close packing along the specified crystallographic plane where, D is the diameter of opal sphere. The transverse periodicity in the t direction has two gratings in the crystallographic directions namely <100> and <110>. Hence the transverse periodicity in opaline structure is either, $m_t D / 2 = 2\pi / K_t$, where $m_t = 1,2,3,\ldots\ldots$, or $m_t 0.816D = \frac{2\pi}{K_t}$. One combination contributes to a transmission only mode i.e. $D = 300nm$, $n_{eff} = 1.22$, $m_z = 1$ (a monolayer of Er implanted silica spheres) and $m_t = 2$ in the <100> direction. Two magic incident angles exist: $\theta = 7.7^0$ and $\theta = 48.8^0$. The later is in very good agreement with our experimental value of $\theta \approx 50^0$. Due to experimental limitations, we could not verify the experiment at the other angle namely $\theta = 7.7^0$.

Photoluminescence [50] experiments were performed on the Er implanted opal samples. The excitation used in the luminescence experiments is a 400 mW Ar ion laser emitting a 514 nm green line. The excitation beam from Ar ion laser impinged from the back at a given latitude angle and the photoluminescence light was collected by a quartz

lens and focussed onto the spectrometer through a bandpass filter. We took care to see that the bandpass filter did not contribute to the luminescence characteristics. Neither excitation nor the viewing angle affected the spectral shape of the luminescence curve, although it did affect the amplitude of the same. For example, erbium implanted green (silica ball diameter = 245 nm) showed an increased signal at large angles. The largest luminescence signal is obtained for the orange (silica ball diameter = 275 nm) opal samples. While Er implanted red and blue opal samples exhibited spectra typical of nonimplanted opal samples. Representative of the luminescence results at room temperature of the Er implanted green opal and nonimplanted substrate of the same sample are shown in Fig 5.7. The data for samples before annealing at 850 ^{0}C resembles that of a nonimplanted opal matrix. The Er line [47] at 1.54μm serves as a reference. Also we detected a peak at $\lambda = 0.9\mu m$ for the Er implanted region as opposed to a peak at $\lambda = 1.1\mu m$ for nonimplanted opal matrix.

We observed that although the luminescence spectrum was independent of the excitation or viewing angle, the efficiency of the luminescence was angle dependent illustrating coupling of the excitation wavelength to the periodic structure of silica opal. The luminescence is an incoherent process with a broad spectrum. Hence, the respective sample's geometry is the reason behind different sample's luminescence efficiency. In addition, as the implanted region occupied only a monolayer of silica spheres; hence we postulate the maximum luminescence efficiency correlated to the optimized imaging conditions. The self-imaging distance [51] for sub-wavelength spheres is analytically unknown, but may be given by, $Ls \approx \frac{s.4\pi k_0 n_{eff}}{K_t^2}$, with $s = 1,2,3,.......$ At an optimal
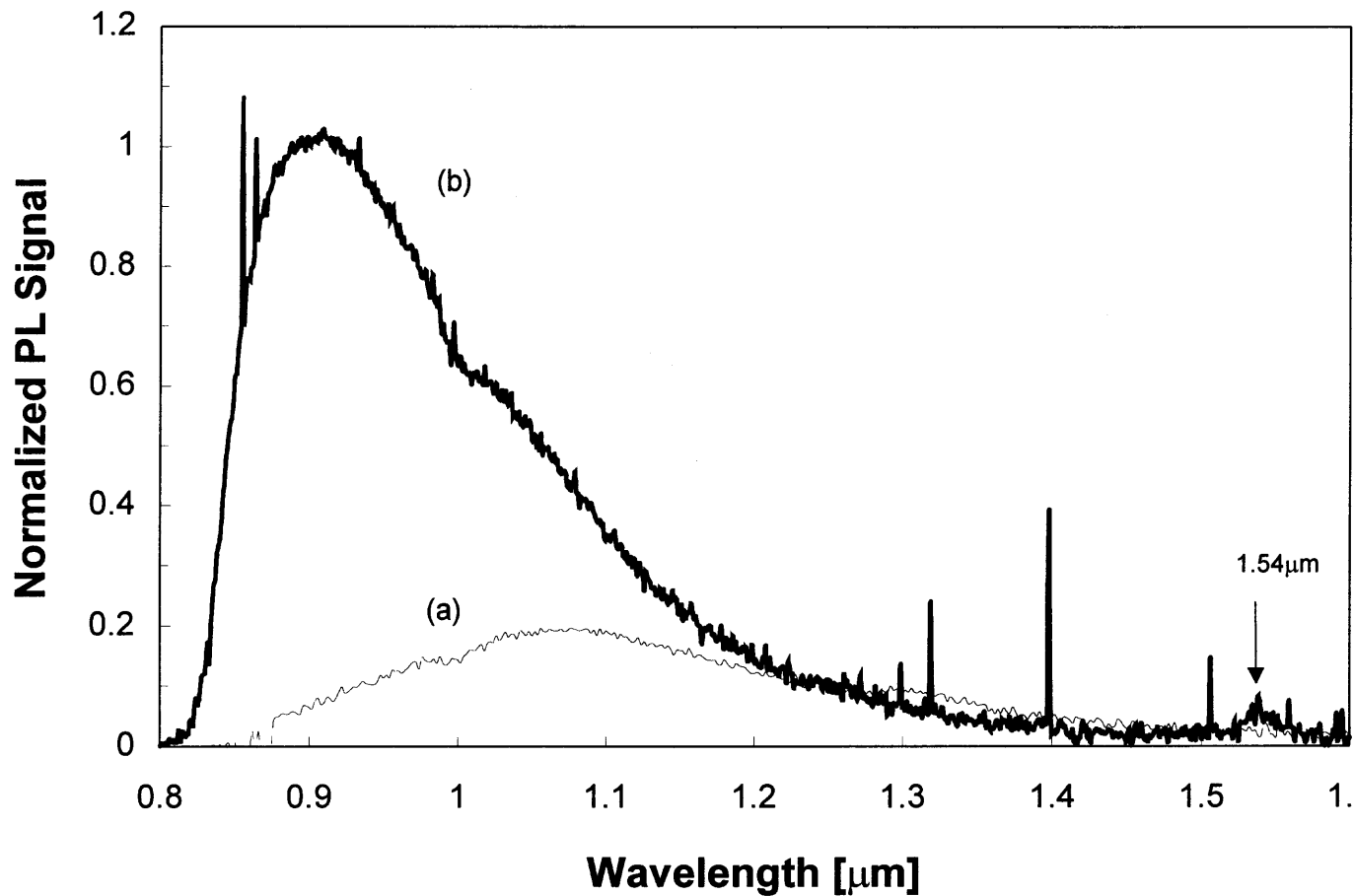
Fig. 5.7   Photoluminescence of (a) non-implanted and (b) Er implanted regions of a

'green' (245 nm sphere) opal sample excited by a λ=0.514 μm line of an

Ar laser at an incident angle of θ=30° from the back and at a viewing angle

of 15°.

wavelength, the implanted depth, L_{imp} contains integral number of self-imaging distances from various opal planes. For example, the optimal peak wavelength for the Er implanted "green" opal (i.e. sphere diameter = 245 nm) $D = 245 nm$ and $L_{imp} = 612.5 \pm 80 nm$, results in $\lambda_{opt} \approx 1000 nm = 1 \mu m$. The radiation from Er implanted silica, which possesses two radiation peaks in the spectral region, namely $\lambda = 0.85 \mu m$ and $\lambda = 0.98 \mu m$ is therefore enhanced by this lensing effect. The optimal peak wavelength of Er implanted "red" opal with $D = 0.3 \mu m$ and $L_{imp} = 0.75 \mu m$, is $\lambda_{opt} = 1.3 \mu m$.

The luminescence peak around $\lambda = 1.1 \mu m$ i.e. 0.9 eV for non-implanted "red and "blue" samples is attributed to the existence of defect states between Si nanoclusters and silica matrix of opal [52]. Non passivated dangling bonds are responsible for the luminescence signal although in the past, this band was observed at low temperatures. The existence of Si nanoclusters in our non implanted opal samples was confirmed through the X-Ray Diffraction (XRD) [50].

CHAPTER 6

APPLICATIONS AND FUTURE SCOPE OF RESEARCH

During the course of present chapter, we introduce possible applications of the materials discussed in the dissertation and projections for the future directions of research.

6.1   Wavelength Conversion Using Four Wave Mixing

Wavelength Division Multiplexed (WDM) [53] networks make very effective utilization of the fiber bandwidth and offer flexible interconnects based on wavelength routing. In high capacity WDM networks, blocking due to wavelength contention can be reduced by wavelength conversion [54]. Wavelength conversion addresses a number of important issues including transparency, interoperability and network capability. The number of wavelengths in WDM networks determine the number of independent wavelength addresses or paths. Although this number may be large enough to fulfill the required information capacity, it is often not large enough to support large number of nodes. In such cases, the blocking probability rises due to possible wavelength contention with two channels at the same wavelength at the same output. This point is illustrated in Fig 6.1, whereby the network operators 1, 2, and 3 are responsible for their own subnetworks and wavelength assignments within the subnetwork which are independent of other network operators. But the need of the wavelength conversion arises with the linking between these subnetworks. This is shown as points of wavelength conversion in Fig. 6.1.
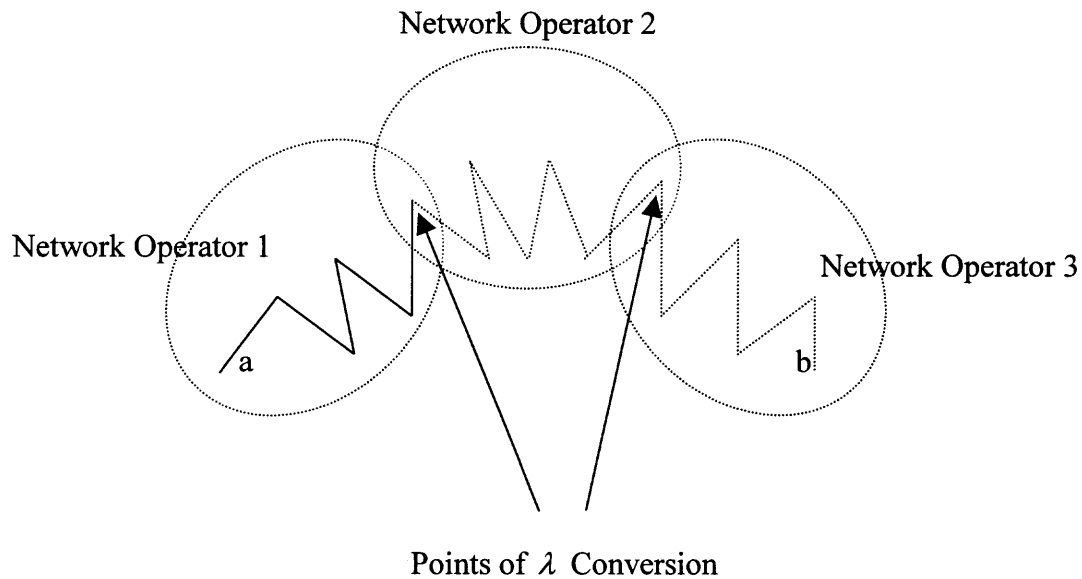
Fig. 6.1   Interconnected WDM networks and need of wavelength conversion

Wave-mixing rises from a nonlinear optical response of a medium when more than one wave is present. The outcome of the wave-mixing effect is another wave whose intensity is proportional to the product of the interacting wave intensities. The phase and frequency of the generated wave is a linear combination of those of the interacting waves. Hence, the wave-mixing preserves both phase and amplitude information, and therefore is the only category of wavelength conversion that offers strict transparency as compared to other wavelength conversion techniques including optoelectronic conversion, cross gain and phase modulation in semiconductor amplifiers.

A semiclassical picture of four-wave-mixing [10] includes the formation of a grating and scattering of a wave off the grating. Two optical waves form a grating due to

intensity patterns in the nonlinear medium. This can either be a standing wave grating if the two waves have identical frequency and no relative phase jitters. The nonlinear material in our case the silicon naocluster film responds to this intensity grating by forming a refractive index grating so called Kerr grating. If two waves differ in frequency, the grating pattern sweeps in space at a rate corresponding to the frequency difference. The third beam present in the film is scattered by the grating. This scattered wave is the wave generated as a result of the four-wave-mixing interaction of the three incident waves. The frequency of the generated wave is offset from that of the third wave by the frequency difference of the first two waves. The intensity of the generated beam is related to the intensities of the interacting beam and the magnitude of the third order susceptibility,

$$I_4 \propto \left|\chi^{(3)}\right|^2 I_1 I_2 I_3 \qquad (6.1.1)$$

The high values of the $\chi^{(3)}$ obtained for the Si nanoclusters prepared by the laser ablation makes them an ideal candidate for the application of wavelength conversion in WDM networks.

6.2   Raman Amplifiers

For quite some time in the past, the microwave communication links were preferred to optical ones due to the availability of the amplifiers in the microwave domain. The optical links had to follow 3R regeneration i.e. retiming, reshaping and reclocking optical-to-electrical and electrical-to-optical conversion. This drawback of the optical links is overcome by the use of rare earth doped fiber amplifiers (EDFA) [48]. Of late a new kind of amplifier based on the Stimulated Raman Scattering (SRS) [55] has

attracted the mind of many fiber optics communications researchers as this may convert the attenuating piece of transmission media i.e. fiber into a gain medium. Raman amplification has the advantage of being all optical process also stretching the link length longer than before. As compared to EDFA, one does not have to use a separate portion of erbium doped fiber of few meters length.

SRS is a strong scattering process whereby a photon of frequency ω is destroyed and a photon at the Stokes shifted frequency $\omega_s = \omega - \omega_v$ is created leaving the molecule in an excited state. This process is shown in Fig. 6.2.
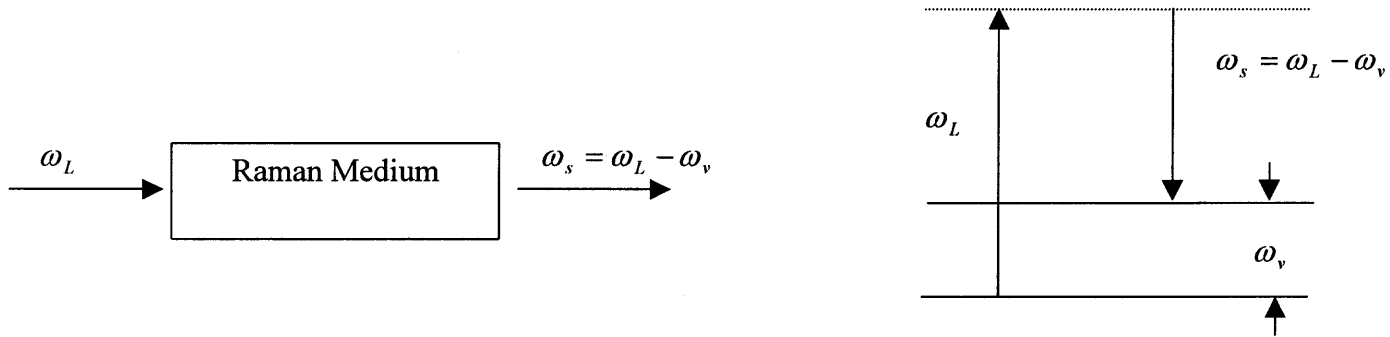
Fig. 6.2   Stimulated Raman scattering

The spatial evolution of the Stokes wave follows the following equations given by [12]

$$\frac{dA_s}{dz} = -\alpha_s A_s \tag{6.2.1}$$

and α_s is the Stokes absorption coefficient given by

$$\alpha_s = -12\pi i \frac{\omega_s}{n_s c} \chi_R^{~3}(\omega_s)|A_L|^2 \tag{6.2.2}$$

where,

ω_s = Stokes frequency,

n_s = refractive index at the Stokes frequency,

c = speed of light in vacuum,

$\chi_R^3(\omega_s)$ = real part of the third order susceptibility,

A_L = amplitude of the pump optical field

The laser ablated silicon film described in the second chapter with high valued nonlinear third order susceptibility values is a good candidate for the Raman amplifier films.

6.3   Si Implanted Opal Structure

Photoluminescence (PL) studies [35] carried out on the silicon implanted opal structures reveal a large PL signal in comparison to the silicon implanted in flat silica matrix. Also we observed different PL signal intensity for the different silica opal feature size i.e. ball diameter. In Fig. 6.2 we represent the comparative PL signals for 3 samples namely the silicon implanted in smooth silica and in two of the opal matrices with feature size of 245 nm i.e. green opal and 300 nm i.e. red opal. This PL data were obtained with Ar laser at λ=514 nm (100 mW average power) and a SPEX spectrometer with a cooled photomultiplier tube.

The PL signal enhancement in the case of opaline samples may be attributed to the difference between the flat and opaline matrix's material i.e. the difference in the preparation of silica matrix and hence thereby to the surface states. The matrix geometry also plays an important role in optimum coupling of the Ar pump light to the Si nanoclusters as can be grasped by the magnitude difference in the green and red

implanted samples. This kind of luminescence itself may be very useful for the optical devices based on the silicon technology. Also through the use of the three dimensional photonic crystal in this case silica opal and changing the feature size of the same one may tune the PL efficiency of the silicon nanostructures embedded within the opal matrix. This kind of tunable PL intensity with respect to the opaline matrix feature size would pave the way for the silicon based optoelectronic transmitters.

The nonlinear behavior of the silicon implanted opal matrix might be used as a built in limiter for the laser with the silicon nanocrystals, which would reduce the output light from the silicon implanted opal structure for high intensities. Embedding different organic dye molecules within the opal may achieve the lasing action in the opal structure. In these kind of application the opal matrix is being used as a highly reflecting mirror in three dimensions and one can have a microcavity formed within the opaline matrix.

6.4   Erbium Implanted Opal Matrix Aplifier

In the past few years, erbium doped fiber amplifiers (EDFA) [48] have enabled fiber optic transmission systems to increase in capacity by more than a hundred-fold. EDFAs open the way to all-optical amplification of the transmission signals. With the recent explosive growth in optical transmission networks, both undersea and terrestrial, the fiber amplifying fabric has become an essential building block these networks. The attenuation of the signal in the optical fiber link can be counteracted by employing the EDFA along the link. As we discussed in chapter four, with the erbium ion implanted silica opal of appropriate feature size, one would have a photoluminescence signal at
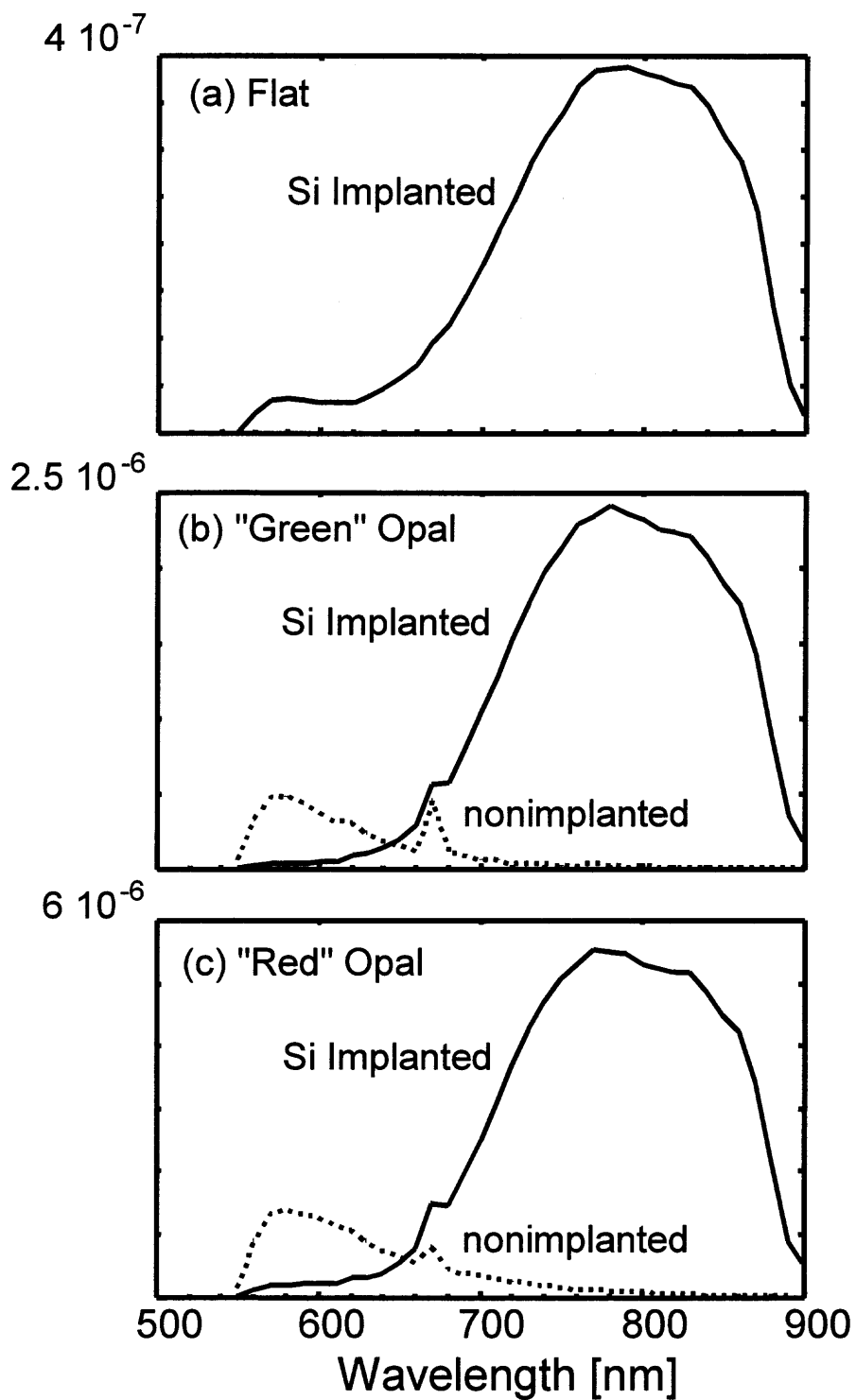
Fig. 6.3 Comparative photoluminescence data for Si nanoclusters in different silica matrices

1.54 μm, which is where the third window of the fiber optic communication is located. With this kind of amplifying medium, one would be able to have an all optical amplifier with a thin opal matrix implanted with Er ions of thickness of few microns rather than using few meters of length of erbium doped silica glass fiber.

During late 1980's or so the optical fiber communication links in the second optical fiber communication window are laid in different parts of the world. This window was much useful due to zero or low dispersion offered by the silica fibers when operating in the 1.3 μ m wavelength region. It is an estimate that about 50m million kilometers of standard fiber whose performance is optimized for 1.3 μ m operation. Clearly these communication links would benefit from the optical amplifiers operating near 1.3 μ m. It has been long known that the praseodymium (Pr) doped silica fibers [56] are the amplifying medium for the 1.3 μ m communication window. One may also test the gain possibility of praseodymium (Pr) doped opal in the future work on the amplifiers in the 1.3μm region.

6.5   Pulse Compression & Dispersion Management

Basic idea of optical pulse compression is borrowed from chirp radar where chirped pulses at microwave frequencies are compressed by passing them through dispersive delay line i.e. a combination of frequency chirp followed by the dispersion compensator. Periodic structures such as diffraction gratings are historically used for achieving pulse compression. Photonic crystals such as silica opal which comprises of three dimensional diffraction gratings have the potential of being used for the same purpose.

Recent studies [57] have paved the way of achieving the nonlinear optical pulse compression by incorporating the silicon nanoclusters in the silica opal through the ion implantation. Unlike Bragg fibers, here the researchers employed a transverse scheme, namely, the dispersion is achieved via transverse Bragg reflections while maintaining non-resonance conditions along the direction of propagation of the optical pulse.

Dispersion management is an important aspect of today's optical fiber communication systems whereby the ill effects of pulse spreading by the communication grade fiber are undone by the use of a Dispersion Compensator. The problem of dispersion compensation has become more relevant with the deployment of fiber amplifiers whereby loss of the fiber is no more a limiting factor for the optical link length. In some sense, optical amplifiers solve the loss problem but worsen the dispersion problem since, in contrast to the electronic regenerators , an optical amplifier does not restore the amplified signal to its original state. As a result the dispersion induced degradation of the transmitted signal accumulates over multiple amplifiers. Usually the dispersion management is undertaken by using a Dispersion Compensating Fiber (DCF) which offers opposite signed dispersion as offered by the communication grade fiber. The typical attenuation offered by the DCF is on the order of 0.5 dB/km at $1.3\,\mu$m. The nonlinear dispersion properties of the photonic crystals can be used in this direction. In a broader perspective one may be able to use the above mentioned Er implanted opal structure for both purposes of achieving optical gain and tackling the dispersion management problem.

6.6   Optical Logic Gates

Switching is an essential operation not only in telecommunications but also in digital computers and signal processing etc. One of the fundamental building blocks for switches is the logic gate. The current rapid deployment of all optical networks has created a need of high capacity repeaters and terminals for processing optical signals and therefore a need of high speed optical logic devices [58].

Optical logic operations are preferred over the electronic logic due to following basic reasons:

a. Speeds exceeding 50 GB/s can be achieved with optical logic which is beyond the rates at which electronic systems can be expected to operate.

b. By processing optically we avoid the bottlenecks caused by the conversion between optics and electronics. This is of particular interest to the all optical networks where the information enters and leaves the node in optical format.

The simple thin film containing the Si nanoclusters studied during the dissertation may be employed for the purpose of realizing an all optical inverter, OR logical gate.

In high intensity region the optical absorption coefficient can be modelled as

$$\alpha = \alpha_0 + \beta I$$

where in our case typically β is negative.

Consider an all optical inverter as shown in Fig. 6.3. The input laser beam is split by the beam splitter into the splitting ratio of 95:5 into I_1 and I_2 i.e. into a strong and weak beam respectively. The strong and the weak beams are focussed onto the same spot on the laser ablated Si nanocluster film. When the strong beam is on, the transmission through the nonlinear film increases and hence one will get high transmission of the weak
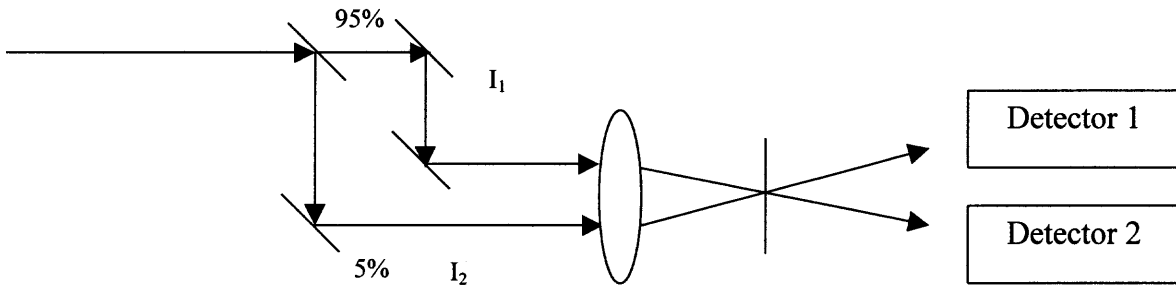
Fig. 6.4   All optical inverter based on Si nanocluster film

beam and vice versa for the other case. The obvious advantage of the collecting the reflected beams to get the NOT of the above operation gives an added advantage to the all optical logical devices. One can also get the logical OR functionality by making 2 strong beams and one weak beam interacting in the nanocluster film.

CHAPTER 7

CONCLUSIONS

During the course of this dissertation, two different nano systems are studied with respect to their linear and nonlinear optical properties. One was Laser Ablated silicon nanoclusters passivated under the influence of Ar, H_2 and He. The other class of materials consisted of ion implanted species of Si, Ge and erbium within silica opal – a three dimensional photonic crystal.

Our investigations into the laser ablated films containing silicon nanoclusters grown under the passivation of Ar, H_2 and He, revealed that the nonlinear refractive index change Δn for these films was about $1/10^{th}$ to $1/2$ of the values of the non passivated Si nanocluster films. The maximum value of the Δn was -0.2 for the He passivated film at $\lambda = 640$ nm. We observed nonlinear refractive index variation with respect to the different passivating environment, which we believe is a step towards understanding the role of surface states in the nonlinear process.

The remaining of the dissertation was devoted to semiconductor implanted photonic crystals. We chose to implant the silicon and germanium nanoclusters into the silica opal owing to their wide spread use in the electronic world. Through the experimentation on the silicon implanted opal structure, we found that, we have achieved very large nonlinear index change at intensities which are about three orders of magnitude lower than those used for non-opaline structures. The large nonlinear refraction was correlated with transverse scattering perpendicular to the direction of wave propagation.

Lastly we investigated the Er implanted silica opal structure and found that the implantation dose of 10^{14} cm^{-2} at 2.7 MeV had left the opal matrix undamaged. Large nonlinear transmission obtained through the Er implanted photonic crystal is once again correlated to the transverse Bragg planes inside the photonic crystal.

These nano materials and structures open the door for novel optoelectronic devices. The 'nano with nano' concept obtained through incorporating nano semiconductor clusters within periodic silica structures may hold a true solution to low intensity nonlinear all optical switches and filters.

APPENDIX

Z-SCAN THEORY [16]

In this section we formulate the theoretical background for analyzing the Z-Scan technique.

In general, for the case of cubic nonlinearity, the index of refraction n is expressed in terms of nonlinear indices n_2 (esu) or γ (m^2/W) through

$$n = n_0 + \frac{n_2}{2}\left|E^2\right| = n_0 + \gamma I = n_0 + \Delta n(I) \qquad (A.1)$$

where n_0 is the linear index of refraction, E is the peak electric field (cgs), and I denotes the irradiance (MKS) of the laser beam within the sample. (n_2 and γ are related through the conversion formula n_2 (esu) $= (cn_0 / 40\pi)\gamma(m^2 / W)$ where $c(m/s)$ is the speed of light in vacuum.) Assuming a TEM$_{00}$ Gaussian beam of light waist radius w_0 travelling in $+z$ direction, we can write E as

$$E(z,r,t) = E_0(t)\frac{w_0}{w(z)}.\exp\left(-\frac{r^2}{w^2(z)} - \frac{ikr^2}{2R(z)}\right)e^{-i\phi(z,t)} \qquad (A.2)$$

where $w^2(z) = w_0^2(1 + z^2 / z_0^2)$ is the beam radius, $R(z) = z(1 + z_o^2 / z^2)$ is the radius of curvature of the wavefront at z, $z_0 = kw_o^2 / 2$ is the diffraction length, i.e., the Rayleigh Distance of the beam, $k = 2\pi / \lambda$ is the wave number, and λ is the laser wavelength, all in free space. $E_0(t)$ is the radiation electric field at the focus and contains the temporal envelope of the laser pulse. The co-ordinate axis used for the Z-scan theoretical analysis are depicted in Fig. A.1. The $e^{-i\phi(z,t)}$ term contains all the radially uniform phase variations. Since we are only concerned with calculating the radial phase

variations $\Delta\phi(r)$, the slowly varying envelope approximations (SVEA) [16] applies, and all other phase changes that are uniform in r are ignored.
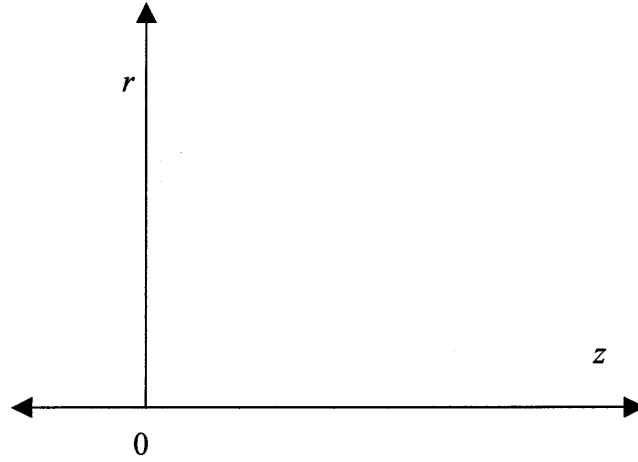
Fig. A.1   Co-ordinate axis configuration for Z-scan analysis

If the sample length is small enough that changes in beam diameter within the sample due to either diffraction or nonlinear refraction can be neglected, then we may regard this medium as "thin," in which case self refraction is regarded as "external self action". For linear refraction, this implies that $L \ll z_0$, and for nonlinear refraction, $L \ll z_0 / \Delta\phi(0)$ [59]. In most of the Z-Scan experiments the second critical condition is automatically met since $\Delta\phi$ is small. Also it is found that first criterion can be made less restrictive to $L < z_0$ [16]. This assumption simplifies the problem considerably, and the amplitude $\sqrt{I}$ and ϕ of the electric field as a function of z' are governed by SVEA by a pair of simple equations:

$$\frac{d\Delta\phi}{dz'} = \Delta n(I)k \qquad (A.3)$$

$$\frac{dI}{dz'} = -\alpha(I)I \tag{A.4}$$

where z' is the propagation depth in the sample and $\alpha(I)$, in general includes linear and nonlinear absorption terms. Note that z' should not be confused with the sample position z. In the case of cubic nonlinearity, Eq. (A.3) and (A.4) are solved to get the phase shift $\Delta\phi$ at the exit surface of the sample which follows the radial variation of the incident irradiance at a given position of the sample z. Thus,

$$\Delta\phi(z,r,t) = \Delta\phi_0(z,t)\exp\left(-\frac{2r^2}{w^2(z)}\right) \tag{A.5}$$

with

$$\Delta\phi_0(z,t) = \frac{\Delta\phi_0(t)}{1+\dfrac{z^2}{z_0^2}} \tag{A.6}$$

where $\Delta\phi_0(t)$, is on axis phase shift at the focus, and is defined as

$$\Delta\phi_0(t) = k\Delta n_0(t)L_{eff}$$

where
$$L_{eff} = (1-e^{-\alpha L})/\alpha \tag{A.7}$$

with L the sample length and α the linear absorption coefficient. Here $\Delta n_0 = \gamma I_0(t)$ with $I_0(t)$ being on axis irradiance at the focus (i.e. $z = 0$). We ignore Fresenel reflection losses, for example $I_0(t)$ is the irradiance within the sample.

The complex electric field exiting the sample E_e now contains the nonlinear phase distortion

$$E_e(z,r,t) = E(z,r,t)e^{-\alpha L/2}e^{i\Delta\phi(z,r,t)} \tag{A.8}$$

From the Huygen's principle, one can obtain the far field pattern of the beam at the aperture plane through a zeroth-order Henkel transformation of E_e. We follow a method called "Gaussian Decomposition" [59] which is more suitable for Gaussian beams. In this method, we decompose the complex electric field at the exit plane of the sample into a summation of Gaussian beams through a Taylor series expansion of the nonlinear phase term $e^{i\Delta\phi(z,r,t)}$ in Eq. (A.8). That is

$$e^{i\Delta\phi(z,r,t)} = \sum_{m=0}^{\infty} \frac{[i\Delta\phi_0(z,t)]^m}{m!} e^{-2mr^2/w^2(z)} \qquad (A.9)$$

Each Gaussian beam now propagates to the aperture plane where it will contribute to reconstruct the beam. We write the resultant electric field pattern at the aperture as

$$E_a(r,t) = E(z,r=0,t)e^{-\alpha L/2} \sum_{m=0}^{\infty} \frac{[i\Delta\phi_0(z,t)]^m}{m!} \frac{w_{m0}}{w_m}.\exp\left(-\frac{r^2}{w_m^2} - \frac{ikr^2}{2R_m} + i\theta_m\right) \qquad (A.10)$$

Defining d_1 as the propagation distance in free space from the sample to the aperture plane and $g = 1 + d_1/R(z)$ the remaining parameters in Eq. (A.10) are expressed as

$$w_{mo}^2 = \frac{w^2(z)}{2m+1}$$

$$d_m = \frac{kw_{mo}^2}{2}$$

$$w_m^2 = w_{mo}^2\left[g^2 + \frac{d_1^2}{d_m^2}\right]$$

$$R_m = d\left[1 - \frac{g}{g^2 + d_1^2/d_m^2}\right]^{-1}$$

$$\theta_m = \tan^{-1}\left[\frac{d_1/d_m}{g}\right]$$

The expression given by Eq.(A.10) is a general case derived by Weaire whereby the collimated beam of $R = 0$ is considered for which $g = 1$.

The Transmitted power through the aperture is obtained by spatially integrating $E_a(r,t)$ up to the aperture radius r_a, giving

$$P_T(\Delta\phi_0(t)) = c\varepsilon_0 n_0 \pi \int_0^{r_a} |E_a(r,t)|^2 r\, dr \qquad (A.11)$$

where ε_0 is the permittivity of vacuum. Including the pulse temporal variation, the normalized Z-Scan transmittance $T(z)$ can be calculated as

$$T(z) = \frac{\int_{-\infty}^{\infty} P_T(\Delta\phi_0(t))dt}{S \int_{-\infty}^{\infty} P_i(t)dt} \qquad (A.12)$$

where $P_i(t) = \pi w_0^2 I_0(t)/2$ is the instantaneous input power within the sample and $S = 1 - \exp(-2r_a^2 / w_a^2)$ is the aperture linear transmittance, w_a denoting the beam radius at the aperture in the linear regime.

For the cubic nonlinearity and a small phase change the on-axis Z-Scan transmittance can be obtained by letting $r = 0$ in Eq. (A.10). Also due to small phase change i.e. $|\Delta\phi| \ll 1$, only two terms in Eq. (A..10) are retained. One arrives at the normalized Z-Scan transmittance as given by

$$T(z,\Delta\phi) = \frac{|E_a(z,r = 0, \Delta\phi_0)|^2}{|E_a(z,r = 0, \Delta\phi_0 = 0)|^2}$$

$$= \frac{\left| (g + i\, d/d_0)^{-1} + i\Delta\phi_0 (g + i\, d/d_1)^{-1} \right|^2}{\left| (g + i\, d/d_0)^{-1} \right|^2}$$

(A.13)

The far field condition $d \gg z_0$, can be used to further simplify Eq. (A.13) to get the geometry independent normalized transmittance as

$$T(z, \Delta\phi_0) \approx 1 - \frac{4\Delta\phi_0 x}{(x^2 + 9)(x^2 + 1)}$$

(A.14)

where $x = z / z_0$.

The Z-Scan theory described above can be extended to include the nonlinear absorption effects in the nonlinear sample. To develop this theory, we analyze two-photon absorption (2PA), in semiconductors with $E_g < 2\hbar\omega < 2E_g$, where E_g is the bandgap energy and ω is the optical frequency. The third order nonlinear susceptibility is considered to be a complex quantity, given by,

$$\chi^{(3)} = \chi_R^{(3)} + i\chi_I^{(3)}$$

(A.15)

The imaginary part is related to the 2PA coefficient through

$$\chi_I^{(3)} = \frac{n_0^2 \varepsilon_0 c^2}{\omega} \beta$$

(A.16)

and real part is related to γ through

$$\chi_R^{(3)} = 2n_0^2 \varepsilon_0 c \gamma$$

(A.17)

We neglect the free-carrier effects as we are concerned with low excitation regime. In view of this approximation we write:

$$\alpha(I) = \alpha + \beta I$$

(A.18)

This yields the irradiance distribution and phase shift of the beam at the exit surface of the sample as

$$I_e(z,r,t) = \frac{I(z,r,t)e^{-\alpha L}}{1+q(z,r,t)}$$

(A.19)

and

$$\Delta\phi(z,r,t) = \frac{k\gamma}{\beta}\ln[1+q(z,r,t)]$$

(A.20)

where $q(z,r,t) = \beta I(z,r,t)L_{eff}$. Combining Eq. (A.19) and (A.20), we obtain the complex field at the exit surface of the sample as

$$E_e = E(z,r,t)e^{-\alpha L/2}(1+q)^{(ik\gamma/\beta-1/2)}$$

(A.21)

Above equation reduces to Eq. (A.8) in the limit of no two photon absorption. A zeroth order Henkel transform of Eq. (A.21) gives the field distribution at the aperture which then can be used in Eq.(A.11) and (A.12) to yield the transmittance. For $|q| < 1$, following a binomial series expansion in powers of q, Eq.(A.21) can be expressed as an infinite sum of Gaussian beams similar to the purely refractive case described earlier as follows:

$$E_e = E(z,r,t)e^{-\alpha L/2}\sum_{m=0}^{\infty}\frac{q(z,r,t)^m}{m!}\cdot\left[\prod_{n=0}(ik\gamma/\beta-1/2-n+1)\right]$$

(A.22)

where Gaussian spatial profiles are implicit in $q(z,r,t)$ and $E(z,r,t)$. The complex field pattern can be obtained as we derived in Eq.(A.10). The result is represented by Eq. (A.10) if we substitute the $(i\Delta\phi_0(z,t))^m/m!$ terms in the sum by

$$f_m = \frac{(i\Delta\phi_0(z,t))^m}{m!}\prod_{n=0}^{m}\left(1+i(2n-1)\frac{\beta}{2k\gamma}\right)$$

(A.23)

with $f_0 = 1$. Note that the coupling factor $\beta/2k\gamma$ is the ration of the imaginary to real part of the third order nonlinear susceptibility. $\chi^{(3)}$.

As evident from Eq. (A.23), the absorptive and refractive contributions in the far field beam profile and hence open and close aperture Z-Scan transmittance are coupled. When the aperture is removed, however Z-Scan transmittance is only a function of nonlinear absorption.. The total transmitted fluence in the open aperture case can be calculated by spatially integrating Eq. (A.19) without having to include the free space propagation process. Integrating Eq. (A.19) at z over r, we obtain the transmitted power $P(z,t)$ as follows:

$$P(z,t) = P_i(t)e^{-\alpha L}\frac{\ln[1+q_0(z,t)]}{q_0(z,t)}\qquad\text{(A.24)}$$

where $q_0(z,t) = \beta I_0(t)\dfrac{L_{eff}}{(1+z^2/z_0^2)}$ and $P_i(t)$ is defined in Eq. (A.12). For a temporally Gaussian pulse above equation can be integrated to give the normalized energy transmittance

$$T(z,S=1) = \frac{1}{\sqrt{\pi}q_0(z,0)}\int_{-\infty}^{\infty}\ln[1+q_0(z,0)e^{-\tau^2}]d\tau\qquad\text{(A.25)}$$

For $|q_0| < 1$, this transmittance can be expressed in terms of peak irradiance in a summation form more suitable for numerical evaluation:

$$T(z,S=1) = \sum_{m=0}^{\infty}\frac{[-q_0(z,0)]^m}{(m+1)^{3/2}}\qquad\text{(A.26)}$$

Thus once the open aperture Z-Scan is performed, nonlinear absorption coefficient β can be determined. Usually a simplified form of the above Eq. (A.26) is used by considering only first two terms of the summation and is given by

$$T(z, S = 1) = 1 + \frac{\beta I_0(t) L_{eff}}{(1 + \frac{z^2}{z_0^2}) 2^{3/2}} \qquad (A.27)$$

REFERENCES

1. J. Gowar, "Optical Communication Systems", *Prentice-Hall International*, Second Edition 1995.

2. G.P. Agrawal, "Fiber-Optic Communication Systems", *John Wiley & Sons*, Second Edition 1997.

3. J. M. Senior, "Optical Fiber Communication", *Prentice Hall International*, Second Edition 1996.

4. Near Margalit, S.Z. Zhang, J. Bowers, "Vertical cavity lasers for telecom applications", *IEEE Communications Magazine*, Vol. 25, pp. 164-170, May 1997.

5. Stanely Wolf and Richard Tauber, " Silicon Processing for the VLSI era: Process Technology", *Lattice Press*, 1999.

6. Mark Hybertson, " Absorption and emission of light in nanoscale silicon structures", *Physical Review Letters*, 72(10), 1514-1517, 1994.

7. S.S. Iyer, Y.-H.Xie, " Light emission from silicon", *Science*, 260, 40-46, 1993.

8. Z.H.Lu, D.J.Lockwood & J.-M.Barlbeau, " Quantum confinement and light emission in SiO_2/Si superlattices", *Nature*, 378, 258-260, 1995.

9. S. Vijayalakshmi, H. Grebel, Z. Iqbal, C.W. White, "Artificial dielectrics: nonlinear properties of Si nanoclusters formed by ion implantation in SiO_2 glassy matrix", Journal of Applied Physics, 84(12), 6502-6506, 1998.

10. Electro-Optics Handbook, Edited by Ronald Waynant and Marwood Ediger, Chapter 13 "Nonlinear Optics", by Gary Wood and Edward Sharp, *McGraw Hill Publishers*, 1993.

11. Constantine A. Balanis, "Advanced Engineering Electromagnetics", *John Wiley & Sons*, 1989.

12. Robert W. Boyd, "Nonlinear Optics", *Academic Press, Inc*, 1992.

13. Laser Ablation: Principles and Applications Edited by J.C. Miller, *Springer Verlag*, 1994.

14. Plused Laser Deposition of Thin Films Edited by D. Chrisey and G. K. Hubler, *John Wiley & Sons*, 1994, Chapter 13 "Comparison of Vacuum Deposition Techniques" by Graham Hubler.

15. Joseph T. Verdeyen, "Laser Electronics", *Prentice Hall Publishers*, 1994.

16.   M. Sheik-Bahae, A.A.Said, Tai-Huei Wei, D. J. Hagan, E.W.Van Stryland, "Sensitive measurement of optical nonlinearities using a single beam", *IEEE Journal of Quantum Electronics*, **26**(4), 760-769, 1990.

17.   Ulrich Brackman, "Lambdachrome® laser dyes", 2'nd edition, *Lambda Physics GmbH*, 1997.

18.   M. Ajgaonkar, S. Vijayalakshmi, Y. Zhang, M.A. George, "The Role of Passivation in the Nonlinear Optical Properties of Silicon Nanoclusters", *Materials Research Society*, Spring Meeting 1999.

19.   S. Vijayalakshmi, F. Shen, H. Grebel, "Artificial Dielectrics: Nonlinear optical properties of silicon nanoclusters at λ=532 nm", *Applied Physics Letters*, **71**(23), 3332-3334, 1997.

20.   Yan Zhang, Zafar Iqbal, S. Vijayalakshmi, H. Grebel, " Stable hexagonal-wurtzite silicon phase by laser ablation", *Applied Physics Letters*, **75**(18), 2758-2760, 1999.

21.   T. Yoshoda, S. Takeyama, Y. Yamada, K. Mutoh, " Nanometer-sized silicon cystallites prepaperd by excimer laser ablation in constant inert gas pressure", *Applied Physics Letters*, **68**(13), pp 1772-1774, 1996.

22.   Costas M. Soukoulis Ed., "Photonic Band Gap Materials", *Kluwar Academic Publishers* NATO ASI Series, 1996.

23.   Eli Yablonovitch, " Inhibited spontaneous emission in solid-state physics and electronics", *Physical Review Letters*, **58**(20), 2059-2062, 1987.

24.   Sajeev John, "Strong localization of photons in certain disordered dielectric superlattices", *Physical Review Letters*, **58**(23), 2486-2489, 1987.

25.   E. Yablonovitch, "Photonic band-gap structures", *Journal of Optical Society of America B*, **10** (2), 283-295, 1993.

26.   W.M. Robertson, G. Arjavalingam, R.D. Meade, K.D. Brommer, A.M. Rappe, J.D. Joannopoulos, "Measurement of photon dispersion relation in two-dimensional ordered dielectric arrays", Journal of Optical Society of America B, **10**(2), 322-327, 1993.

27.   Shawn Lin, J.G. Fleming, "A Three Dimensional Optical Photonic Crystal", *IEEE Journal of Lightwave Technology*, **17**(11), 1944-1947, 1999.

28.   Alfons van Blaadren, ReneRuel, Pierre Wiltzius, "Template-directed colloidal crystallization", Nature, **385**, 321-324, 1997.

29. G. Subramania, K. Constant, R. Biswas, M.M. Sigalas, K.-M. Ho, "Optical photonic crystals synthesized from colloidal systems of polystyrene spheres and nanocystalline titania", *Journal of Lightwave Technology*, **17**(11), 1970-1974, 1999.

30. J.V. Sanders, "Colour of precious opal", *Nature*, **204**, 1151-1153, 1964.

31. Werner Stober, Arthur Fink, Ernst Bohn, " Controlled Growth of monodisperse silica spheres in micron size range", *Journal of Colloid and Interface Science*, **26**, 62-69, 1968.

32. Albert P. Philipse, "Solid opaline packings of colloidal silica spheres", *Journal of Materials Science Letters*, **8**, 1371-1373, 1989.

33. J.F. Ziegler, "Handbook of ion implantation technology", *North Holland Publications*, 1992.

34. Reimer, Ludwig, "Scanning electron microscopy: physics of image formation and microanalysis" , *Springer-Verlag*, 1985.

35. Y. Zhang, S. Vijayalakshmi, M. Ajgaonkar, H. Grebel, "Optical Properties of Ordered Array of Silica Nanospheres Embedded With Silicon Nanoclusters", accepted for publication in *Journal of Optical Society of America B*.

36. Jin Au Kong, "Electromagnetic wave theory", *Wiley Interscience Publications*, Second Edition, 1990.

37. Pochi Yeh, "Optical Waves in Periodic Media", *Wiley Interscience Publications*, 1988.

38. Takashi Yamasaki, Tetsuo Tsutsui, "Spontaneous emission from fluorescent molecules embeded in photonic crystals consisting of polystyrene microspheres", *Applied Physics Letters*, **72**(16), 1957-1959, 1998.

39. M. Ajgaonkar, Y. Zhang, H. Grebel, C.W. White, "Nonlinear optical properties of a coherent array of submicron SiO_2 spheres(opal) embedded with Si nanoparticles", *Applied Physics Letters*, **75**(11), 1532-1534, 1999.

40. S. Vijayalakshmi, H. Grebel, Z. Iqbal, C.W. White, "Artificial dielectrics: nonlinear properties of Si nanoclusters formed by ion implantation in SiO_2 glassy matrix", Journal of Applied Physics, **84**(12), 6502-6506, 1998.

41. E. Snoeks, A. van Blaaderen, C. M. van Kats, M. L. Brogersma, T. van Dillen and A. Polman, "Colloidal ellipsoids with continuously variable shape", submitted to Nature, 1999.

42. M. Ajgaonkar, Y. Zhang, H. Grebel, M. Sosnowski, D.C. Jacobson, "Linear and nonlinear optical properties of erbium-implanted coherent array of submicron silica spheres", *Applied Physics Letters*, **76**(26), 3876-3878, 2000.

43. Daniel M. Mittleman, Jane F. Bertone, Peng Jiang, Kevin S. Hwang, and Vicki L. Colvin, "Optical properties of planar colloidal crystals: Dynamical diffraction and the scalar wave approximation", *Journal of Chemical Physics*, **111**, 345-354 1999.

44. S. M. Sze, "Semiconductor Devices: Physics and Technology", *John Wiley & Sons*, 1985.

45. M. Ajgaonkar, Y. Zhang, H. Grebel, R. Brown, "Linear and nonlinear optical properties of germanium implanted coherent array of submicron silica spheres", submitted to *Optics Letters*, September 2000.

46. J. R. Heath, J. J. Shiang and A. P. Alivisatos, "Germanium quantum dots: optical properties and synthesis", *Journal of Chemical Physics*, **101**(2), 1607-1615, 1994.

47. P.C. Becker, N.A. Olsson, J.R. Simpson, "Erbium-doped fiber amplifiers: fundamentals and technology", *Academic Press*, 1999.

48. A. Polman, "Erbium implanted thin film photonic materials", *Journal of Applied Physics*, **82**(1), 1-39, 1997.

49. A. Yariv and P. Yeh, "*Optical Waves in Crystals*", Wiley and Sons, New York, 1984.

50. D. Skoog, F. James Holler and Timothy Nieman, "Principles of Instrumental Analysis", *Saunders College Publishers*, Fifth Edition, 1997.

51. J. Tobias and H. Grebel, "Self-imaging in photonic crystals in sub-wavelength range", *Optics Letters*, **24**, 1660 –1662, 1999.

52. M. Fujii, A. Minura, S. Hayashi, K, Yamamoto, C. Urakawa and H. Ohta, "Improvement in photoluminescence efficiency of SiO2 films containing Si nanocrystals by P doping: an electron spin resonance study", *Journal of Applied Physics*, **87**(4), 1855-1857, 2000.

53. Harry J.R. Dutton, "Understanding optical communications", *Prentice Hall Publications*, 1998.

54. S.J.B.Yoo, "Wavelength conversion technologies for WDM network applications", *IEEE Journal of Lightwave Technology*, **14**(6), 955-966, 1996.

55. Govind P. Agrawal, "Nonlinear fiber optics", *Academic Press*, 1989.

56. Timothy J. Whitely, "A review of recent system demonstrations incorporating 1.3 μ m Praseodymium doped fluoride fiber amplifiers ", **13**(5), 744-760, 1995.

57. S. Vijayalakshmi, Y. Zhang, H. Grebel, G. Yaglioglu, R. Dorsinville, C.W. White, "Nonlinear dispersion properties of sub-wavelength photonic cystals", *OSA & IEEE LEOS* sponsored International conference on Nonlinear Optics: Materials, Fundamentals and Applications, August 6-10, 2000, Hawaii.

58. Edited by: T. Ogawa, Y. Kanemitsu, "Optical properties of Low Dimensional Materials", *World Scientific*, 1995.

59. D. Weaire, B.S. Wherrett, D.A.B. Miller and S.D. Smith, "Effect of low power nonlinear refraction on laser beam propagation in InSb", *Optics Letters*, **4**, pp 331-333, 1974.